CMOS-COMPATIBLE SCALABLE MICROFABRICATION OF GRAPHENE POLYMERIC STRAIN GAUGE ARRAYS

by
MELİH CAN TAŞDELEN

Submitted to the Graduate School of Engineering Sciences
in partial fulfilment of
the requirements for the degree of Master of Science

Sabancı University
August 20

CMOS-COMPATIBLE SCALABLE MICROFABRICATION OF GRAPHENE POLYMERIC STRAIN GAUGE ARRAYS

Approved by:

Asst. Prof. Dr. MURAT KAYA YAPICI ……..
(Thesis Supervisor)

Prof. Dr. MELİH PAPİLA ..……..……..

Prof. Dr. ZAFER ZİYA ÖZTÜRK……..

Approval Date: August 28, 2020

ABSTRACT

CMOS-COMPATIBLE SCALABLE MICROFABRICATION OF GRAPHENE POLYMERIC STRAIN GAUGE ARRAYS

MELİH CAN TAŞDELEN

MATERIALS SCIENCE AND NANO ENGINEERING, MSc. THESIS, 2020

Thesis Supervisor: Asst. Prof. Dr. MURAT KAYA YAPICI

Keywords: Graphene, Strain Gauge, Piezoresistivity, MEMS, Microelectronic Fabrication, Semiconductor Process Technology

Over the years, microelectromechanical systems (MEMS) have been utilized widely in sensing applications due to their characteristics such as small form-factor, ultra-high sensitivity, low-cost and scalability. Among the various sensing principles, piezoresistive effect has proved to be critical for strain sensing applications, owing to several advantages including compatibility with standard microelectronic fabrication techniques, ability for either monolithic or heterogeneous integration with readout circuitry which have rendered widespread use of piezoresistive sensors in various fields like structural and environmental monitoring. However, the sensitivity of strain gauges otherwise referred to as the gauge factor (GF) is limited to single digits (~ 2) for commercial metal-foil gauges on polymeric substrates. Single crystal silicon or polysilicon strain gauges achieve much higher GF values but at the expense of smaller ultimate strains and need for moderate to high levels of doping translating into additional process steps and higher device costs. On the other hand, graphene, a two-dimensional (2D) honeycomb structure of sp^2 hybridized carbon atoms has vast potential for strain sensing applications due to its distinctive mechanical and electrical properties, provided that it can be integrated into standard semiconductor process flows. This thesis reports on the microfabrication of graphene strain gauges in arrayed format on flexible, polymeric structural layers where SU-8 was selected due its stable chemical and mechanical properties. Experimental characterization results show that, the fabricated graphene strain gauges achieve more than two orders of magnitude increase in GF values of up to 300, along with Raman results verifying successful integration of graphene layers into device format based on well-defined, scalable and IC-compatible processes.

ÖZET

GRAFEN POLİMERİK GERİNİM ÖLÇER DİZİNİNİN CMOS UYUMLU ÖLÇEKLENEBİLİR MİKROFABRİKASYONU

MELİH CAN TAŞDELEN

MALZEME BİLİMİ VE NANO MÜHENDİSLİK, YÜKSEK LİSANS TEZİ, 2020

Tez Danışmanı: Dr. MURAT KAYA YAPICI

Anahtar Kelimeler: Grafen, Gerinim Ölçer, Piezorezistif, MEMS, Mikroelektronik Fabrikasyon, Yarıiletken Proses Teknolojisi

Mikroelektromekanik sistemler (MEMS), küçük biçim faktörü, aşırı yüksek hassasiyet, düşük maliyet ve ölçeklenebilirlik gibi özelliklerinden dolayı yıllar içinde algılama uygulamalarında yaygın olarak kullanılmaktadır. Çeşitli algılama ilkeleri arasında, piezorezistif etkinin, standart mikro elektronik fabrikasyon teknikleriyle uyumluluk, yapısal ve çevresel izleme gibi çeşitli alanlarda piezorezistif sensörlerin yaygın kullanımına hizmet etmesini sağlayan tek yongalı veya heterojen entegrasyon yeteneği okuma devresi ile gerilim algılama uygulamalarında kritik olduğu kanıtlanmıştır. Bununla birlikte, ölçü faktörü (GF) olarak adlandırılan gerinim ölçerlerin hassasiyeti, polimerik altlıklar üzerindeki ticari metal-varak göstergeleri için tek rakamlarla (~2) sınırlıdır. Tek kristal yapılı silikon veya polisilikon gerinim ölçerler çok daha yüksek GF değerlerine ulaşır, ancak daha küçük gerilmeler ve ek işlem adımları pahasına daha yüksek cihaz maliyetlerine yol açan orta ila yüksek seviyelerde doping gereksinimi mevcuttur. Öte yandan, sp2 hibritlenmiş karbon atomlarının iki boyutlu (2D) bal peteği yapısı olan grafen, standart yarı iletken süreç akışlarına entegre edilebilmesi koşuluyla, kendine özgü mekanik ve elektriksel özelliklerinden dolayı gerilim algılama uygulamaları için büyük bir potansiyele sahiptir. Bu tez, durağan kimyasal ve mekanik özellikleri nedeniyle SU-8'in seçildiği esnek, polimerik yapısal katmanlar üzerinde sıralanmış formatta grafen gerinim ölçerlerin mikrofabrikasyonunu rapor eder. Deneysel karakterizasyon sonuçları gösteriyor ki, üretilen grafen gerinim göstergeleri, grafen katmanlarının iyi tanımlanmış, ölçeklenebilir ve entegre devreye dayalı cihaz formatına başarılı bir şekilde entegrasyonunu doğrulayan Raman sonuçlarıyla birlikte, GF değerlerinde 300’e kadar, iki kat büyüklüğünde artış elde edilmiştir.

ACKNOWLEDGEMENTS

This page of the thesis will be reserved for people in my life who have left traces that have always sparkled at the end of the blurry tunnel to guide me, to encourage me, and sometimes to remind me who I am. First of all, I would like to extend my deeply gratitude to Asst. Prof. Dr. Murat Kaya Yapıcı who has shared his knowledge and experiences with his complete professionalism, extraordinary patience, and priceless guidance throughout the study. Under his supervision, I found myself as being a part of the academy thus making me feel adequate to be a candidate researcher in this realm.

Next, I need to say something about my excellent and adorable friends who were not just friends, but were also creators of warm, cheerful, and helpful atmosphere making life easier for people like us who spend their times in a very competitive environment. I would like to thank cordially Farid Sayar Irani, Osman Şahin, and Tuğçe Delipınar, who have always provided precious support for me, and they have always been keen on taking the load off my shoulders especially in the last days of the work. Furthermore, I would like to share my thankfulness with Asena Gülenay Tatar, Gizem Demir, and Efsun Şentürk, who spent their efforts to fill my stomach with very delicious meal sometimes better than my mother's, which made my brain much more functional than ever before.

Thesis writing is a challenging task which I found a chance to experience that together with Özberk Öztürk, who has shared the same feelings along the study period. Even though it was a hard time for both of us, it became easier to keep my mental endurance with his companionship. B9, dormitory lounge as our temporary shelter, has witnessed the times that we spent together.

Finally, I send my great appreciation to my dearest parents, who offered their eternal support and encouragment, and made me feel stronger with their existence.

TABLE OF CONTENTS

LIST OF TABLES

LIST OF FIGURES

LIST OF ABBREVIATIONS

1. INTRODUCTION

With the popularity of the internet-of-things (IoT), smart, ubiquitous, pervasive sensing is rapidly gaining importance to provide reliable information at unprecedented sensitivity to enable new applications in electronics such as consumer electronics [1], healthcare [2], manufacturing and structural health monitoring [3-5], transportation [6], defense and surveillance [7], robotics and space-based systems, and therapeutics [8]. Microscale strain sensors in MEMS have attracted intense interest due to their functionalities such that they are capable of measuring force, acceleration, pressure and sound, which allow obtaining and processing simple data over an integrated readout electrical circuit solution.

Recent studies have shown that piezoresistive sensing has been great importance of strain sensors among the various sensing approaches as the sensorial part of the strain sensor is originated from the piezoresistive sensing modality. Practicability of the fabrication process and ease of integration for the read-out circuitry have broadened the use of piezoresistive sensors in several fields such as structural and environmental monitoring applications. Strain sensing, usually, operates under tensile strain as the body expands and under compressive strain as the body contracts, and they are designed to attach to the surface of the target object in order for a purpose of sensing deformations as a result of stress which induce the electrical resistance change of the sensor element. These principals make the strain sensors resistive measurement-based devices [9].

Traditional piezoresistive sensors are made up of semiconductors or metal oxides. Since semiconductor based piezoresistive sensors show a wide range of gauge factors larger than 100, silicon as a prominent semiconductor, is utilized typically as a piezoresistive material in sensor applications owing to its great mechanical behaviors and a high piezoresistive coefficient with a large gauge factor in comparison to its alternatives. As

an example, the value for p-type [110] single crystalline silicon gauge factor has been reported around 200 [10-12], which makes it more precise in measurements as semiconductor gauges (piezoresistors) and more preferable to metal foils. Since thin metallic layers have a higher impact on the overall stiffness of the structure, it is a good idea to substitute metals with fillers like carbon nanotubes, conductive carbon fibers, and graphene for the sake of increasing the tolerance of the sensors for the case in which high flexibility is required [8].

The fact that semiconductors are fragile materials, the strain range detection is attenuated, thereby limiting the applications. Besides, the piezoresistive sensors comprised of metal or metal oxides demonstrate small sensitivity impeded by the dimensional change in conduction path. Therefore, both semiconductor and metal/metal oxide based piezoresistive sensors prove that they don't show their potentials in flexible and stretchable applications [13].

In the last decades, strain sensors have become more and more popular among researchers, materials that can display an appreciable response upon even small strains have been investigated in order to fabricate effective strain sensors. In recent studies, nanoscale materials including noble metal nanomaterials (e.g. nanoparticles, nanowires) and carbon materials (e.g. carbon nanotube and graphene) have been considered as functional materials in strain sensor applications where piezoresistive effect is utilized. Nonetheless, utilization of the noble metal nanomaterials in the flexible piezoresistive sensors require complicated and expensive manufacturing processes such as advanced nanostructure design, which are actually not applicable and scalable [13]. On the other hand, carbon-based strain sensor presents an alternative for flexible piezoresistive sensor applications, which agrees with low-cost production and material compatibility requirements. As a prominent two-dimensional material, graphene has robust strength, large surface area, excellent flexibility and high conductivity, which make it a superior alternative to use in piezoresistive sensors [14].

With the advent of wearable devices, there is a demand for flexible piezoresistive sensors to use in next generation of portable devices. In recent studies about micromechanical and microfluidic systems, polymeric materials have gained great interest since they are produced faster and in lower cost in comparison with Si-based materials [15]. Structural

layer(s) of mechanical micro-devices can also be comprised of polymers. The main technique is utilized to shape these polymeric layers is lithography, which the polymeric resist is exposed by an energetic radiation, such as UV light in optical lithography or by a electron beam in EBL (electron beam lithography). Then, the resist will be stripped away by chemical dissolution due to fundamental changes in structure of the exposed or non-exposed area based on the resist type, which is positive (scission of the chain) or negative (cross-linking) [16]. SU-8 is an epoxy-based negative resist commonly used in MEMS owing to its high aspect ratio, good mechanical properties and etching resistance [16]. SU-8 has become a popular, cheap, and easy fabrication alternative to silicon for micro components such as such as microchannels, electroplating micromolds and hot embossing masters. It was also shown that passive SU-8 can be used in atomic force microscopy [17]. SU-8 is chemically resistance material thereby becoming a component material. It is able to form different layer thicknesses from 1 micron to 1 mm with high aspect ratio [18]. Since SU-8 is much softer and conformable to a gold resistor, it is proven that SU-8 has shown almost the same sensitivity change as the silicon piezoresistive sensors [19].

Main motivation of this thesis is to present an extensive study to show the fabrication procedures and the performance characteristics of the graphene-based SU-8 polymeric piezoresistive strain sensors. In this thesis, the concept of piezoresistive SU-8 polymeric sensors has been broadly explained, and optimizing design, fabrication, and performance of these sensors have been studied. First, inclusive information on the graphene and its strain sensing applications will be presented. Then, SU-8 polymer-based piezoresistive cantilever sensors are critically reviewed within the aspects of the design, fabrication, and performance. Next, SU-8 polymeric piezoresistive strain sensors fabricated using common microfabrication techniques will be delivered as background information. Also, the optimization of the fabrication processes of the SU-8 polymeric piezoresistive strain sensors will be presented in order to provide a systematic study to demonstrate the effects of several parameters such as baking temperature, exposure dose, development and etching time, and developer and etching solution. Lastly, the obtained data from the piezoresistive SU-8 polymeric strain sensors performed bending tests will be demonstrated.

1.1. Graphene

Graphene is a two-dimensional material formed by arrangement of single layer carbon atoms as hexagonal rings. The formation of carbon atoms is a honeycomb-like shape that each atom is placed in each vertex. This allows graphene to be the most dynamic material known. Therefore, graphene has become more preferable and promising in numerous applied research fields like batteries and supercapacitors due to its thin, flexible qualities, large surface area and rapid charging duration. Moreover, graphene's outstanding electrical, thermal and mechanical properties make it a superior alternative to use in strain sensors, Nano-electronics, flexible and photonic circuits, biomedical industry and catalysis application [14]. The compatible formation of graphene with the semiconductor fabrication technology is widening the areas of its utilization as well.

Among the various sensing modalities, piezoresistive sensing has been widely used in structural [20] and environmental [21] monitoring applications where the fundamental detection principle relies on the variation in resistance of the sensor element as a result of the physical measurand exerted on the sensor which is typically comprised of a micromechanical element that is engineered to be susceptible to deformation due to stress.

Various materials are utilized in the sensor, which can be customized according to types of measured quantity. Different qualities and parameters, such as selectivity, sensitivity, accuracy, stability, and etc., are considered to select a proper and efficient sensitive material for the sensor applications [22]. Instead of conventional materials, such as metals, metal oxides, semiconductors which possess mechanical, electrical and thermal qualities, graphene has gained attention thanks to its promising physical, mechanical, and electrical [23-25]. Lately, it has been widely studied as a functional material in sensor appplications, which gains higher efficiency to sensors for different applications.

1.1.1. Fundamental Properties

With the discovery of graphene as the first 2D material, studying with single-atomic thickness materials became easier. Unique fundamental properties, (electrical [26, 27],

mechanical [28], optical [29], and sensing [30, 31] properties) of graphene show differences with respect to bulk graphite.

1.1.1.1. Electrical

With the first experimental isolation of graphene on insulator, there has been a rapid growing interest in physics, which included observations of graphene's ambipolar field effect, the quantum Hall effect at room temperature, measurements of extremely high carrier mobility, and even the first detection of single molecule adsorption events. These properties made graphene a highly attractive material in a number of devices such as future generations of high-speed and radio frequency logic devices, thermally and electrically conductive reinforced composites, transparent electrodes for displays and solar cells, and sensors [32].

The electronic properties of both graphene and carbon nanotube from a theoretical point of view were discussed [33], which graphene should be regarded as a metal rather than a zero-gap semiconductor. In another research, j. Nilsson et al. [34] presents results for the electronic properties of disordered graphene multilayers which show that it is a new class of materials with an unusual metallic state.

Typically, exfoliated graphene shows better quality, in terms of different properties, than CVD graphene and rGO. These differences are due to the disorder and the scattering process which do not exist in exfoliated samples. Source of disorder in CVD-grown graphene indicates lattice defects and grain boundaries created through growth process, and structural defects and chemical contamination created during transfer [35-40]. Results show that CVD-grown graphene exhibits lower electronic properties when compared to exfoliated samples, whereas recent works show progress in electronic properties of CVD-grown graphene [38-44]. It was demonstrated by multiple measurements that CVD-grown graphene can achieve repeatable electronic performance like exfoliated samples [45].

1.1.1.2. Mechanical

Graphene is known for very high in-plane stiffness (Young's modulus) and the highest ever measured mechanical strength [28, 46, 47]. Unique mechanical properties of graphene are very important due to its significant role in its applications. For example, durability of graphene is used in electronic and energy storage, its elasticity or plastic deformation and fracture could be applied in electronic and structural application, and nanocomposites with graphene additions are utilized as structural and/or functional materials [48]. An atomic force microscope (AFM) was used on single layer graphene membranes to measure its elastic properties and strength [28]. The breaking strength and elastic stiffness were reported as 42 Nm-1 and 340 Nm-1, respectively. These results confirm graphene as the strongest material ever, making it suitable to work in mechanical tests and flexible applications.

In a study, mechanical properties enhancement of nanocomposite based on exfoliated graphene nanosheets and poly(vinyl alcohol) via a facial aqueous solution was shown [49]. A considerable improvement on the mechanical properties of graphene/PVA composite was observed. In a composite with a loading of 1.8 vol % graphene sheet, tensile strength and modulus values are greater than PVA sample, by 2.5 times and more than 10 times, respectively.

A nondestructive mechanical analysis with AFM was performed on a suspended exfoliated graphene layer on a trench pattern in silicon oxide/silicon substrate [50]. The graphene thickness was less than 10 nm and the spring constants varied between 1 to 5 N/m. A young's modulus of 0.5 TPa was obtained which is much less than the value for bulk graphite equal to 1 TPa.

1.1.1.3. Piezoresistivity

Piezoresistive effect is observed when a change in electrical resistivity of a material occurs as a result of the applied stress which shows itself as a deformation. Germanium [51], silicon [52] and polycrystalline silicon [53] are the most common semiconductor materials that show piezoresistive effect and they are used frequently in MEMS for sensing strain, pressure, acceleration, flow as well as tactile sensing and haptics

applications. Graphene attracted a lot of attention not only due to being the thinnest known material and having its special mechanical and electrical properties, but also due to observing linear change in resistance versus strain, making it a good candidate for piezoresistive sensor applications [54]. Graphene shows 1 TPa of the mechanical stiffness and 130 GPa of the intrinsic breaking strength at 25% strain, which is comparable to considerable in-plane values of graphite and other materials with high mechanical strengths [28]. When electronic properties such as having high velocity electrons (1/100 velocity of light) and a zero-band gap are combined with these mechanical properties, graphene-based strain sensors are achievable. In this regard, the piezoresistivity of a uniform coated multilayer of graphene on a poly (methyl methacrylate) (PMMA) substrate was investigated [55]. The characterization was achieved by a bending test that has shown a high piezoresistivity with a gauge factor of 50, which made it practical as a reliable strain sensor. In addition, Anderson D. Smith et al. have verified the piezoresistive effect in graphene by applying uniaxial and biaxial strains [56]. It has been proven that experimental results are different from what simulation predicted. Also, it has been figured out gauge factor of biaxial strained devices is higher than uniaxial one.

The piezoresistivity effect of graphene has been elucidated with three different mechanisms in the followings as shown in Fig.1:

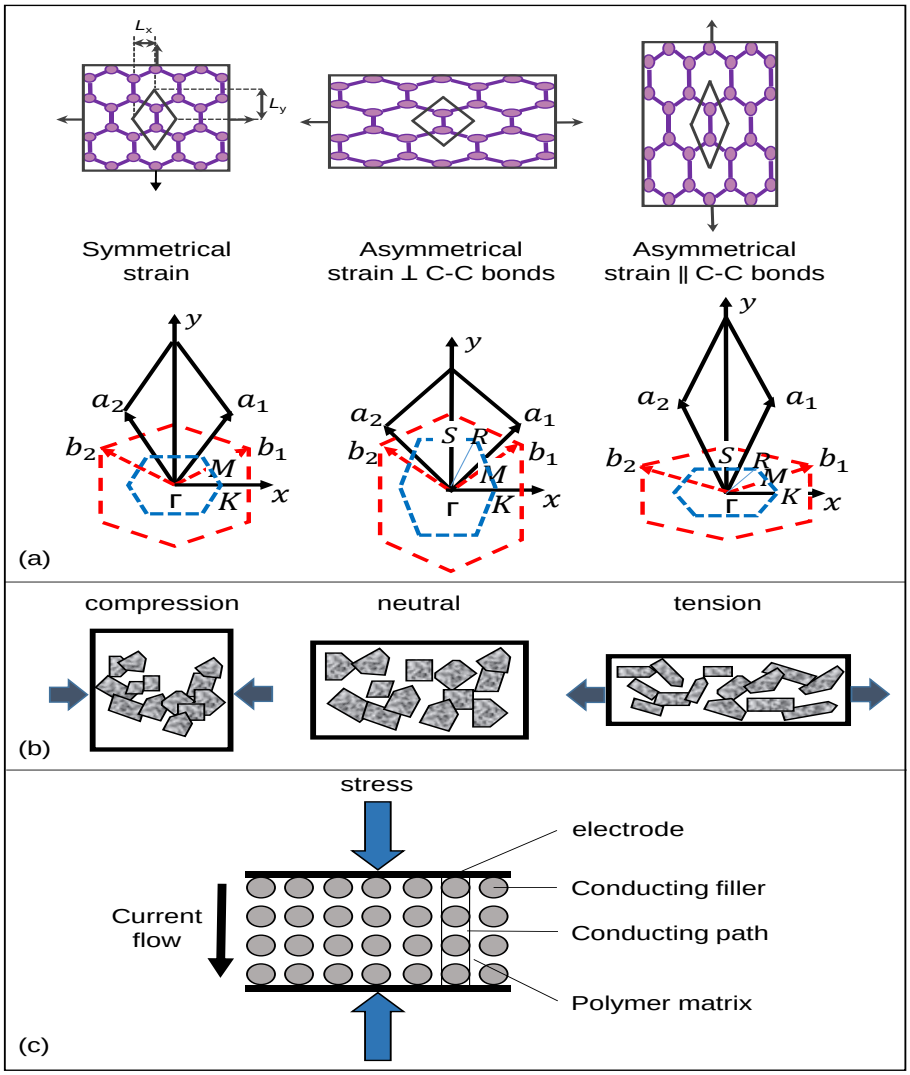

Figure 1. (a) Symmetrical strain distribution, asymmetrical strain distribution perpendicular to C-C bonds, and asymmetrical strain distribution parallel to C-C bonds [57]. (b) Schematic illustration of piezoresistivity of graphene sheets [58]. (c) Schematic illustration of the tunnelling model [59].

1.1.1.3.1. Structure Deformation

Graphene, as a two-dimensional uniform semiconductor material, bears up to one fourth of tensile elastic strain, which makes it the strongest material that ever known. Electrical-mechanical coupling in graphene could be observed when a significant elongation in graphene causes change in its electrical properties and electrical band structure. Recent

studies on strained graphene demonstrated that changes in graphene electrical properties is related to type of strain distribution, which an asymmetrical strain distribution in graphene causes shift in Dirac cones and reduction in fermi velocity due to pseudo-magnetic field. In a symmetrical strain distribution, an additional scattering and resistance decrease was observed while no change happens in graphene properties [60-65]. Upon many distinct properties and demand for device applications, graphene became a valuable source for engineering Fermi velocity which is one of the important concepts in the material research [66].

The band gap is enlarged by increasing the amount of strain. It can reach a maximum value of 0.486 eV in a graphene that the strain is parallel to C-C bonding and increased to 12.2%. Also, in a graphene with a perpendicular strain to C-C bonding, band gap increases to maximum 0.170 eV by increasing strain to 7.3% (Figure 1a) [57].

1.1.1.3.2. Over Connected Graphene Sheets

Besides the structure deformation that primarily describes the resistance change in graphene, there are more theories to explain it. One is connected graphene sheets in a large scale which the sheets are not a full-grown graphene and form a conductive network. The distortion of a single graphene sheet from a nanoscopic perspective alters the resistivity of the single sheet that can trigger a resistance change in the entire conducting system. Thus, response of the graphene to the applied stress network relies primarily on the contract strength of the neighbouring plates from a macroscope point of view. Overlap area and contact resistance determines the conductivity between the neighbouring flakes. As demonstrated in Fig. 1b, the overlap between neighbouring flakes becomes smaller or greater that the resistance changes accordingly once a compression or tension is applied to the graphene film. This mechanism makes graphene applicable in strain sensors [14, 58].

1.1.1.3.3. Tunneling Effect Between Neighbouring Graphene Sheets

It is known that the separation between two graphene sheets specified the conductivity of

graphene. Accordingly, the gauge factor is limited to less than 200. Due to the tunnelling effect current flows between single graphene plates, and their separation distance and resistance change relates exponentially (Figure 1c) [59]. This mechanism could be used for higher GF in graphene-based strain sensors.

1.1.2. Synthesis

Graphene as a 2-D material provides unique properties inherently involving ultra-high mobility [67], astonishing mechanical strength [28] while it has the ability to be stretched over 20% [68]. Despite its superior electrical and mechanical properties, the challenges of obtaining pristine graphene, limits the widespread use of this 2D material in device applications. In an effort to address this problem, numerous techniques were investigated to obtain thin graphitic films and few layers graphene after its initial demonstration by Geim and Novoselov with mechanical exfoliation method (i.e. Scotch tape), which was a major breakthrough in graphene research that was announced the effort of transferring graphene onto a silicon substrate coated with a layer of silicon dioxide (SiO_2) typically 300 nm-thick [69] and measuring its electrical properties. Even though Scotch tape method provides the highest quality graphene, however wafer size scale graphene is needed for mass production.

Synthesizing a high-quality graphene is one of the critical matters in which serious efforts have been conducted over the last decades. Different methods, which were classified as bottom-up and top-down processes, have been utilized in order to synthesize a high-quality graphene. The most commonly used methods are: Chemical Vapor Deposition (CVD) [70], exfoliation [71, 72], reduction of graphene oxide [71, 73], epitaxial growth [74]. Unzipping nanotubes, and microwave synthesis of graphene are two techniques as well [67]. The advantages and drawbacks of these methods are highlighted in Table 1.

Table 1: Brief history of buttom-up and top-down graphene [67]

Ref	Method	Thickness	Lateral	Advantage	Disadvantage
[70, 75-79]	CVD	Few layer	Very large in cm	Large size, high quality	Small production scale
[80-86]	Epitaxial growth on SiC	Few layers	Up to cm size	Very large area of pure graphene	Very small scale
[87-89]	Unzipping of carbon nanotubes	Multiple layers	Few micron long nano ribbons	Size controlled by selection of the starting nanotubes	Expensive starting material; oxidized graphene
[90]	Reduction of CO	Multiple layers	Sub-micron	Un-oxidized sheets	Contamination with α-Al_2O_3 and α-Al_2S
[72]	Micromechanical exfoliation	Few layers	Micron to cm	Large size and unmodified graphene sheets	Very small scale production

Micro-mechanically cleaved graphene is commonly preferred for the fundamental research due to the significance of the quality of graphene, so this method promises one that is closest to the nature of graphene. In the chemical exfoliation method, large alkali ions are used to exfoliate graphite in solution dispersion. A similar process exists in chemical synthesis methods, in which solution dispersed graphite oxide is reduced with hydrazine. Catalytic thermal CVD, which is the most important process in terms of large-scale graphene fabrication, is utilized to synthesize carbon nanotube by surface precipitation or dissociation [67].

Epitaxial growth on silicon carbide (SiC), is another method to gain a wide range of graphene which works with thermal decomposition of bulk SiC [74, 91, 92]. Because the SiC is itself a practical semiconductor, only by controlling the growth condition, the obtained epitaxial graphene could hold all the transport properties of a monolayer graphene. Also Sic is commercially available that makes this method very desirable for device applications [93-98]. Recently, different substrates, such as Ru(0001) [99], Ir(111) [100], Cu(111) [70, 101], Pt(111) [102] and Ni thin film [103] were reported as the substrates to obtain high quality EG (epitaxial graphene). In order to produce a large

single-crystal graphene film in a short time, the domains should be aligned and perfectly stitched, that was observed when Ge(100) and Cu(111) were used as the substrate [104, 105]. Besides, a number of popular methods such as Plasma Enhanced Chemical Vapor Deposition (PECVD) [106] and spray-deposited graphene from solution [107], have been demonstrated in which graphene could be directly deposited on a substrate without catalytic. On the other hand, the synthesis methods have some disadvantages that depend on the type of device and the area in which the graphene is being used. To illustrate, in the mechanical exfoliation method, graphene might be fabricated in the order of monolayer to few-layers, which comes up with the reliability issue such that when a similar structure is obtained by using this method, it might show some structural changes. Moreover, chemical synthesis processes are conducted in low temperatures, which are more suitable for graphene synthesis on different substrates at room temperature, especially on polymeric substrates; however, large scale synthesize of graphene obtained in this process are dispersed and non-uniform. Besides, reduced graphene oxide technique is not reliable in terms of the rate of reduction, therefore succession of the reduction depends upon the rate of reduction. On the contrary, thermal CVD methods are more beneficial for large-area device fabrication and promising for future complementary metal oxide semiconductors (CMOS) technology by replacing Si [108]. Epitaxial graphene method includes high thermal treatment for graphitization of a SiC surface, which restricts transfer of graphene on any other substrates. On the other hand, a uniform layer of thermally chemically catalysed carbon atoms is obtained by the thermal CVD method that the deposition is done on a metal surface and transferring to various substrates is possible [67]. Figure 2 presents an outline of graphene synthesis techniques as a flow chart.

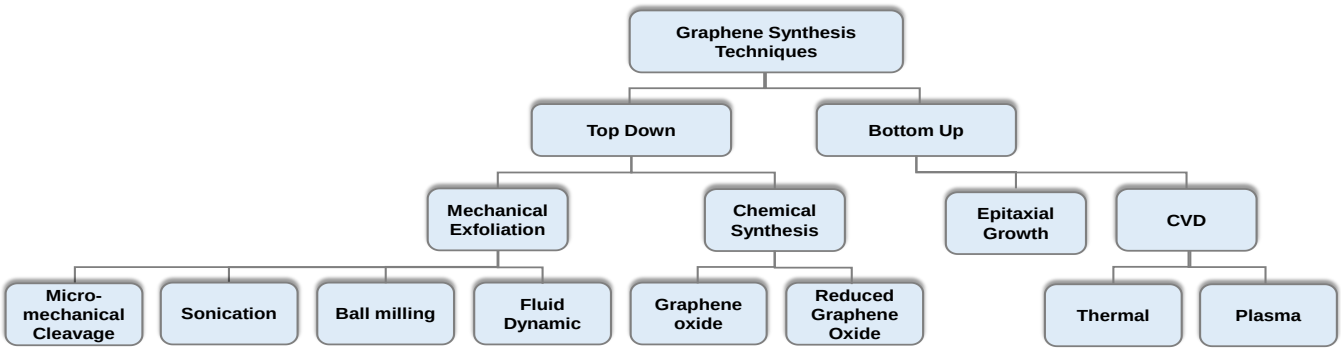

Figure 2. Summary of the different techniques to obtain graphene categorized based on

top-down and bottom-up fabrication techniques [67].

1.1.2.1. Chemical Vapor Deposition

CVD synthesis of few-layer graphene (FLG) was reported firstly in 2006, from that day forward the CVD bottom-up synthesis has progressed to a method providing scalable and reliable production technique of a high quality and large-area graphene [109-112]. However, the quality of exfoliated graphene continues to show better properties as compared to the properties of CVD-produced graphene. The growth and development of high-quality, large area graphene by using CVD method on catalytic metal substrates is a recent topic for both fundamental and technological interest. CVD technique provides many opportunities such as inexpensive, transferable, ability to produce high quality and large-area graphene films, which make it the most promising methodology [23]. Due to the existence of polycrystalline structure of the synthesized large-scale graphene, the studies are focused on monitoring domain sizes, number of graphene layers, density of grain boundaries, defects etc. It is required to solve these problems in order to realize the potential of graphene for utilizing it into the graphene-based applications.

The deposition in CVD technique happens by forming a stable solid over a suitable substrate because of chemical reaction between gaseous reactants (Figure 3a). The chemical reactions require energy that is supplied by various sources of which are heat, light, or electric charge used in thermal, laser-assisted, or plasma-assisted (PA) CVD respectively. There are two different reactions occurring in the deposition process; first is homogeneous gas-phase reactions, and second is heterogeneous chemical reactions arising on a heated surface. Powders and/or films are formed in each case [113]. In CVD method, a catalytic transition metal such as copper (Cu) [70], nickel (Ni) [114] is used as a substrate to grow mono- or multiple layers of graphene. Copper is a suitable material for graphene synthesis, as it promises low costs such as flexible Cu foils which are affordable in price. Besides, carbon solubility is particularly low (0.03 atom %) at the standard graphene growth temperatures (1000-1060°C) [115]. Removing oxide from the surface of copper is done by annealing the Cu substrate at 1000°C in a chamber filled by hydrogen and argon. Detachment of methane gas (CH_4) to carbon atoms is occurring on the surface of Cu substrate in order to form the graphene lattice. Formed Graphene islands

on the substrate owing different lattice orientations that enlarge and grow together [116]. As the graphene islands merge a grain boundary is formed, which might affect the electronic properties (e.g., scattering effect induced electron mobility at the level of grain boundaries) [96, 97] or the mechanical characteristics (e.g., higher possibility of crack formation) [117, 118].

A common transfer method that has been developed recently, especially for CVD synthesized-graphene, is polymer-supported metal etching. Moreover, there are a few exceptions in which a polymer is employed as a support layer for HOPG [117] or graphene oxide (GO) [119] film transfer [120]. During such a transfer process, the key idea is that the metal layer where graphene is grown up is a sacrificial layer, therefore the metal layer is required to be removed after the synthesis is complete. $Fe(NO_3)_3$, $FeCl_3$, $(NH_4)_2S_2O_8$ are chemical solutions used to etch Ni and Cu metal layers away from the surface, without needing a polymer support. A report from Hong group has shown that transferring a CVD graphene layer to SiO_2/Si substrate was reported in which wet etching of SiO_2 and Ni layers was performed by BOE and $FeCl_3$ solutions respectively (Figure 3b) [121]. Nevertheless, the ultrathin graphene shows a tendency to be ripped and torn during the etching and transfer process, and also it depends on the quality of synthesized graphene because a slight disturbance could even be enough to break apart graphene. Thereby, the use of polymer support guarantees the safety of graphene transfer that makes polymer support transfer a preferable method in many research compared to other techniques such as dry transfer [110]. Besides, polymer-supported transfer method enables to transfer large area graphene as synthesizable CVD graphene resulting in rapid increasing of the area to several inches in lateral width.

Another preferable material for graphene transfer to a substrate is PDMS (polydimethylsiloxane). Promising properties of PDMS such as durability, unreactivity, moldability, solvent resistance, and most significantly its low surface free energy makes the material excellent for soft lithography [120, 122, 123]. Therefore, the low adhesion force is maintained between PDMS and the applied substance on the PDMS, and it helps the substance released from PDMS when it is in contact with the target substrate and stamped onto the substrate. The same mechanism is applied for the graphene. In addition, PDMS support graphene from mechanical defects during the transfer process until the metal substrate etching is completed (Figure 3c) [121]. SiO_2/Si and PET are known as

typical substrates for transferring graphene from PDMS that the soft lithography principle is utilized. Figure 3 demonstrates the schematic process of the PDMS transfer.

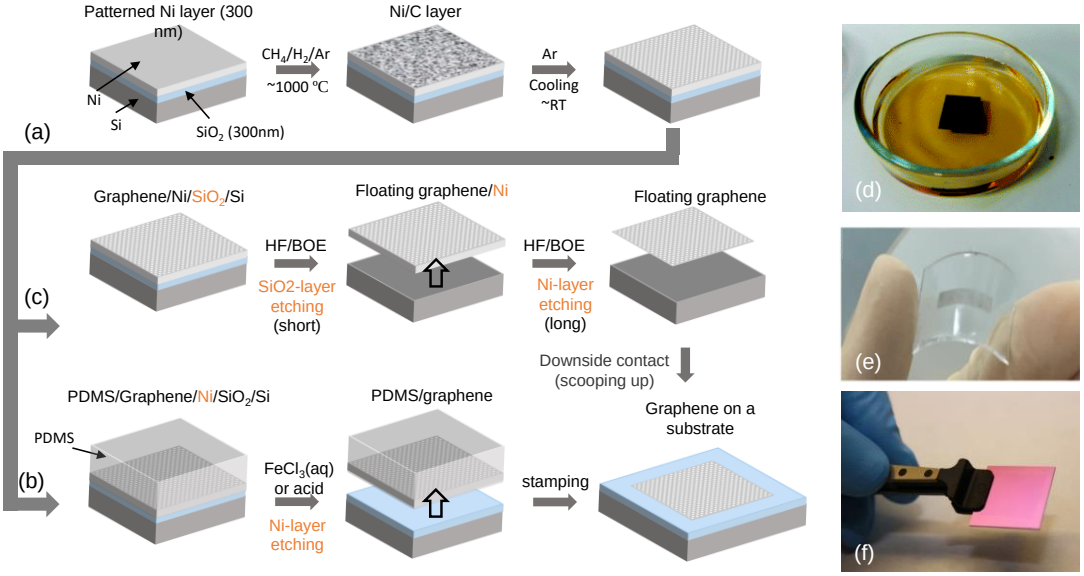

Figure 3. Make use of polymeric soft substrate (PDMS) for dry transfer of graphene layer grown on Ni film. (a-c) Schematic pictures of transferring processes of patterned graphene films with and without PDMS stamp [121]. (d) Using $FeCl_3$ solution to etch underlying Ni layer [124]. (e) Transparent graphene films on the PDMS substrate [125]. (f) The graphene film on SiO_2 substrate [126].

PDMS is also useful for fabricating a graphene-based device by stamping method [120]. Growing a patterned graphene by using a pre-patterned metal should be done bery carefully, otherwise ruptures might occur on the surface of graphene which changes electrical and mechanical properties of graphene-based devices substantially. On the other hand, PDMS stamping technique eliminates this performance degrading, and enables nanofabrication. Kang et al. reported the successful device fabrication using PDMS stamp shown schematically in figure 4a. The molded PDMS with the desired pattern have been preffered to growing pattered graphene [127]. The patterned PDMS was stamped onto the metal/graphene surface. By etching metal layer, only graphene layer left on the patterned PDMS, which is feasible to stamp it onto devices substrate such as electrode for and organic field-effect transistor (Figures 4b, c).

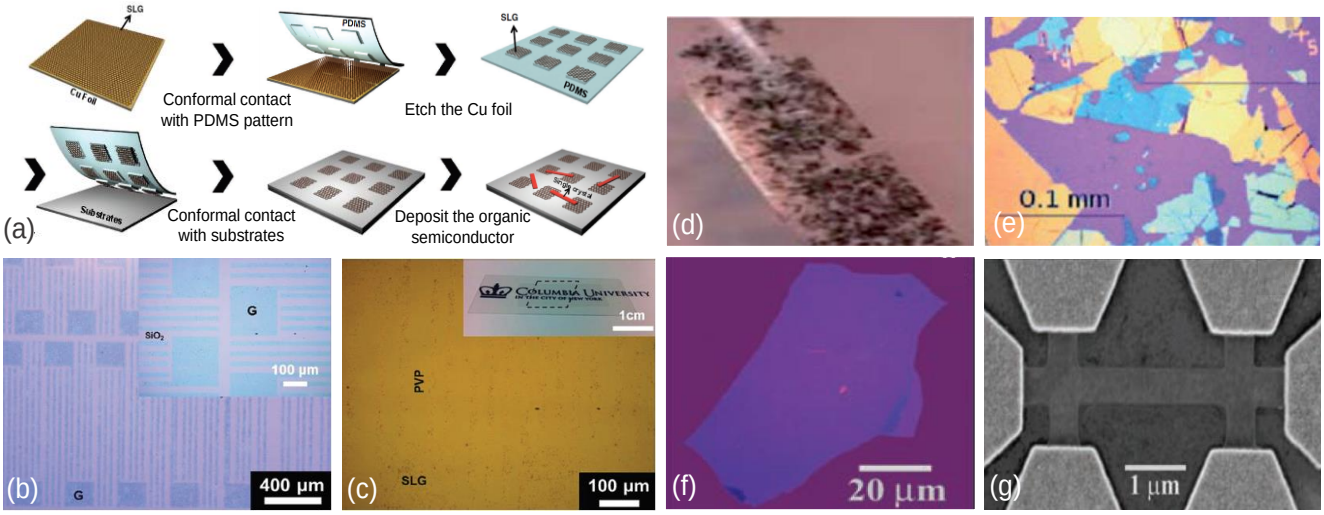

Figure 4. Mechanical exfoliation-obtained graphene flake from HOPG with using Scotch tape method. (a) A schematic of micropatterned single layer graphene transferring process to a substrate. (b) An optical microscope image of patterned SLG electrode on SiO_2. (c) Patterned SLG electrode on PET/graphene/PVP image under optical microscope [127]. (d) Graphene flakes on scotch tape. (e) Graphene flakes on SiO_2/Si wafer image under optical microscopy [120]. (f) Large few layers of graphene flakes on SiO_2/Si wafer under optical microscope. (g) SEM image of patterned graphene flake based devices [72].

1.1.2.2. Mechanical Exfoliation

The first graphene was obtained by tape-peeling method from a highly ordered pyrolytic graphite (HOPG) in 2004 by Novoselov and Geim (Figures 4d, e, f, g) [72]. Although the primary mechanical exfoliation method was not feasible for large-scale production, the obtained graphene by this method was high quality and with the high mobility of ~10000 cm^2/Vs at room temperature.

Mechanical exfoliation is one of the most promising methods to acquire high quality large-scale graphene with low cost [55]. One of the advantages about this method is that using chemical etchants such as iron nitrate [128], iron chloride [121], and ammonium persulfate [110], which are severe and ecologically dangerous, and also costly to dispose of, could be avoided. A mechanical exfoliation method has been reported for the fabricating Graphene-based saturable absorber (GSA) that the performance demonstrated

an improvement in comparison to optical deposition technique [129]. In order to optimize mechanical exfoliation method, to obtain high-quality graphene, different studies have been done to understand the exfoliation mechanism [130]. Mainly, there are two means of mechanical method to render graphite into graphene flakes by exfoliation. The first one uses normal and shear force to overcome the van der Waals attraction (Figure 5a). The other way is the fragmentation of large graphite layers to smaller ones (Figure 5b). It is easier to exfoliate smaller graphite flakes than the larger ones. However, it is not desirable for achieving large-area graphene.

In a recent study [131], different types of mechanical exfoliation techniques, such as ball milling, micromechanical cleavage, fluid dynamics, and sonication were discussed. The mechanism behind these techniques is applying a shear force or nominal force to break the Van der Waals bonds between the graphene layers in the bulk graphite. Each method is briefly discussed in the following.

1.1.2.2.1. Micromechanical Clevage

The first graphene flake was obtained from a simple idea of the exfoliation of graphene layers from the bulk HOPG surface which is a very labor-intensive and time-consuming method that is not practical for scaling up and limited mostly to academic research settings (Figure 5c) [72].

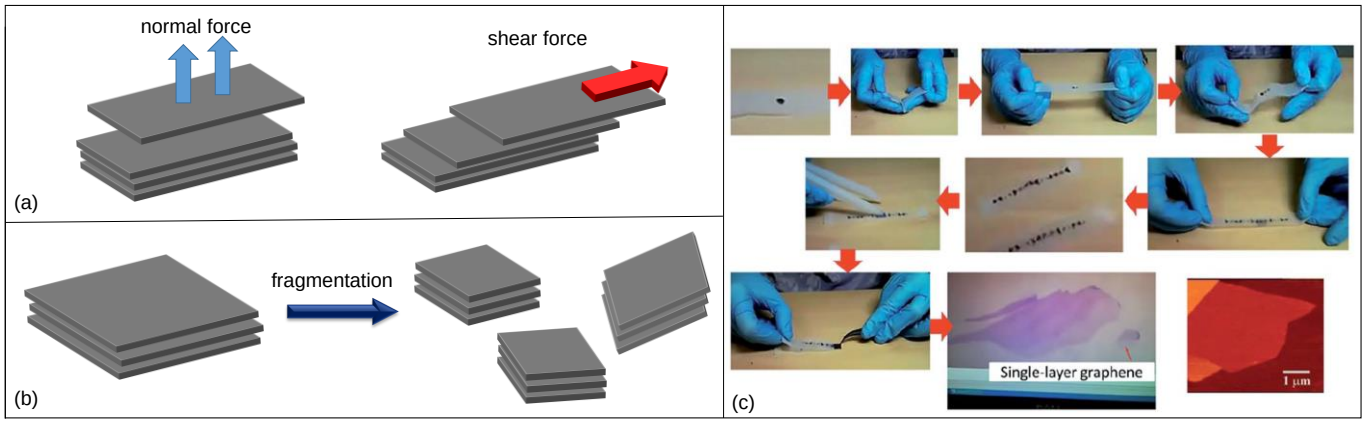

Figure 5. (a, b) Two ways to mechanically exfoliate graphite into graphene flakes. (c) An illustrative procedure of the micro-mechanical cleavage of highly ordered pyrolytic graphite (HOPG) based on repetitive pealing of a piece of graphite on adhesive tape (i.e. Scotch tape, which at the same time lends its name to the exfoliation technique) [131].

1.1.2.2.2. Sonication

Sonication method is a liquid cavitation technique that the first high-yield graphene production by using this method was reported in 2008 by Colman's group [71]. Two possible sonication processes result exfoliation are shown in Fig. 6a. The first mechanism explains tensile stress that exfoliates the flakes. The tensile stress is a consequence of compressive stress waves that are spread to the free interface of the graphite body as a result of bubbles collapse. A secondary process shows unbalanced lateral compressive stress results in separation of two nearby flakes by a shear effect. Different publications have focused on drawbacks of sonication methods that give rise to defects in acquired graphene [132-138].

1.1.2.2.3. Ball Milling

One of the popular techniques in powder production industries is ball milling that is easy to generate shear force with this technique. Fig. 6b illustrates two mechanical mechanisms that are presented so far. In the primary way, applied shear force is the

main reason for exfoliation that results in large-sized graphene flakes. The second mechanism is a fragment of large flakes to small ones caused by collisions or vertical attractions of the balls during rolling actions. Since, acquiring high class and large-size graphene is vital, secondary effect should be diminished.

1.1.2.2.3.1. Wet Ball Milling

In this method, van der Waals force of adjacent graphene flakes is broken by a surface energy between a "good" solvent and dispersed graphite. Various solvents are being used for this aim, such as DMF, NMP, tetramethylurea [139], a mixture of 1-pyrene carboxylic acid and methanol [140].

1.1.2.2.3.2. Dry Ball Milling

To produce graphene out of graphite by dry ball milling, a mixture of graphite and chemically stable inorganic salt is used. There is a large attraction between inorganic salt and graphene that makes the graphene layers to be shifted. As the inorganic salt is soluble in water, it will be removed from the product after washing it with water and graphene powder will be obtained Fig. 6c [141-144].
The main problem with ball milling is fragmentation and defects during the milling process that are not avoidable because of collisions among the grinding media.

1.1.2.2.4. Fluid Dynamics

Fluid dynamic method is another type of exfoliation to achieve graphene which is basically different from sonication and ball milling. It is performed by flowing a fluid, severely or mildly, on the graphite to exfoliate the graphene flakes repeatedly in different positions. The mechanism of exfoliation is the result of a normal-force that is generated by depressurization of penetrated supercritical fluid into the layer gap [131].

1.1.2.3. GO to rGO

Reducing graphene oxide is one of the typical ways to achieve high amounts of graphene and the produced material is called reduced graphene oxide (rGO) [145]. Graphite oxide or graphene oxide (GO) include numerous functional groups and they are produced by chemical oxidation of graphite by using various oxidants [146]. Hummer's method is one of the oxidation methods where graphite flake is dispersed in potassium permanganate ($KMnO_4$), sulphuric acid (H_2SO_4), and sodium nitrate ($NaNO_3$) solution [147, 148]. Reduced graphene oxide has a different structure from graphene oxide, because most of the functional groups are removed. Reducing graphene oxide results in some defects. Consequently, its electrical properties are lower than the mechanically exfoliated graphene. The reduction of graphene oxide is illustrated in Figure 7.

Several methods and reducing agents are used for reducing graphene oxide. In some studies, different reducing agents such as phenyl hydrazine [149], hydroxylamine [150], glucose [151], ascorbic acid [152], hydroquinone [153], alkaline solutions [154], and pyrrole [155] have been reported. In addition, a simple, one-step solvothermal reduction process [156] can also be used to obtain similar rGO. Electrochemical reduction is another process that is reported in several papers to synthesize graphene at large scale [157-159].

Since reduced graphene oxide is obtained by a cheaper and simpler process than exfoliated graphene, which by increasing the require for cheap and scalable devices, rGO is a good alternative [160].

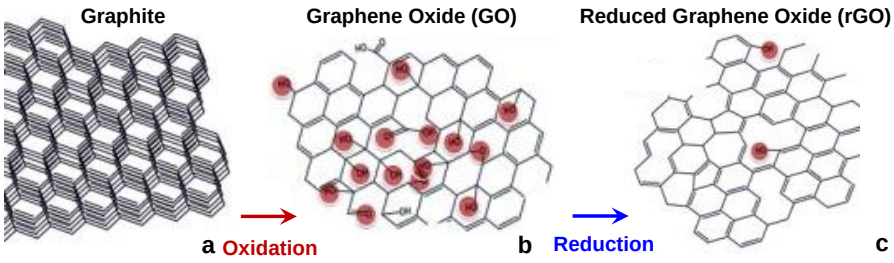

Figure 6. (a, b, c) The schematic diagram of reducing graphene oxide to develop reduced graphene oxide.

1.1.3. Characterization

Raman spectroscopy is a common testing and analysis technique in which doping, defects, disorder, chemical modifications, and edges are allowed to monitor. These make Raman spectroscopy a widely used tool to characterize graphene structures [161]. Raman spectra of graphene, as shown in Fig. 7a, contains three principal peaks which the position and intensity of each of them are representing a feature and containing some information. All sp2 bonded carbons show common features in their Raman spectra, called the G-band, 2D-band and D-band [162-164].

G band and 2D band are generally used to determine the number of graphene layers. G band is the main spectral feature of graphene that appears close to 1580 cm^{-1} and represents the planarly configured sp2 bonded carbon composing graphene. G-band is mainly used to find out the thickness of graphene layers. The position of the band and the shape might give a lot of information. Therefore, the band position needs to be considered as attempting to determine graphene layer thickness. Figure 8d demonstrates the relation between the position of the G-band and layer thickness. A shift in band position to lower energy happens when the thickness of layer increases. Also the intensity of G band has a direct and linear relation with the number of graphene layers (figures 7c, e) [165].

The D-band, which is a consequence of one phonon vibrational process, is directly proportional to the defects in a material. D band shows a disorder, or a defect related to dislocation of atoms in a lattice from the middle of the Brillouin zone. The band is weak in graphene, which gives a peak between 1270 cm^{-1} and 1450 cm^{-1}.

The 2D-band, which is a consequence of two phonon vibrational processes, is referred to as the second order of the D-band. However, unlike the D-band, it does not represent defects. The 2D band appears in 2700 cm^{-1} for a 514 nm and like G band indicates number of graphene layers but the frequency shift in it is not as simple as G band. Moreover, sharpness of 2D peak changes according to the number of layers, as the number of layers decreases sharper peak is obtained or vice versa as illustrated in Fig. 7c [166, 167].

Raman spectra of different types of graphene are shown in Fig. 7f. Study of peak status

and the ratio of I2D/IG in each graph, show the quality of each sample. In CVD grown graphene, the ratio of I2D/IG is about 2 which shows high quality and it could also be confirmed by the weak D peak at 1350 cm^{-1}. For the mechanical exfoliated graphene (G-ME) the ratio of I2D/IG is about half that along with the TEM & AFM results, it consists of few layers with defects in its structure [168].

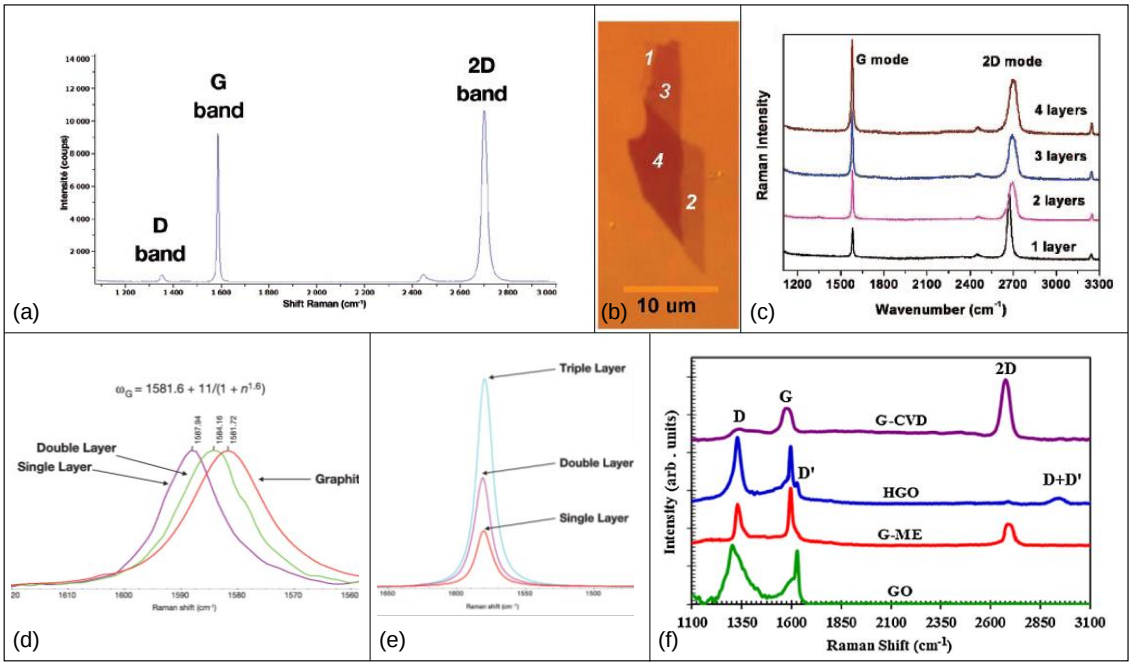

Figure 7. (a) Raman spectra at 514 nm for graphene [167]. (b) Colour optical images of graphene nanosheets with different thicknesses on SiO_2/Si. (c) Changes in the Raman spectrum of G and 2D mode of graphene, G mode gets sharper with increase in number of graphene layers [168]. (d) G-band shifts to lower energy as graphene layer thickness increases. (e) Intensity of G band increases as number of layers increases [169]. (f) Observation of the changes in Raman spectrum of G-CVD, HGO, G-ME and GO; the D-peak sharpened due to hydrogenation of graphene oxide, and the D' and D + D' peak appeared at 1630 cm-1 and around 2950 cm^{-1}, respectively [170].

The graph for graphene oxide illustrates no 2D peak and an intense D peak that show high defects and imperfections in the structure. Hydrogenating graphene oxide affects the D peak and makes it sharper. Moreover, two D' and D+D', that show structural characteristics of the hydrogenation of graphene, appear at 1630 cm^{-1} and 2950 cm^{-1}, respectively [171].

There is a type of scanning probe microscopy (SPM) in which the demonstrated resolution increases to a much higher level of a nanometer fractions that is much better ways compared to the optical diffraction limit, is named scanning force microscopy (SFM) or atomic force microscopy (AFM). Analysis data is collected by how the surface is being “touched” or “felt” with a mechanical probe. Gathering the data of different researches on graphene and results taken out by AFM, shows a thickness greater than theoretical value of a completely flat sp2-carbon atom network which is ~0.3 nm (figure 8) [172]. This difference is in consequence of various reasons such as the existence of oxygen in functional groups of epoxy and hydroxyl, instrumental error that results from the way AFM cantilever, graphene sheet and substrate interchange together, and inherent out-of-plane deformation of graphene sheet [154].

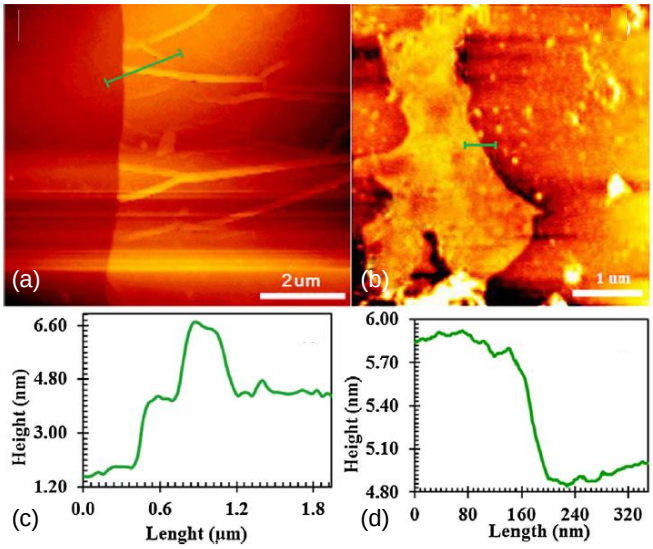

Figure 8. (a, b) Images of GO and G-ME taken with AFM. (c, d) The green paths in the images (a) and (b) utilized to get height profiles for GO and G-ME; the thicknesses are about 3.1 and 1.0 nm, respectively [170].

1.1.4. Graphene-Based Strain Gauges

1.1.4.1. Graphene and its application in sensors with GF as a performance characteristic

Gauge factor or strain factor of a strain gauge describes relative change in the electrical resistance, R, with respect to change in the strain, Ɛ. Most commercialized strain gauges are composed of resistors that are made from materials showing a strong piezoresistive effect. A perfect graphene has a low piezoresistive sensitivity due to its weak electrical conductivity response which is a result of structural deformation [173]. Graphene is brought together with its allied products; therefore, a great variety of gauge factors is obtained, which is associated with their sensitivity values. For example, combination of graphene with elastomer composites in strain sensor applications, where rubber is used as a substrate, have shown gauge factors ranging from 7 to 139 [174-176]. High-performance strain sensors that are composed of spray deposited graphene flakes by using methyl pyrrolidone solvent have reached gauge factors of 150 [107]. The percolation network design was used to clarify the film's characteristics. Another study measures gauge factor of 261 for a graphene based strain sensor with polydimethylsiloxane (PDMS) substrates [177]. Fu et al. produced highly sensitive strain sensor devices prepared by single layer CVD-grown graphene with measured GF of 151 [178], while in different study on CVD-graphene strain sensor a GF of 300 was successfully obtained [173]. Moreover, numerous results were obtained from reduced graphene oxide (rGO) based sensors that were using different substrates. For example, in strain sensors with graphene oxide that is reduced by laser and deposited on a polyethylene terephthalate (PET) substrate, gauge factors ranging from 7.1 to 62 are achieved [179, 180]. rGO and silver nano- composite based strain sensors in which kapton or polyimide has been chosen as a substrate achieved gauge factors of 12 [181-183], whereas the rGO based strain sensors on paper substrates have gauge factors around 67 [160, 184, 185].

Table 2. The comparison of gauge factors of different graphene-based sensors

Ref.	Test Device	Piezoresistive Ceofficient kPa^{-1}	Gauge Factor	Sensing Strain Range
[186]	Graphene ripple		-2	30%
[187]	Suspended graphene ribbon		1.9	3%
[174]	Graphene glow sensor		2.4	2%
[107]	Percolative graphene film		15	1.7%
[185]	Graphene nanopaper		1.6, 7.1	100%
[188]	Graphene based on yarns		1.4	150%
[189]	Graphene woven fabric		106	30%
[190]	Graphene foam		2.4, 15	77%
[191]	Graphene/CNT composite		100	40%

[192]	Graphene/PVDF composite		12.1	0.1
[193]	Graphene tactile sensor		2.1	-
[194]	Micro-structured graphene array	-5.53, -0.01		1.4 kPa
[180]	Laser-scribed graphene	-0.96, -0.005		113 kPa
[195]	Double-layered graphene	-0.24, 0.039		10 kPa
[196]	RGO film	40.9, 0.007		20 kPa
[197]	Piezopotential powered sensor		389.69	0.3%
[198]	PDMS-cellulose-rGO/CNFs hybrids		9.4	70%
[199]	Polyurethane-silver nanowires/graphene hybrids		20-400	2%
[200]	SWCNT/graphite nanoplatelet hybrid film		8	-
[201]	Graphene wrapped CNTs		20	1.2%
[202]	PDMS-graphene nanoplatelet/CNT hybrids		1000	18%
[203]	3D porous PDMS CNT/rGO hybrid		1.6	80%
[204]	PDMS graphene reinforced CNT network		0.36	-
[205]	Polyurethane CNT/graphene		5.1-152.9	90%
[206]	Carbon nanotube-graphene nanoplatelet hybrid film		<1	-
[21]	rGO-conductive cotton fabric on wrist		-	0.02-0.35%
[185]	Graphene-crumpled graphene on finger		-7.1	100%
[207]	rGO-fish scale like on wrist and neck		16	82%
[208]	rGO-FET on thumb		20	50%
[209]	Graphene-graphene woven fabric on finger		223	3%
[210]	rGO-microtube on wrist and neck		630	50%
[211]	Graphene-printed fragments		125	0.3%
[212]	Graphene-nano graphene sheets on finger		500	1.0%
[213]	Graphene-single layer graphene on finger		42.2	20%
[214]	rGO-PS nanoparticles doped rGO on back and neck		250	1.05%

1.1.5. Sensing Applications of Graphene

Recently, graphene has gained interest in sensing applications due to its remarkable characteristics like excellent thermal stability, large surface area, large carrier mobility at room temperature, ballistic conductivity, robust mechanical strength, and small electrical noise [14, 189, 210, 215-217]. Following these features of graphene, three different sensing mechanisms were proposed to make three types of graphene-based sensors, which are shown schematically in the Fig. 9. Some studies reported graphene-based electrochemical sensors that can be used to recognize harmful ingredients like hydrazine, and to detect haemoglobin, adenine dinucleotide and biomolecules, such as ascorbic acid and uric acid due to their selective detection mechanisms [218-222]. Moreover, graphene-based sensors have been successfully shown for biomolecular, physical, and chemical sensing [223]. In addition to its great sensitivity, the simple design and

adaptability to mass production are some of the benefits that make the graphene-based electrical sensors pioneer for such kinds of applications.

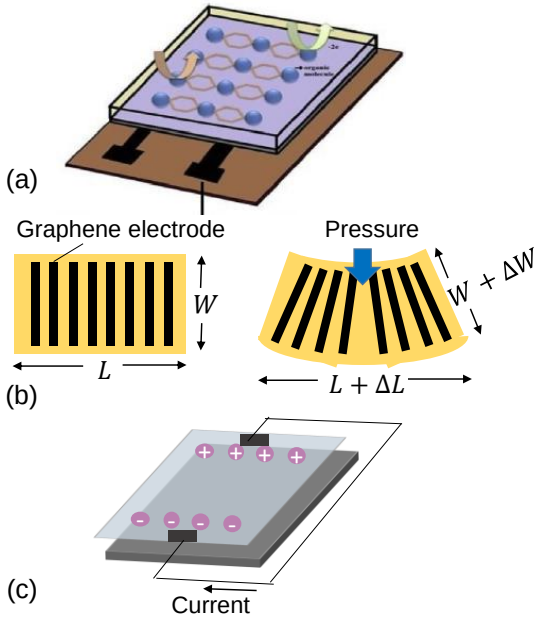

Figure 9. Schematic representation of the graphene-based (a) electrochemical (b) strain (c) electrical sensors' sensing mechanisms [224].

To date, there have been many different materials which were used to formulate and develop strain sensors. The graphene-based sensors have shown excellent properties as highly potential candidates for strain-sensing applications among the others. The striking feature of using graphene upon conductive materials for strain sensing originates from the generation of a pseudo-magnetic field because of the change in the Dirac cones and reduction of the Fermi velocity. The magnetic field is utilized to distinguish the change in electronic structure during strain. The efficiency of fabricated strain sensors is attributed to the gauge factor (GF), which calculates the resistance change due to mechanical deformations. Normally, the fabrication of graphene-based strain sensors requires combining a composition of various materials in it, which the gauge factors determine the amount of strain should be taken into account for the material.

In strain sensors, graphene has been used as electrode because of its high surface conductivity and high elastic stiffness and strength due to high Young's modulus. The structural strength and load transfer capabilities are two main assets of graphene, making it a perfect candidate to combine with conductive materials such as CNTs and polymers

like PDMS, PMMA, in order to enhance the capability to endure big cyclic strains above 50% without altering its characteristics such as sensitivity, response and durability [224].

Graphene composites have been used in a couple of strain sensors with high reported GF [107, 175]. Plenty of research groups have studied on developing graphene films on polymers such as PDMS, Polyethylene terephthalate (PET) and Polyimide (PI) [174, 183, 225], and they worked on obtaining a piezoresistive effect by inducing the changes in resistance within a non-monotonic regime with the applied stress. Fig. 10 (a, b, c) illustrate three different types of graphene-based polymeric strain sensors prepared with photolithography, drop-casting, and thermal annealing processes, respectively. Graphene nano-papers, as another form of graphene, were also utilized in order to enhance strain sensors [185, 226, 227]. Fig. 10d illustrates the schematic diagram showing the fabrication of nano-cellulose based sensor patch [185].

Strain sensors have been utilized in a wide range of applications. Some of these applications have already been put into practice. In healthcare devices, the strain sensors have been integrated to the gloves, organs, and skins [228] to display physiological activities of the human body. Another study aimed investigating a device to detect and identify sound signals by the help of strain sensing mechanism of the graphene woven fabric (GWF)-based sensor with PDMS substrate [60-62, 167, 168, 170-172]. The sensor patch was placed on throat muscles to interpret the changes in the resistance as a response to muscle movement. The sensor gave different responses for each English phoneme which were analysed to distinguish outputs. Different words were also used to confirm the reliability of the developed sensor. Graphene films show a gauge factor in the range of 1.9 to 6 [187, 229] thus, in order meet the expectations of the standards in a high-performance strain/tactile sensors, a sensor design has been investigated to specialize the sensors in terms of high sensitivity, repeatability, wide range of working areas, and ability to detect the direction of force. Accordingly, numerous types of sensor structures that conduction mechanisms differ in each such as a rosette type gauge arrangement [174], percolative film [107], nano-paper [185], woven fabric [189], foam [190], and micro structured arrays [194] have been suggested. Table 2 also shows the properties of graphene-based tactile and strain sensors according to the conduction mechanisms, piezoresistive coefficients, gauge factors, response types, and sensing ranges.

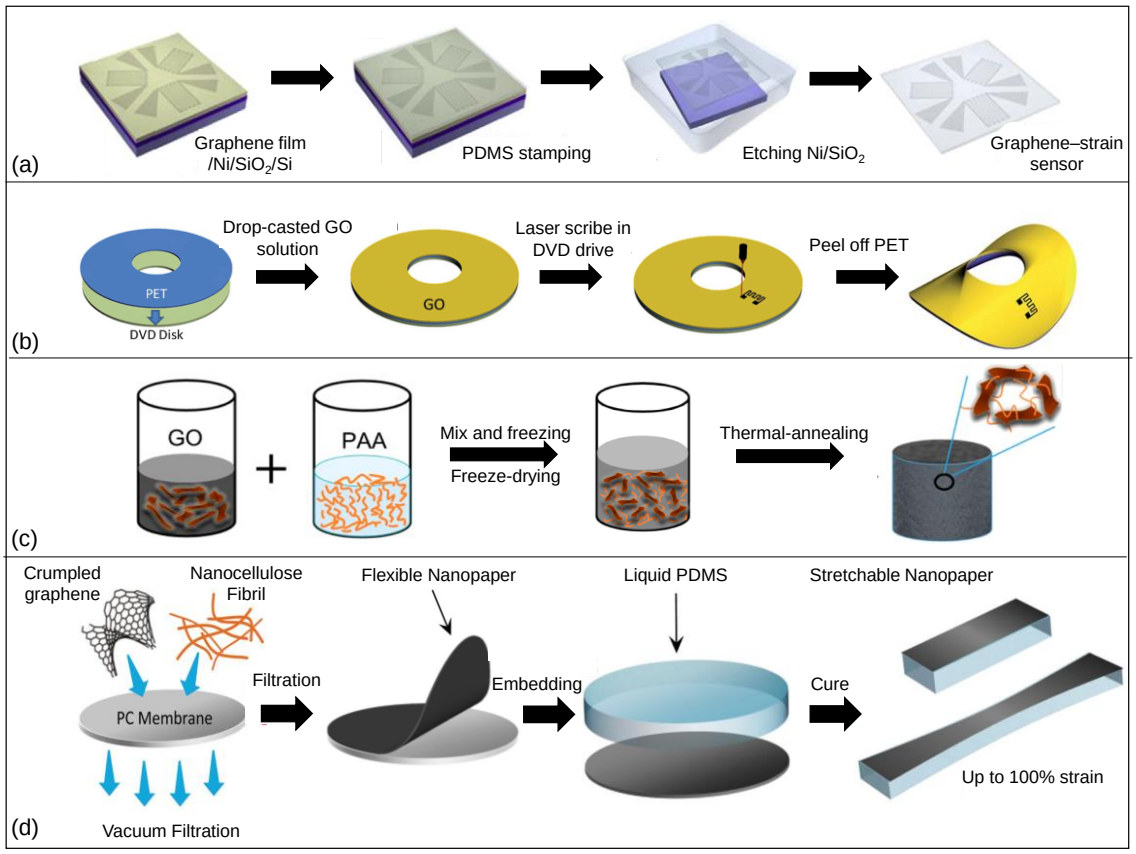

Figure 10. (a) Fabrication of graphene-based strain sensor with PDMS stamping method on Ni/Si/SiO2 film [174]. (b) Fabrication of a flexible strain sensor on PET by drop-casting method and making integrated circuit by laser write on it [225]. (c) Nanocomposite based strain sensor with reduced graphene oxide/polyimide prepared by mixing, freezing, and thermal annealing with polyamic acid [183]. d) Schematic representation of the development of stretchable graphene nano-papers [185].

A single strain gauge is typically capable of measuring the strain that has the same direction with its gauge positioning [228]. Since recognizing the principal strain directions on human skin is generally impractical, it is not easy the predominant strain to be measured directly. That is why the alignment of a strain sensor within the direction of the strain makes it enable to give immediate response to the bending of a finger. Fig. 11a demonstrates a graphene based glove sensor in rosette form that was used to sense the direction and magnitude of the predominant strains. It also shows good durability and recovery under consecutive bending and straightening of a finger as shown in the Fig. 11a. In this application, as it has illustrated in Fig. 11b, a graphene-based rosette gauge

including three gauge mounted on the backside of the finger. There are some changes occurred in a normalized resistance value when the rosette gauge is stretched. Both the applied force and the direction of the strain are detected at the same time by using the three strain gauges in the rosette arrangement. Both the magnitude of applied force and the direction of major strains on the skin are detected at the same time by setting the strain gauges in the rosette arrangement. However there is still a restriction about measuring significant amount of strains of above 50% generated that is resulted in by stretching and contracting motions in human joints. On the other hand, nano-papers might be a solution in terms of detecting a strain of over 100% as shown in Fig. 11c. It is three-dimensional, highly stretchable, and composed of wrinkled graphene and nanocellulose. In Fig. 11d, the corresponding values are shown on the chart presenting the changes in the relative resistance with respect to a strain up to 100%. A gauge factor is 7.1 when the resistance change reached 710% at 100% of strain. The amount of gauge factor seems 10 times higher compared to 1D materials like CNTs and AgNWs having a similar device arrangement. Fig. 11e demonstrates nano-paper based strain sensors on a rubber glove as a possible real-life application of wearable sensors in order to detect the movements of fingers. In Fig. 11f, the sensors placed on gloves can clearly measure the motions of fingers by bending and stretching repetitively at a frequency of 1 Hz, and it also displays great sensitivity in a wide range of deformations as shown in Fig. 11f. Besides, the solution process-based fabrication method makes the strain gauge advantageous in low cost and mass production.

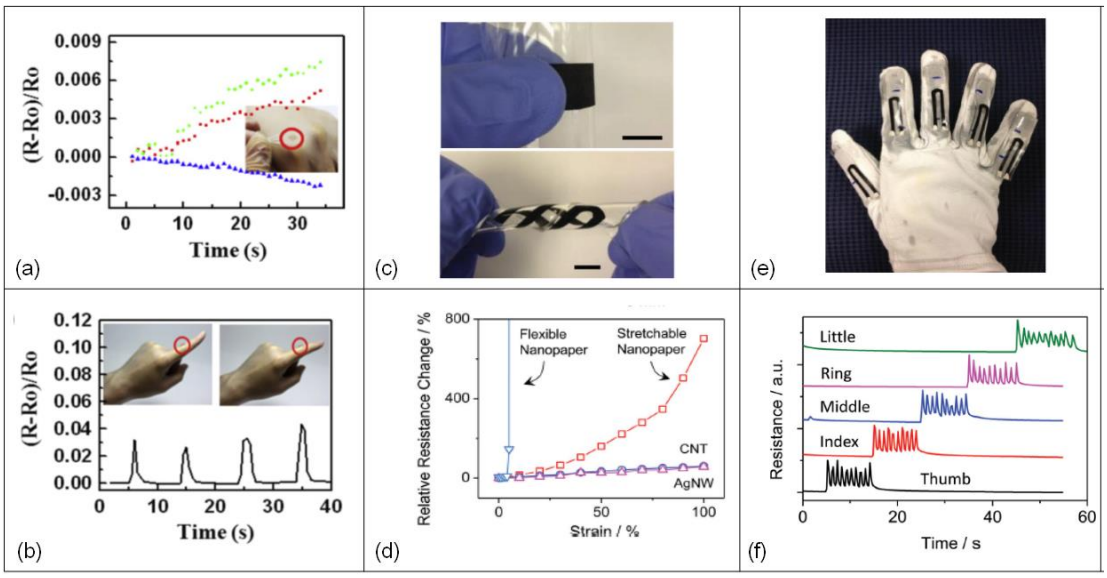

Figure 11. (a) Observation of relative resistance changes in the strain sensor on a glove when the finger bends or unbends. (b) Using a rosette gauge on the glove to detect the direction of principal strain by applying stretch gently. (c) Pictures of stretchable graphene nanopaper made up of crumpled graphene and nanocellulose. (d) Relative resistance changes of stretchable, flexible nanopaper, CNT and AgNW with respect to the applied strain up to 100% in the form of stretch (e) Application of graphene nanopaper-based sensors on a glove is imaged. (f) Transitions between the corresponding resistance changes of the strain sensor by the motion of each of the fingers [174, 185].

1.1.5.1. Wearable Strain Sensor

Wearable electronics are being utilized with various applications for the human body, such as monitoring heart rate, blood pressure, wrist pulse, intraocular pressure, motion to name a few. The strain sensor is the most important application among the others. It is used to monitor different types of human body's motion such as vibration of vocal cords and movement of joints. Therefore, strain sensors are required to be flexible and stretchable materials to meet the demands. Piezoresistive strain sensors detect deformations over resistance change due to noncontinuous path in the network geometry or cracks occurring when conductive nanomaterials, such as metal nanowires (mNWs), graphene flakes or films, and CNTs, are deformed during stretching or bending [175, 184, 189, 230-232]. Graphene woven fabric (GWF) used as a strain sensor was shown in Fig. 12a. The sensor had gauge factors of 10^3 when the strain was in the range of 2-6%, and it has shown gauge factor of 10^6 when the strain was higher than the previous case (>7%) due to the fact that the density of cracks was generated higher with stretching than that of bending (figure 12b) [189].

1.1.5.2. Bluetooth Integrated Sensors

In wearable technologies, information about people's bodily status and motion activities in real time can be exchanged mutually between the monitoring systems and devices [233]. The sensors connected in Bluetooth systems can measure the exchange of information upon mutual transfers [234-236]. Bluetooth is distinguished from other

wireless systems due to its inexpensive, low power, and data transmission at maximum level with the rate of 24 MB/s up to a distance of 100 m. Fig. 12e shows a flexible strain sensor using combination of carbon nanotube and rGO as electrodes and ZnO nanowires as the active layer channel. The sensor equipped with a Bluetooth module was used to detect real-time changes in the strain due to the subject's movements. Fig. 12e shows the sensor attached to the subject's wear; as the subject bends an arm, the sensing results were displayed on a smartphone. The integration of Bluetooth modules has broadened the wearable strain sensor's applications ranging from healthcare to aeronautic [237].

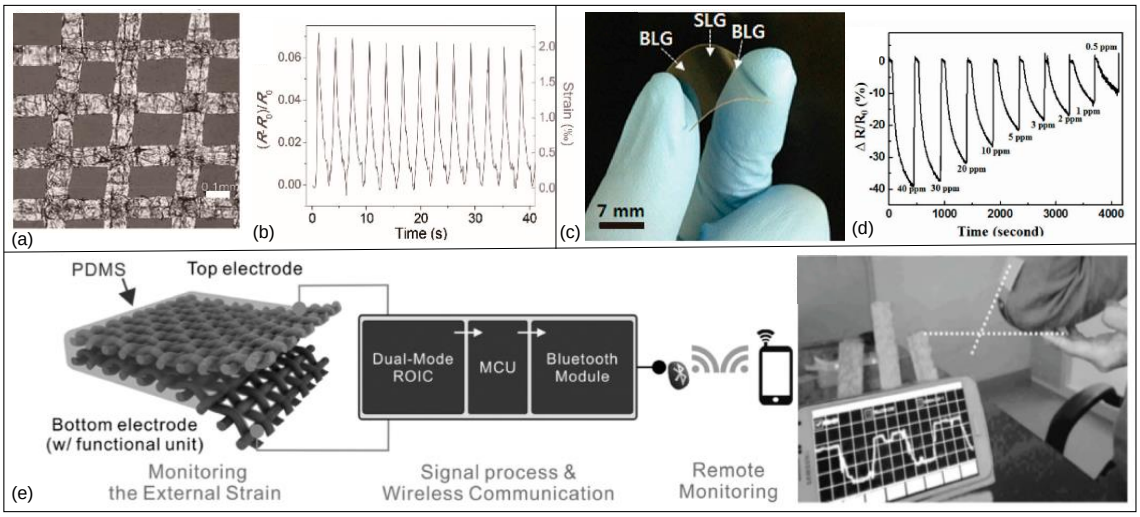

Figure 12. (a) Optic microscope image of a composite film composing of graphene woven fabrics (GWFs) and PDMS. (b) Plot of relative resistance change as a function of applied strain varying among 0% and 0.2%. (c) Picture of transparent and flexible single-layer graphene (SLG) sensor with bilayer graphene channel (BLG) as a heater on polyethersulfone (PES) body. (d) Observation of the relative change of resistance of SLG channels with respect to time. (e) A flexible strain sensor based on textile integrating with a monitoring system. Pictures of the textile based strain sensor integrated with Bluetooth device enabling for instantaneous operation over mobile phone, a remote monitoring device.

2. MEMS-BASED STRAIN SENSORS AND FUNDAMENTAL PRINCIPLES

Over the last decade, MEMS technology have been presented in the field of physical sensing and have enabled to produce small, robust, and inexpensive devices like accelerometers, gyroscopes, pressure sensors, and strain gauges. High sensitivity, good scaling features, and low cost are advantages offered by MEMS piezoresistive strain sensors.

A strain gauge or strain sensor is a device used to measure the distortions experienced by a component as a result of applied stress. A strain gauge is composed of different materials such as metals and semiconductors, which are utilized as sensing materials in order to convert strain or deformation into electrical signal. Therefore, the electrical resistance of a sensing material changes when a strain gauge experiences strain or deformation under applied stress, which is known as piezoresistivity. In 1856, Lord Kelvin was the first to discover the piezoresistive effect, which is a commonly used sensor principle. The piezoresistive effect allows transducing energy/signal easily and directly through the electrical and mechanical domains. Over the years, it has been utilized in the MEMS sensor applications ranging from pressure sensors to sensors for observing structural unity of mechanical constituents [238].

A typical strain gauge is constituted of a metallic foil pattern and a flexile backing that provides mechanical durability shown in Fig. 13. A conductor or semiconductor material that is typically used in a strain gauge is directly fabricated on the sensor or attached with the sensor. When the sensor is attached to a body or an object, and at the moment that the body or the object is deformed, the foil is also deformed, thus causing changes in the electrical resistance of the foil.

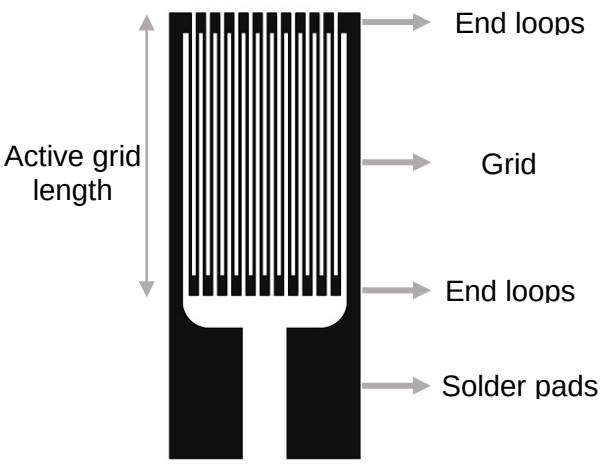

Figure 13. Typical design of a metallic strain gauge

The resistance value is defined with the length being *l* and the cross-sectional area *A* is given by

$$R = \rho \times \frac{l}{A} \tag{1}$$

where the resistivity of material (ρ) and the dimensions are two factors determining the resistance value.

The macroscopic definition of the behavior of a piezoresistor under a normal strain gives the relation between the strain and the electrical resistance change is as follows

$$\frac{\Delta R}{R} = GF \times \frac{\Delta L}{L} \tag{2}$$

where $\Delta R/R$ is the normalized fluctuation in resistance; $\mathcal{E}$ represents strain. The resistance change is linearly related to the applied strain, and *GF* as the proportional constant in the above equation is called the gauge factor of a piezoresistive material, then the equation is rearranged in order to define *GF* value explicitly as the following

$$GF = \frac{\Delta R/R}{\varepsilon} \quad (3)$$

2.1. Polymeric Cantilever Platform-Based Sensors

Over the past decade, micro-/nanoelectromechanical systems (MEMS/NEMS) technology has made great progress in developing novel investigation and diagnostic tools for different applications. The improvements in science on nano and micro scales, and in micro- and nano-fabrication technologies have paved the way for permanent development in the area of MEMS/NEMS [239-249]. MEMS-/NEMS-based cantilever sensors promise advantages in compactness, and they also show better sensitivity. Furthermore, they have lower detection limits, and are cost-effective. Besides, they are real-time operating systems. These features make the MEMS-/NEMS-based cantilever sensors practicable and alternative solutions for possible limitations in sensing applications, which will be mentioned in the next chapters, as the classical analyzing tools could not overcome [250].

In cantilever-based strain sensors, a conductive material shows a change in its electrical resistance owing to a stress. The deformation experienced by cantilever platforms is converted into a corresponding electrical signal, which is used to evaluate the change in electrical resistance of cantilever-based strain sensors. Therefore, stress-induced variations in the body of the cantilever are revealed in two forms: observing frequency change in its resonant in dynamic mode or cantilever displacement in static mode. In the latter case, conversion of stress-induced changes in electrical resistance of the cantilever into an corresponding electric signal is achieved in three separate techniques: optical [251]; piezoelectric [252], piezoresistive [253], and capacitive [254] as electrical readout methods. Piezoresistive readout is the most ideal choice among the electrical readout techniques such that it is compact and easy to scale. It also provides a wider dynamic range. Besides, it can be used in a wide range of operation. Moreover, it is independent from an operational medium, and enables for detecting without using label. Furthermore, it provides compliance of on-chip or off-chip signal processing circuit, and shows

compatibility with the fabrication process flow of integrated circuit (IC). Therefore, these advantages promised by the piezoresistive readout make breakthrough in sensors technology in terms of ability to sense, be compact, and be multi-functional.

AFMs were the first example of the micro-cantilever platforms utilized as a surface imaging tool. First AFMs were solid-state semiconductors based. On the other hand, over the years, semiconductor [109, 255-261], metal [58], ceramic [262], plastic/polymer [263, 264] have become alternative materials. Semiconductor-based devices were not cost-effective, thereby limiting its potential, therefore researchers have made a great effort to explore an alternative material to semiconductors. Piezoresistive cantilever sensors based on SU-8 polymer provide advantages in performance-to-cost ratio compared to the semiconductor counterparts.

In a decade, the studies have reported the cantilevers as sensing platforms within the concept of development and performance characterization [265-270]. In addition, researchers have planned to make progresses in polymer micro-machining [271] and polymer MEMS [272]. Even though, there have been studies of MEMS piezoresistive polymeric cantilevers within the aspects of development and performance, however a minority of researchers have reported sensors with SU-8 [273, 274]. The articles report the advancement in cantilever type piezoresistive stress sensors based on SU-8, and they also criticize the modification of semiconductor-based cantilevers to polymer-based cantilevers, and the versions of cantilevers based on SU-8 are investigated in accordance with material, design, and fabrication aspects.

2.1.1. Typical Device Details and Working Principle

Cantilever type sensors are functioned in mode of statistic where the net deflection experienced by the cantilever is attributed to the applied stress. Generically, SU-8 cantilever sensors are composed of three layers: a main platform, transmission element, and operational layers, which are seen at the top and cross-sectional as Fig. 14 illustrates. The layers of the sensor constitute metal layer(s) served as a building layer and a piezoresistor. Generally, a rectangular shape cantilever can be figured with a piezoresistive layer in U form on top, however the geometry of cantilever and the shape

of piezoresistor are customized according to a type of piezoresistive material, fabrication process, and application. For example, metal, p-type or n-type polysilicon, and polymer with dopants can be given as an example of piezoresistive materials.

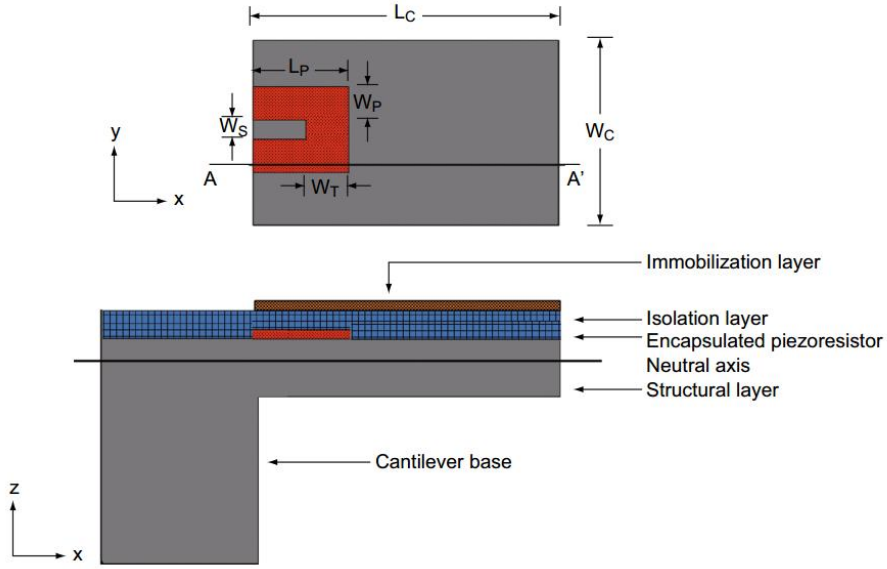

Figure 14. A microcantilever type piezoresistive polymer sensor in composite structure [275].

In the literature, the chain of geometrical comparisons of solid-state semiconductor cantilever sensors based on SU-8 has been reported. SU-8 polymeric cantilevers are generically made up of either three- or four-layered structures, whereas cantilevers based on silicon are two- or three-laminated structures. Besides, the piezoresistor in SU-8 cantilevers is either deposited or spin-coated, but the piezoresistor of silicon cantilevers is obtained using diffusion or ion-implementation technique. When the performance characteristics of both SU-8 cantilevers and silicon cantilevers are considered, they provide similar electrical sensitivity by optimizing the geometry. Moreover, characteristics of the cantilevers are specified according to both component material set and fabrication techniques. For instance, traditional fabrication techniques are followed to produce silicon cantilever sensors that can show good compatibility with CMOS based on-chip signal processing. Over the last years, the reports about improvements in the performance of the cantilever sensors based on silicon have been released by state-of-the-art engineering techniques [276-284]. Silicon cantilevers show outstanding stability toward moisture and better thermal stability. However, SU-8 cantilevers are vulnerable against moisture and differences in temperature. On the other hand, due to low material and fabrication cost, cantilevers based on SU-8 demonstrate comparatively the high ratio

of performance to cost.

A mechanical platform comprises the structural layer of the cantilever, which is not only for providing mechanical resilience against applied stress, but is also for serving as a stress collector. Piezoresistive layer, which is used to read structural deformation in the form of a corresponding electrical signal is deposited at top side of the sensor or embedded into the structural layer by dopping.

Basic microfabrication techniques include spin coat, metal depositing, photolithography, and metal etching that are utilized in order to fabricate SU-8 piezoresistove sensors. A Wheatstone bridge (WSB) is used in the case of deducing cross talk and improving signal to noise ratio (SNR). Therefore, cantilever type piezoresistive sensors based on SU-8 are cabled to WSB shown in Fig. 17. SEM images of a cantilever based on SU-8 with its cantilevers in an array form and cross section are shown in Fig. 15 [285]. Fig. 16 shows the device chips in an array format at wafer level and specific components of piezoresistive cantilevers based on SU-8, where carbon black (CB) is used as a doping material for each device chip. In Fig. 17, the cantilever sensor based on SU-8 in zig-zag form gold as a piezoresistive material is picturized. It may be noted that serpentine shape of peizoresistors is utilized deliberately, which results in increasing the resistance of the piezoresistive material from its nominal value when metal piezoresistors are used. The graphical representation of a WSB-based circuitry is also shown, in which the measuring cantilever forms one side of the bridge and on-chip resistors and the reference cantilever form the other side of the bridge.

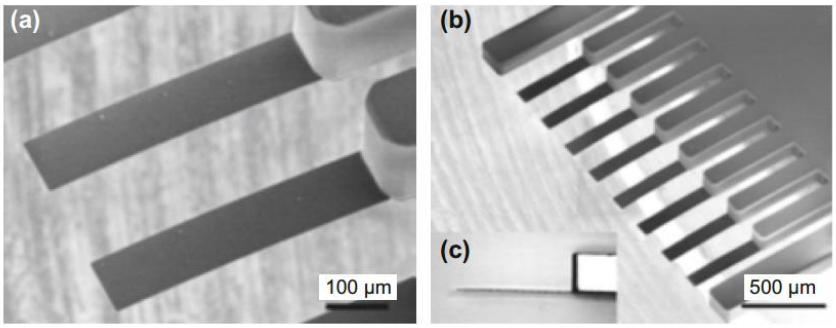

Figure 15. SEM images of the cantilever sensor based on SU-8 in the form of arrays: a and b show a SU-8 cantilever at different magnification rate; c is side view of the cantilever [300].

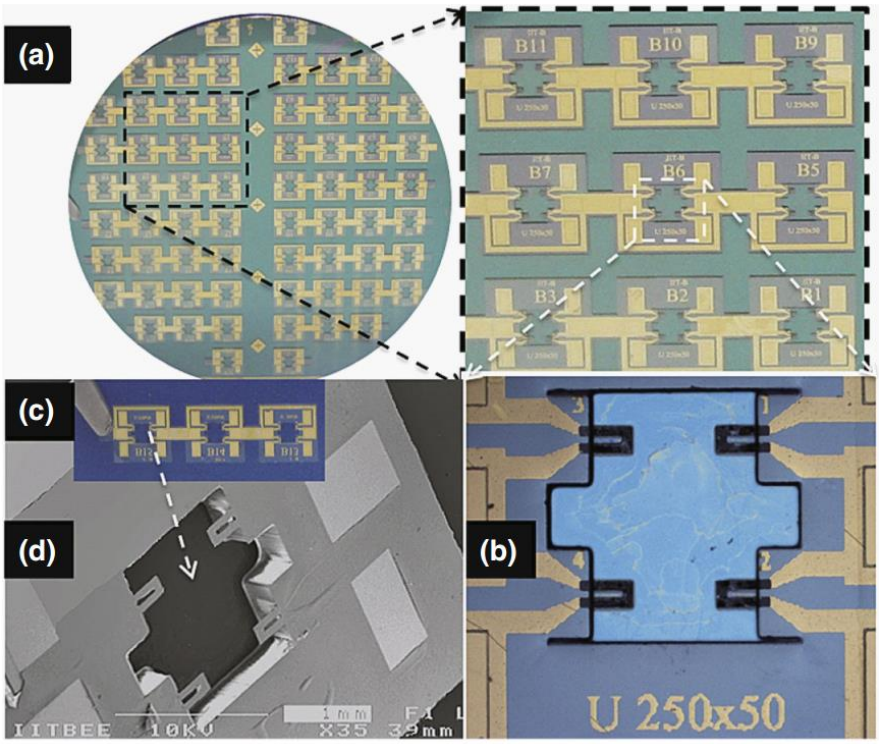

Figure 16. The piezoresistive sensors based on SU-8: (a) the sensor arrays of the silicon wafer prior to release; (b) four rectangular cantilevers shown in the array of the device chips; (c,d) the sensors after the separation [286].

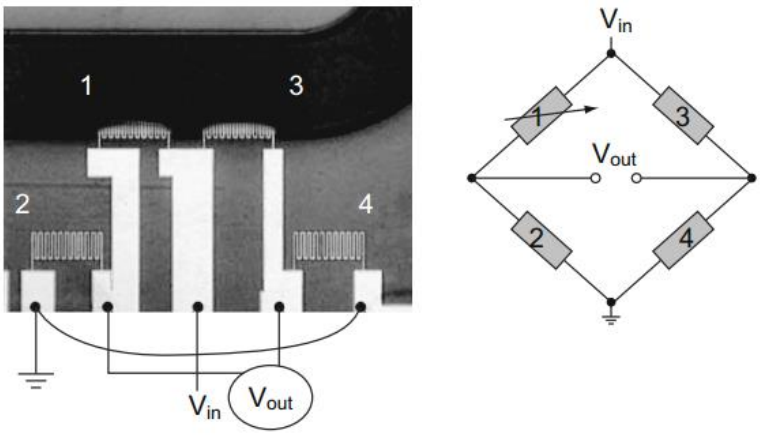

Figure 17. Optical microscope image of a zig-zag shape cantilever with Au piezoresistive material based on SU-8 wired into a WSB configuration [287].

The stress is concentrated at the anchored edge of the cantilever, where the piezoresistor pattern is placed, hence maximizing the electrical sensitivity. One tip of the cantilever is anchored, and the other tip remains free, then an applied force at the tip generates tension at top side of the fixed end leading to bend the structure down, which either increase (*+ΔR)* or decrease (*-ΔR)* in the nominal resistance of the piezoresistor. As the cantilever forms one side of a balanced WSB, there is a voltage output in WSB circuit as a result of nominal resistance change of the piezoresistive cantilever, which corresponds to the amount of surface stress that is generated on the cantilever surface due to the mechanical loading.

2.1.2. Adventure of Sensors from Semiconductors to Cantilevers in Polymeric Form

Silicon and its different versions have been commonly used in fisrt MEMS cantilever sensors. Table 3 summarizes cantilever platform sensors evolved in time, which includes studies of different cantilever sensors. Atomic force microscopes (AFMs) were considered as initial examples of miniaturized cantilevers functionalized for applications to image topographically by Binning et al. [288]. They have reported that AFM was composed of a cantilever in rectangular form with a sharp triangular end enabling for height measurement on topology of a surface with atomic level resolution.

Table 3. The adventure of cantilever sensors on micro and nano scales

Material set	Component layers	Readout method	Applications
Cantilever Au, tip diamond	Structural layer: Au	Tunneling current	AFM topological measurement
Cantilever Si, Al + Pt coating	Additional layer: Al + Pt	Optical	Calorimeter-based chemical sensing
Cantilever Si/Si_3N_4 + Au/Al coating	Additional layer: Au/Al Structural layer: Si/Si_3N_4	Optical	Humidity and mercury vapor sensing
Cantilever Si_3N_4 + Au/Pt coating	Structural layer: Si_3N_4 Additional layer: Au/Pt	Optical	Measurement of electrochemically induced surface stress
Cantilever Si, pieozresistor doped Si	Immobilization layer: gold/polymer Protective layer: SiO_2 Piezoresistive layer: p-poly-Si Isolation layer: SiO_2 Structural layer: Si	Piezoresistive	Temperature, humidity, and alcohol sensing

Cantilever SU-8, piezoresistor Au	Immobilization + isolation layer: SU-8, Piezoresistor layer: Au Structural layer: SU-8	Piezoresistive	Surface micro-machining
Cantilever Si_3N_4, piezoresistor doped polysilicon	Immobilization layer: Au Isolation layer: SiN_x Piezoresistor layer: p-poly-Si, Structural layer: SiN_x	Piezoresistive	ssDNA sensing Bulk + surface micro-machining
Cantilever SU-8, piezoresistor CB SU-8	Isolation layer: SU-8 Piezoresistor layer: CB SU-8 Structural layer: SU-8	Piezoresistive	Surface micro-machining
Cantilever SiO_2, piezoresistor p-SCS	Immobilization layer: Au Isolation layer: SiO_2 Piezoresistor layer: p-SCS Structural layer: SiO_2	Piezoresistive	Methyl-phosphonate sensing Bulk micro-machining
Cantilever SU-8, piezoresistor p-poly-Si	Immobilization + isolation layer: SU-8 Piezoresistive layer: p-poly-Si, Structural layer: SU-8	Piezoresistive	Surface micro-machining, HWCVD
Cantilever SU-8, piezoresistor CB SU-8	Immobilization + isolation layer: SU-8 Piezoresistive layer: CB SU-8 Structural layer: SU-8	Piezoresistive	Surface micro-machining
Cantilever SU-8, piezoresistor CB SU-8	Immobilization + isolation layer: SU-8 Piezoresistive layer: CB SU-8 Structural layer: SU-8	Piezoresistive	CO sensing Surface micro-machining
Cantilever SU-8, piezoresistor CB SU-8	Immobilization + isolation layer: SU-8 Piezoresistive layer: CB SU-8 Structural layer: SU-8 Prohibition layer: Au	Piezoresistive	Soil moisture and relative humidity (RH) sensing Surface micro-machining

Optics or resonant frequency shift readout systems were utilized in the first AFMs and cantilever type sensors, in which a laser beam is used to detect shifts in the position of the cantilever, and a photo detector measures the shift, then a piezoelectric actuation system measures changes in the shift of cantilever's resonant frequency. Even though aforementioned readout systems were able to show cantilever displacement resolution in nanometer (nm) range [289], they were useless in vacuum and air operational medium meaning that they are incapable of measuring in liquid platform due to the fact that fluid causes damping effect. Also, they are useless in opaque liquid medium, and are bulky for measurement setup. Besides, they are required to realign and recalibrate continuously. On the other hand, self-sensing piezoresistive readout technique has been discovered in 1990s, and implemented to eliminate the constraints shown by resonant frequency- or

optic-based readout systems. In 1991, Tortonese et al. was the first group that utilized piezoresistive readout in AFM cantilevers [290]. Piezoresistive readout shows better performance than other readout methods such as capacitive [291], piezoelectric [292], tunneling [293], and integrated optical waveguide [294].

In the past decade, single crystal silicon (SCS), poly-Si, and metals doped semiconductor cantilever sensors of Silicon (Si) [295-300], silicon nitride (Si_3N_4) [301-304], and silicon dioxide (SiO_2) [305-311] have existed. In solid-state semiconductor cantilever sensors are generically composed of a structural layer and the piezoresistor element. Si, Si_3N_4, SiO_2 are typical materials used as the structural layer, and gold, doped silicon, or doped polysilicon forms piezoresistive layer. Cantilever sensors based on semiconductors promise low-cost fabrication since they are compatible with batch manufacturing. However, they are unfunctional and limited since they require huge amount of expenses due to the requirement of cleanroom infrastructure and big payments for devices. Therefore, researchers have focused intensely on these issues, and they tried to resolve by finding an alternative material that could exhibit the same performance as semiconductor sensors has shown in regards to reducing fabrication and material cost.

Ceramic, metal, silicon carbide, diamond, and graphene have been typial materials utlized in MEMS devices, however their feasiblity as piezoresistive-based sensors are limited due to the fact that these materials are highly stiff and expensive, and they also require complex fabrication processes. On the other hand, polymers are alternative materials for being utilized in MEMS-based devices since they offer Young's modulus at low level, they are biocompatible and cost-effective as well, with regards to both material and fabrication. In 1994, Pechmann et al. reported the first study on polymeric cantilever devices composed of a novolak photoresist that was the first photoresist-based sensors at its time. In the following years, parylene [312], PP [313], fluoropolymer [314], SU-8 [315], PET [316], PI [317], TOPAS [318], PS [319], PDMS [320], and PMMA [321] have been broadly utilized in fabricating miniaturized devices. In Table 4, an overview above-mentioned polymer is presented in terms of their material properties, fabrication process, and MEMS applications.

Table 4. General view of several polymers with their corresponding fabrication process, properties, and area of use [275].

Polymeric material	Fabrication process	Properties	Area of use
Parylene	CVD Oxygen plasma etching Lithography	E (Young's modulus) ~ 5 GPa Chemically stable Low intrinsic stress Hydrophobicity Transparency Temperature-sensitive	Electrostatic actuator Micro-valve Spring Electrostatic micro-peristaltic pump
PP	Injection molding Laser ablation	E (Young's modulus) ~ 1.45 GPa Sensitive to oxidants Thermally resistive High thermal coefficient of expansion (TCE) Opaque	Surface stress cantilever sensor Component in air-coupled piezoelectric transducer Piezo-electric film transducer
Fluoropolymer	Spin coating Ion beam sputter etching Magnetically controlled reactive ion etching	E (Young's modulus) ~ 1.45 GPa (Teflon) Chemically stable Hydrophobicity Thermal stable	AFM-based biochemical sensor Micro-tube Micro-fluidic channel
SU-8	Spin coating Photolithography Excimer laser patterning Dry etching	E (Young's modulus) ~ 5 GPa Low molecular weight Chemically stable High refractive index Biocompatible	Optical waveguide Micro-needles Micro-resonator AFM cantilever Surface stress cantilever sensor
PET	Excimer laser patterning and laser ablation	E (Young's modulus) ~ 2.8 GPa Moisture resistant Fracture and deformation resistant	Cantilever biosensor Mechanical susbtrate Micro-pump
PI	Spin coating Dry etching using oxygen Lithography	E (Young's modulus) ~ 7.5 GPa Chemically staable Stable at high temperature and heat Sensitive to alkalis Low vulnerability to moisture	Scanning probe Tactile sensor Humidity sensor Micro-channels
TOPAS	Spin coating Nano-imprint lithography	E (Young's modulus) ~ 3.5 GPa High chemical stability Low vulnerability to moisture Good optical transmission	Water vapor sensor Optical waveguide Micro-fluidic devices
PS	Injection molding Solvent casting technique	E (Young's modulus) ~ 3.0 GPa Sensitive to moisture Optical transparency	Surface stress sensor Accelerometer
PDMS	Spin coating Cast molding	E (Young's modulus) ~ 0.75 MPa Incompatible with organic solvents Optical transparency	Micro-valve Magnetic actuator Micro-pump Micro-channel

PMMA	Injection molding Wire printing Laser ablation	E (Young's modulus) ~ 3.1 GPa Low vulnerability to moisture Optical transparency	Micro-channel Acceleration sensor Nano-structure arrays

SU-8 is rather an alternative material in particular for MEMS applications as compared to other polymers, therefore it is utilized as both structural and piezoresistive materials substituting semiconductors. Viscosity and processing time of SU-8 are two determinant factors, which classify SU-8 polymers are classified into different variants, according to viscosity and processing time, such as SU-8 2000, 100, and 50. For example, SU-8 2000 series polymers show better adhesion and coating, and faster processing time, which makes it widely used material in fabricating cantilever type piezoresistive sensors based on SU-8. SU-8 polymers enables for a structure with high-aspect-ratio, and also it makes possible to form mechanically stable structures. Moreover, SU-8 polymers are chemically inert and convenient to microfabrication techniques such as photolithographic process and etching. SU-8 is a photosensitive material, which has high refractive index in UV range, therefore it allows fabricating structures with sharp edges even for large thicknesses. This results in obtaining structures with high-aspect ratio (> 20) with UV lithography [322]. Besides, SU-8 has become a promising material due to its high refractive index. It is also biocompatible, and enables for adjustments upon its mechanical, optical, and electrical characteristics. SU-8 polymeric piezoresistive sensors can be composed of different piezoresistive material such as gold or doped polysilicon. SU-8 can be used as a piezoresistive element by doping as well.

The G/E ratio is determined by material characteristic, and is used to define the performance of piezoresistive cantilever sensors, which are detailed in Table 5. As it is shown that polymeric sensors based on SU-8 yields G/E ratio more than all the designs based on semiconductors (except the combination of SU-8 with Au piezoresistor). SU-8 polymer integrated with the doped polysilicon and the doped SU-8 show higher G/E ratio, which is due to the mechanical property of SU-8 providing Young's modulus that is lower than the other structural layers. Even though SU-8 polymeric cantilevers integrated with polysilicon by doping and CB-SU-8 piezoresistor provide high electrical sensitivity, graphene-based SU-8 cantilevers have ultra-sensitivity as it is depicted in Table 5, which is attributed to high gauge factor yielded by the graphene-nanoplatelet piezoresistive material [323].

Table 5. Several combinations of different structural layers with different piezoresistors and their corresponding gauge factors and G/E ratios [322-326].

Structural layer	Young's modulus (E) (GPa)	Piezoresistor	Gauge factor (G)	G/E
Si	169	Si	140	0.82
SiO_2	70	Si	140	2.0
	70	p-poly-Si	20	0.28
Si_3N_4	250	Au	2	8×10^{-3}
	250	p-poly-Si	20	8×10^{-2}
SU-8	5	Au	2	0.40
	5	p-poly-Si	20	4.0
	5	CB SU-8	20	4.0
	5	Graphene nano-platelet-SU-8	144	28.8

Over the last decade, SU-8 polymeric piezoresistive cantilever sensors have attracted enormous attention due to their applicability ranging from academic research to industrial applications. Therefore, researchers have discovered several possibilities to develop and optimize systems at material, fabrication, and device levels with high performance-to-cost ratio. In recent studies, materials and device optimization have been reported. For example, SU-8 based cantilevers were reported showing 19 times higher imaging in-air detection bandwith as compared to their typical counterparts, which show similarity in mechanical properties and dimensions. Besides, SU-8/ZnO nanocomposite nano-wires have been investigated for optimizing the performance of devices [327]. Furthermore, CB-doped SU-8 nanocomposites have shown good mechanical strength at low percolation threshold, and ability to be patterned by lithography process [286]. In addition, process parameter optimization has been released that baking temperatures and release methods were optimized to maximize fabrication yield [328]. Residual stress is emerged within the structure after baking process, therefore baking temperature affects mechanical behavior of SU-8-based sensors under deformation. In addition, wet release technique utilizing PMMA as a sacrificial layer has been reported, which resulted in obtaining high yield of 90% as compared to both dry method using fluorocarbon film as a sacrificial layer and wet etching method using omnicoat as a sacrificial layer.

SU-8 cantilevers have been demonstrated as the parts of the system. For example, SU-8 cantilevers have been shown vertically distributed in microchannels with enhanced performance [329]. Besides, SU-8 nanocomposite including silver nanoparticles have been depicted to establish electronic constituents and interconnect on flexible substrate

for sensing application [330]. Low-cost microfabrication techniques were used to fabricate compact-sized electronic elements and interconnects at high density, which make possible to fabricate complete polymeric devices consisting of SU-8 polymer and signal readout circuit. The reports for experiments have resulted that miniaturized devices were developed utilizing structural layer of SU-8 and low-cost fabrication process [331].

The improvements in designs and fabrication process have been also reported for optimizing the performance of cantilever sensors, which require structural optimization and material selection [332-335]. So, the electrical susceptibility of SU-8 piezoresistive sensor is originated from the Young's modulus and gauge factor of its piezoresistor. Besides, geometrical factors, and both intrinsic and extrinsic noises are characteristic factors determining the performance of piezoresistive micro-cantilever sensors based on SU-8.

2.1.3. SU-8 Piezoresistive Cantilever Sensors

SU-8 is an epoxy-based negative photoresist (PR), which includes SU-8 monomers comprising 8 epoxy groups, and each group forms the polymeric matrix, resin, organic solvent, and photoacid generator. SU-8 polymers are induced to experience polymerization reaction (cross-link) because of photoacid generation when they are exposed to light [336] or high-energy proton beam [337]. The polymerization reaction is only completed at raised temperatures, which is required to attain mechanical stability. SU-8 polymers have been utilized in numerous practices. For example, AFM cantilever [338], micro-needle [339], and micro-channel [340] are consisted of SU-8 polymers. SU-8 piezoresistive cantilever sensors are divided into two classes, which are homogeneous cantilever sensors based on SU-8 and hetero cantilever sensor based on SU-8. Hetero SU-8 cantilever sensor is classified based on piezoresistive materials such as doped poly-Si piezoresistor or metal piezoresistor as depicted in Fig. 18.

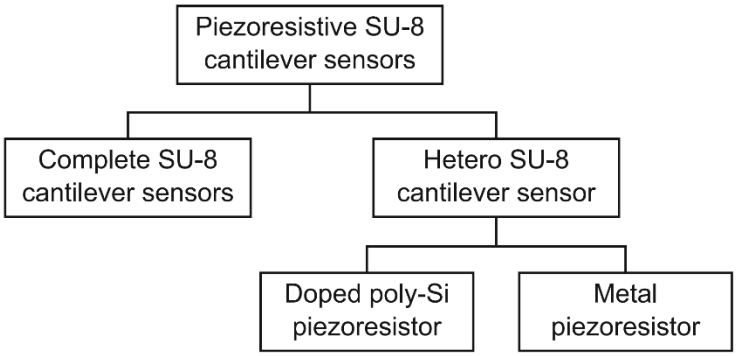

Figure 18. Variants of SU-8 piezoresistive cantilever sensors according to the component and piezoresistive materials of the structure

The sensors with various cantilever geometry, constituent layers, and piezoresistive materials have been reported. The cantilever geometry has been in the different forms such as square, V shape with slit-, rectangular-, and U-shaped. SU-8 polymers have been used to construct various constituent layers like piezoresistive, structural, and isolation layers.

Thickness and lateral dimension are two factors, which determine the mechanical stability of the sensors. Sensor die size and piezoresistor coverage area are two important determinant factors, which affect the design of the lateral dimensions of the cantilever. In order to provide mechanical endurance for the cantilever structure the thickness of the SU-8 cantilever is mainly maintained higher than 1 μm. Besides, the electrical sensitivity is maximized when the distance between the neutral axis of the cantilever stack and the mid-plane of piezoresistor is at maximum. The geometry of piezoresistive layer is designed according to SNR and nominal resistance value at desired level. Typical nominal resistance value of a piezoresistor is maintained around in kΩ range. U-shaped design is a type of geometry commonly used in piezoresistors, which results in enhancing trustworthiness by eliminating interconnections on the stand of the cantilever. The fact that the nominal resistance of U-shaped metal piezoresistors is a few of ohms, they are designed longer to gain higher nominal resistance. Therefore, instead of using the typical U-shaped design piezoresistive layers, the serpentine-shaped piezoresistors are preferred. However, cantilever lateral dimensions restrict the area covered by the piezoresistive layer because longer the cantilever platforms lower the mechanical stability and electrical sensitivity. Likewise, the thickness and width of the piezoresistive layer are two defined

factors in terms of obtaining a nominal resistance at desired level. Thickness of metal piezoresistive layer is inversely proportional to electrical noise level. Therefore, thicker metal piezoresistors yield lower electrical noise.

2.1.3.1. Cantilevers with Metal Piezoresistors

In 2002, Thaysen et al. were the first to report the integration of metal piezoresistive material (Au) with polymeric structural layer (SU-8) [341]. Whereas semiconductor piezoresistors show changes in electrical resistivity as a result of deformation of energy bands, geometrical variations in metal piezoresistive layers induces resistance change, which is called strain-induced resistance change. Throughout the years, various metals and their alloys ranging from titanium to copper-nickel constantan alloy have been studied for strain sensing applications [238, 240, 342-345]

A piezoresistive layer made out of metal is placed on top of SU-8 structural layer in metal piezoresistive-based cantilever sensors. In some cases, SU-8 is coated and used as a dielectric layer on top of metal piezoresistive layer, which avoids contact through the metal piezoresistors with environment. Au- and Ti metal piezoresistors with SU-8 structural layer are better combinations in terms of demonstrating higher sensitivity meaning higher G/E value as compared to the metal or poly-Si piezoresistive layers integrated cantilevers with other material. In Fig.19**,** Ti-based SU-8 cantilever sensor in U-shaped design is picturized where a Wheatstone bridge (WSB) circuit is connected to two microcantilever sensors with integrated piezoresistors [346].

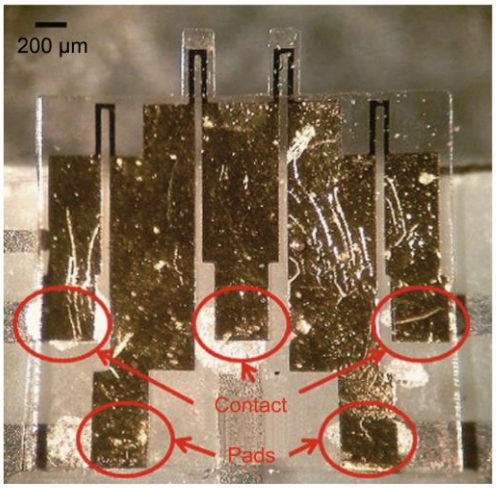

Figure 19. WSB configuration with Ti/SU-8 cantilever sensors [346].

SU-8 cantilevers with metal-based piezoresistive materials are considered as an alternative approach to cantilevers with semiconductor-based piezoresistive materials. However, metal piezoresistors are attenuated in sensing applications due to some limitations. The fact that metals are highly conductive materials leading to substantial amount of Joule heating when an external voltage is applied by a dc source, the nominal resistance value of metal piezoresistors cannot be maximized after a certain point, which is opposed to the concept of cantilevers that are designed to obtain high value of nominal resistance through piezoresistors. In addition to Joule heating in the metal piezoresistors, lower conductance of polymeric matrix of SU-8 is another hindrance resulting not only in changes of TCE-induced cantilever deflection, but also causes to rise the value of Johnson noise floor. The polymeric material of the cantilever suffers the plastic deformation as well. The length of piezoresistor can be increased to obtain higher nominal resistance value, nonetheless the electrical sensitivity of the device is negatively affected. Besides, serpentine-shaped metal piezoresistors and applying dc voltage at low level increase the nominal resistance value of the piezoresistor. On top of above-mentioned factors, adhesive materials are used to stabilize the sensors on any surface in some cases, which cause device failure. However, the sensor reported titanium metal piezoresistor without any adhesive layer [346]. Apart from that, electro-migration effect is strongly associated to the high magnitude of current density leads to instability of resistance.

2.1.3.1.1. Polysilicon Piezoresistor-Based Cantilevers

Cantilevers with polysilicon is alternative to metal piezoresistor-based cantilevers, where polysilicon in thin film form is utilized as the piezoresistive material in SU-8 cantilever sensors. Even though doped polysilicon piezoresistive material integrated with SU-8 structural layer has shown higher G/E value than those of metal-based piezoresistors, use of doped polysilicon is restricted in sensors due to the subsequent reasons. First, SU-8 is vulnerable to deposition processes requiring high-temperature such as plasma enhanced chemical vapor deposition (PECVD) and low-pressure chemical vapor deposition (LPCVD). Second, electrical sensitivity is reduced due to the fact that doped polysilicon has high stiffness, which makes it brittle, theferore it cannot withstand large cyclic strains. On the other hand, it has been reported that sensors that are dimensionally optimized and designed carefully can overcome the limitations caused by cantilever stiffness [347].

Electrical properties of polysilicon are defined with its grain size, concentration, doping type, and crystal orientation [247]. Besides, the electrical properties of polysilicon can be manipulated by changes in impurity concentration and process parameters [348, 349].

The fact that polysilicon piezoresistor have relatively higher Young's modulus than SU-8 polymer, the SU-8 cantilevers with doped polysilicon piezoresistors show low performance due to the increase in stiffness of composite cantilever structure [347]. Although, it causes increasing the electrical noise, reducing the thickness of the piezoresistor is a possible solution. Fig. 20 shows optic imageries of the cantilevers based on SU-8 integrated with the U-shape polysilicon piezoresistor [350].

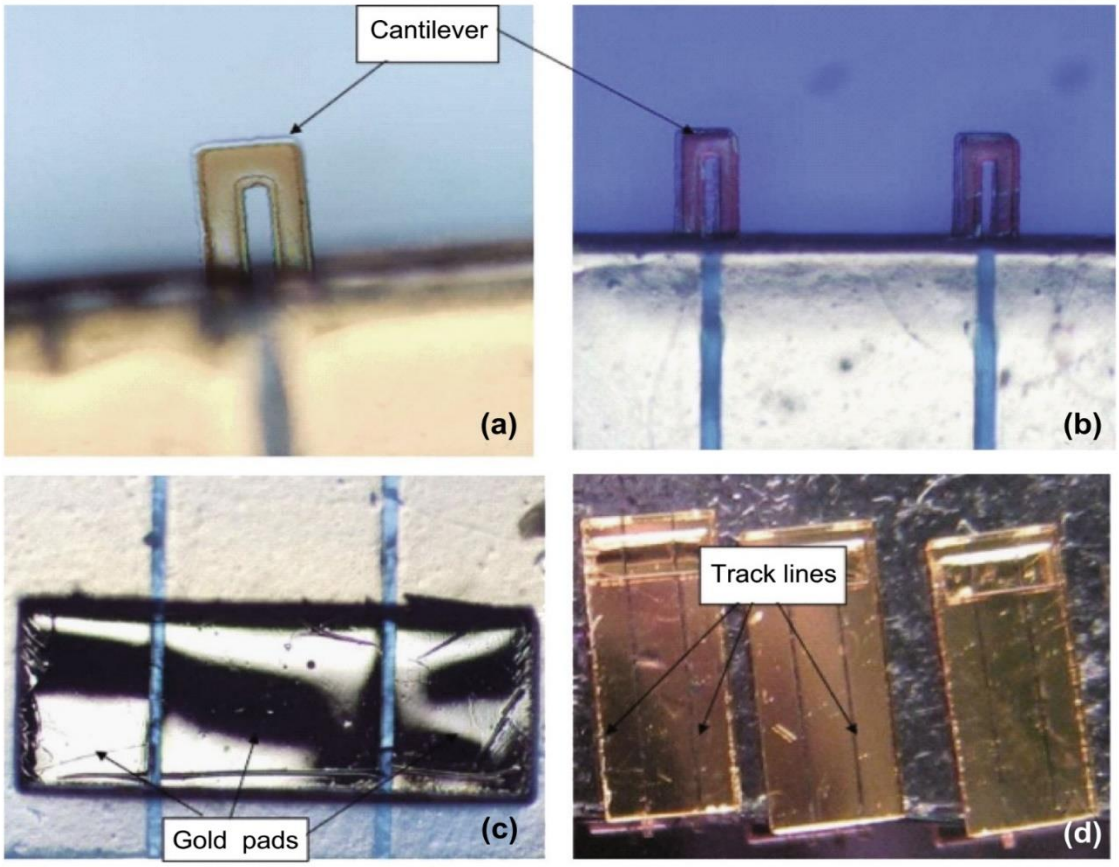

Figure 20. (a) Optic imageries of the cantilevers based on SU-8 integrated with the U-shape polysilicon piezoresistor; (b) two cantilever sensors in U-shape configuration; (c) track lines and gold pads; (d) complete die [230].

2.1.3.1.2. Complete SU-8 Polymeric Cantilevers

Homogeneous polymeric cantilevers based on SU-8, as stated in their names, are constituted of SU-8 polymeric materials, where both structural layers and piezoresistive materials are made up of SU-8. Conductive fillers in form of nanoparticles are added into SU-8 polymer, hence making the polymer conductive. There are a few of conductive filler examples that are physically spread into the polymer matrix to form conductive polymers ranging from carbon black (CB) to gold nanoparticles [341-344, 351]. The dispersion and density of conductive nanoparticles along the polymeric matrix describe the electrical conductivity of polymers. Electron tunneling effect among the nanoparticles through the polymer film boundary creates the mechanism of electrical conduction [255].

Complete SU-8 polymeric cantilevers give higher G/E values than hetero-SU-8 polymeric cantilevers that combine metal/polysilicon piezoresistors with SU-8 polymer. The number of conductive nanoparticles, and their alignment and dispersion in the polymeric matrix govern the conductivity of composite SU-8 structure. Besides, percolation threshold limit is one of the defined parameters for conductivity. When a cantilever is deflected, the conductive pathways consisted of dispersed nanoparticles in the polymeric mould is broken, which resulted in changing the behavior of SU-8 piezoresistor doped with CB in terms of conductivity. Fig. 21 shows the optical image of doped SU-8 with CB piezoresistive sensor array. The higher sensitivity (G/E around 4) is reached as a result of the low Young's modulus of SU-8 and high gauge factor of CB-doped SU-8 [352].

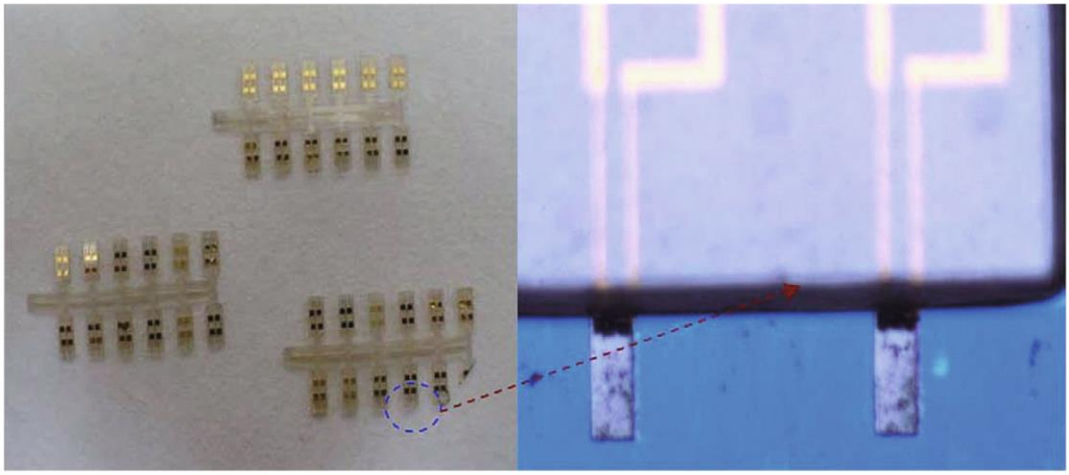

Figure 21. Optical images of doped SU-8 with CB piezoresistor cantilever sensor arrays with a zoom-in image of a pair of cantilevers [322].

3. BACKGROUND OF BASIC MICROFABRICATION TECHNIQUES

With the advent of micro/nanofabrication techniques, structures in the nm-mm range have been able to manufacture. Six orders of magnitude in dimension are available to fabricate innovative devices such as optical, mechanical, electronic, and chemical/biological based sensors.

In this chapter, the most important and commonly used microfabrication techniques are overviewed, which include the most basic methods utilized in the integrated circuitry (IC) industry, such as lithography, thin-film deposition, and etching and substrate removal.

3.1. Lithography

Lithography is the technique where the computer-designed pattern is transferred onto a substrate like silicon, glass, and GaAs. After that, an underlying thin film of this pattern, either oxide or nitride, is used as a substrate layer, and is etched for various purposes like doping and etching. Despite the fact that photolithography is the most commonly used lithography technique that uses an ultraviolet (UV) light source in the microelectronic fabrication, electron-beam (e-beam) and x-ray lithography have been considered as two promising alternatives in the MEMS and nanofabrication fields.

The generation of photomask is the initial point of a specific fabrication sequence, which constitutes a series of photographic processes using optical or e-beam pattern generators. This results in obtaining the desired pattern in the form of a thin chromium layer atop a glass plate. The following lithography processes are sequenced in Fig. 22. Afterwards, a thin film is deposited onto a silicon substrate, then a photoresist is spun onto the wafer.

Photoresists are polymeric materials, and they are sensitive to UV-light. Two types of photoresists exist: positive and negative. When positive photoresist is exposed to UV-light, the exposed areas will be dissolved in the development step. On the other hand, the exposed areas with negative photoresist will remain intact after developing. Following the spinning of the photoresist onto the wafer, the substrate is soft-baked in order to evaporate solvents existing in the photoresist, thus improving adhesion. Then, the mask is brough into alignment with wafer, and exposure of photoresist to UV-light is the next step.

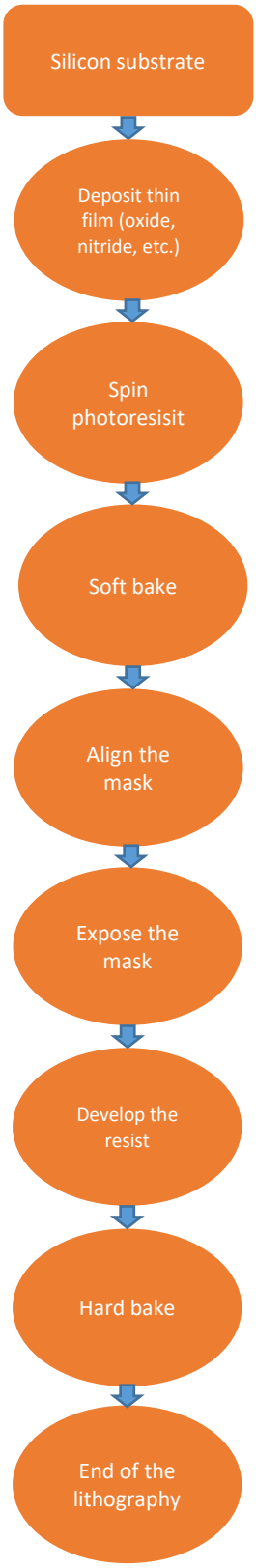

Figure 22. Process flow of lithography

Exposure systems are differentiated based on the difference in the mask and wafer, which are classified into three types: contact printing, proximity printing, and projection

printing. Even though contact printing provides better resolution in comparison to the proximity method, the mask contacts with PR resulting in damaging the mask and reducing the process yield. In projection printing system, a dual-lens optical system is used to project the mask image onto the wafer. The fact that only one die can be exposed at each time, whole wafer area is required to expose with a step-and-repeat system. Projection printing promises the higher resolution than the contact and proximity equals, therefore it is mostly preffered lithography technique in the microfabrication process. The resolution is governed by the exposure source of photolithography. A high-pressure mercury lamp is used for minimum line width above 25 μm. On the other hand, deep-UV sources such as excimer lasers are required for line width between 0.25 and 0.13 μm, and extreme UV (EUV) is chosen for line width below 0.13 μm.

Subsequent the exposure, the photoresist is developed, then it is hard-baked in order to enhance bonding more onto the surface. The photolithography process flow is concluded with the hard-bake step, thus forming the designed pattern on the wafer. After that, the thin film underneath of the photoresist is etched, and the photoresist is removed using acetone and isopropyl alcohol, respectively.

3.2. Thin-Film Deposition

Thin-film deposition technique is mostly utilized in micro/nanofabrication technologies, which allows producing main constituents of micro/nanostructures by using several deposition techniques. These techniques are utilized in a few typical applications ranging from mask for etching to mechanical structure.

The properties of the deposited thin films show dissimilarities to their bulk forms counterparts. For example, metals have lower resistivities in bulk forms than those of their corresponding thin-film forms. Furthermore, the techniques used to deposit these materials lead to some changes in their ultimate characteristics. For instance, internal stress can occur through the thin film due to deposition techniques. So, when excess amount of stress is applied, film will be cracked or detached from the substrate, therefore it must be minimized. Moreover, adhesion is improved by depositing noble metals like

gold or titanium in some cases, and chromium or titanium is also deposited into the midplane as an adhesion layer. Lastly, step coverage and conformality need to be taken into account due to their impacts on deposition techniques.

3.2.1. Chemical Vapor Deposition

Chemical vapor deposition (CVD) covers all the deposition techniques that form the deposited thin film by reacting chemicals in gas phase. The substrate is maintained at elevated temperature; therefore, the required energy is supplied in order to initiate chemical reaction. However, optical or plasma excitation enables for maintaining the substrate at low temperature, therefore they are considered as alternative energy sources. Among the deposition techniques, plasma-enhanced CVD is mostly used in microfabrication.

In the PECVD process, radiofrequency (RF) energy is used to create the plasma with very reactive particles, which enables to perform the reaction at lower temperature level at the substrate (150-350 ^{o}C). Parallel-plate reactors are utilized in microfabrication, therefore a number of wafers per batch is limited to process. The fact that the wafers are located horizontally at the top side of the lower electrode, only single lateral of the wafer is deposited. Silicon oxide, silicon nitride, and amorphous silicon are typical materials deposited by PECVD process. Fig. 23 shows the schematic diagram of typical PECVD system [353].

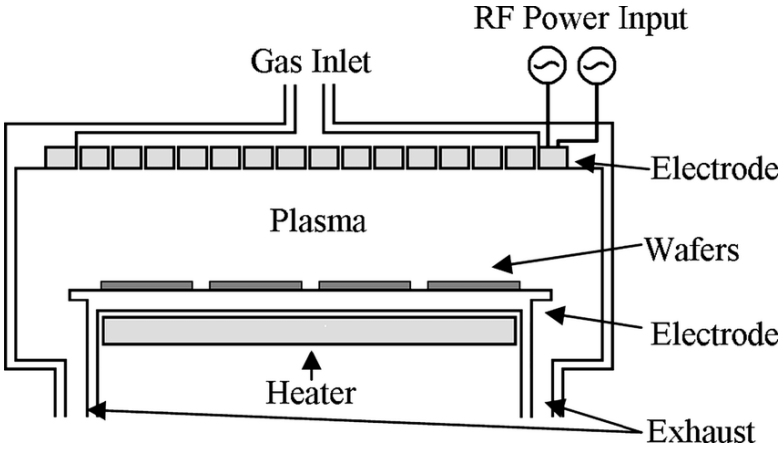

Figure 23. Schematic of PECVD system [364].

3.2.2. Physical Vapor Deposition

In physical vapor deposition systems, the material transferring occurs in the same chamber where a source into the crucible is positioned right across to a wafer meaning that one is at the top and the other is at the bottom side of the same chamber. The transferring the material is based on two physical principles: evaporation and sputtering. Physical principle of evaporation includes that the source placed into a small container, named the crucible, is heated up to a specific temperature where the source is started evaporating. Several techniques are utilized in order to heat up the source such as coils twisted around crucible inducing high currents and use of an electron beam (e-beam) for bombarding the material surface. In this way, metals are deposited. In the vacuum chamber of the system, the crucible is positioned at the bottom side of a vacuum chamber while the wafers are placed face down to the crucible at the top side of the chamber. It may be noted that very poor step coverage such as shadow effect is experienced in evaporated films at the end of this process. However, the wafers are rotated and/or heated in order to enhance the step coverage during deposition. Evaporation system allows depositing more than one material simultaneously or consecutively, which enables to gain films in alloys and multilayer forms. For example, Au and Pt are low-reactivity metals, therefore a thin layer of another metal such as Ti or Cr, frequently used adhesion promoter, is previously deposited in order to increase adhesion. The system shows better

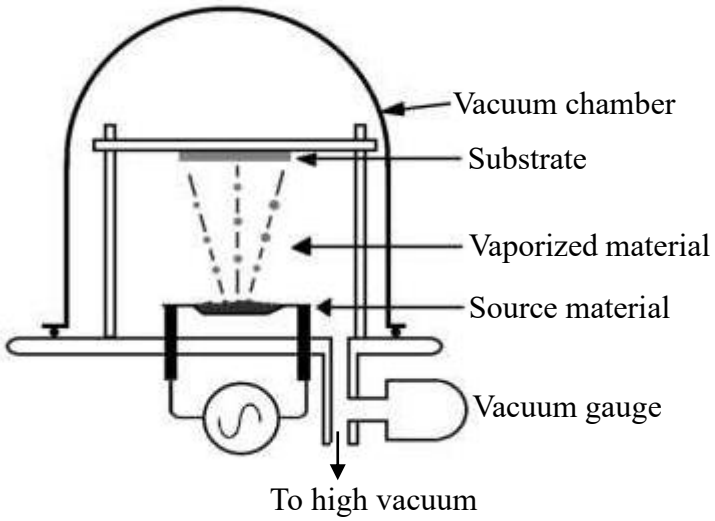

Figure 24. Schematic representation of PVD system [355].

performance in terms of the deposition rates among CVD techniques. Fig. 24 shows the schematic representation of PVD system [354].

3.2.3. Metal Etching and Substrate Removing

Thin-film and bulk substrate etching are important parts of micro/nanofabrication processes. Several dielectric and conducting thin films are deposited in purpose of passivation or masking, which need to be removed eventually. In micro/nanofabrication, thin-film is not only etched, but the substrate composed of silicon, glass, GaAs, etc. also needs to be detached in order to obtain numerous mechanical micro/nanostructures such as beams and plates. Selectivity and directionality are functions of the etching process. Selectivity is defined by the degree of the etchant that can distinguish between the masking layer and the layer to be etched. Directionality is described with the etch profile under the mask. When the etchant performs in all directions at the same rate with regards to etching the material, it is called an isotropic etch. Therefore, a semicircular profile is created under the mask. On the other hand, an anisotropic etch performs based-on the dissolution rate on specific directions, therefore straight side-walls or other noncircular profiles can be obtained.

In this chapter, etching techniques are classified into wet and dry etching categories. First, wet etching is elaborated with various wet etchants. Then, dry etching techniques used mostly in the micro/nanofabrication are discussed.

3.2.3.1. Wet Etching

Wet etchants are better at select the masking layer in comparison to several dry techniques, and their characteristics are also typically isotropic. Besides, the minimum feature size limited to 3 μm is enabled to reach with wet etchants due to the horizontal undercut. Moreover, typical wet etchants are utilized to remove a few substrate layers and masking layers as mentioned in the previous section. For example, silicon dioxide is etched by dilute or buffered HF solutions. In addition to the etching silicon dioxide, silicon nitride and photoresist are considered as two most common masking materials to be etched by wet etchants. On the other hand, metals are etched by several mixtures of acid and base solutions. Commercially available etchant formulations are also available for etching aluminum, chromium, and gold.

With the discovery of wet etching of crystalline (silicon and gallium arsenide) and noncrystalline (glass) substrates in anisotropic and isotropic profile, micromachining and MEMS discipline have been recognized. Various combinations of solutions dating back to 1950s are currently used to make the silicon wafer thin isotropically. Glass is also isotropically etched by using the chemical combination of HF and HNO_3, which is utilized to obtain microfluidic components such as microchannels.

In anisotropic wet etching, silicon dioxide and nitride are used as common masking materials. Crystallographic plane of (111) represents the slowest etch rate. Even though the lower atomic concentration throughout these planes has been claimed as the reason for this circumstance, the evidence needs to be concluded, and other factors must be taken into account for this notable etch-stop characteristic. Due to the anisotropic characteristic of the etchants in (111) planes, mechanical and structural components including beams and membranes have been able to fabricate.

3.2.3.2. Dry Etching

Dry etching techniques are mostly plasma-assisted, which provide some advantages in comparison to etching in wet form. For example, smaller lines are allowed to pattern (smaller undercut), and to form high-aspect-ratio vertical structures (higher anisotropy). Etching techniques in dry form show inferior in terms of selectivity to wet etchants; therefore, masking materials must be taken into account with their finite etch rate. RIE is one of the most common dry etching techniques combining physical etching with chemical reactions. Therefore, it is also named as ion-assisted etching. In the reaction, the top layers are stimulated by the collisions of ions from the plasma, then those incident ions break the bonds at the surface, therefore the reaction between the material and the reactive species is initiated. Due to the direction of the ion’s velocity, a higher number of collisions occurs on the flat side than on the vertical side. Therefore, higher etching rates are achieved vertically.

4. DESIGN AND FABRICATION OF A GRAPHENE BASED SU-8 PIEZORESISTIVE STRAIN SENSOR

4.1. Design of Microcantilever

The dimensions of the strain gauge have been determined prior to the fabrication. The dimensions for the designed microcantilever is listed in Table 6. Fig. 25 shows the image of the microcantilever sensor schematically with its 3 mm width, 6.1 mm length, and 0.05 mm thickness. The ratio of the total length of the cantilever to the length of the designed piezoresistor is 10, *i.e. 600 microns*.

Table 6. The dimensions of the designed piezoresistive strain gauges

Parameter	Value	Unit
Cantilever length	6.1	mm
Cantilever width	3.0	mm
Cantilever thickness	0.05	mm
Graphene/Au piezoresistor arm length	2.4	mm
Graphene piezoresistor arm length	2.4	mm
Graphene/Au piezoresistor width	0.65	mm
Graphene piezoresistor width	0.65	mm

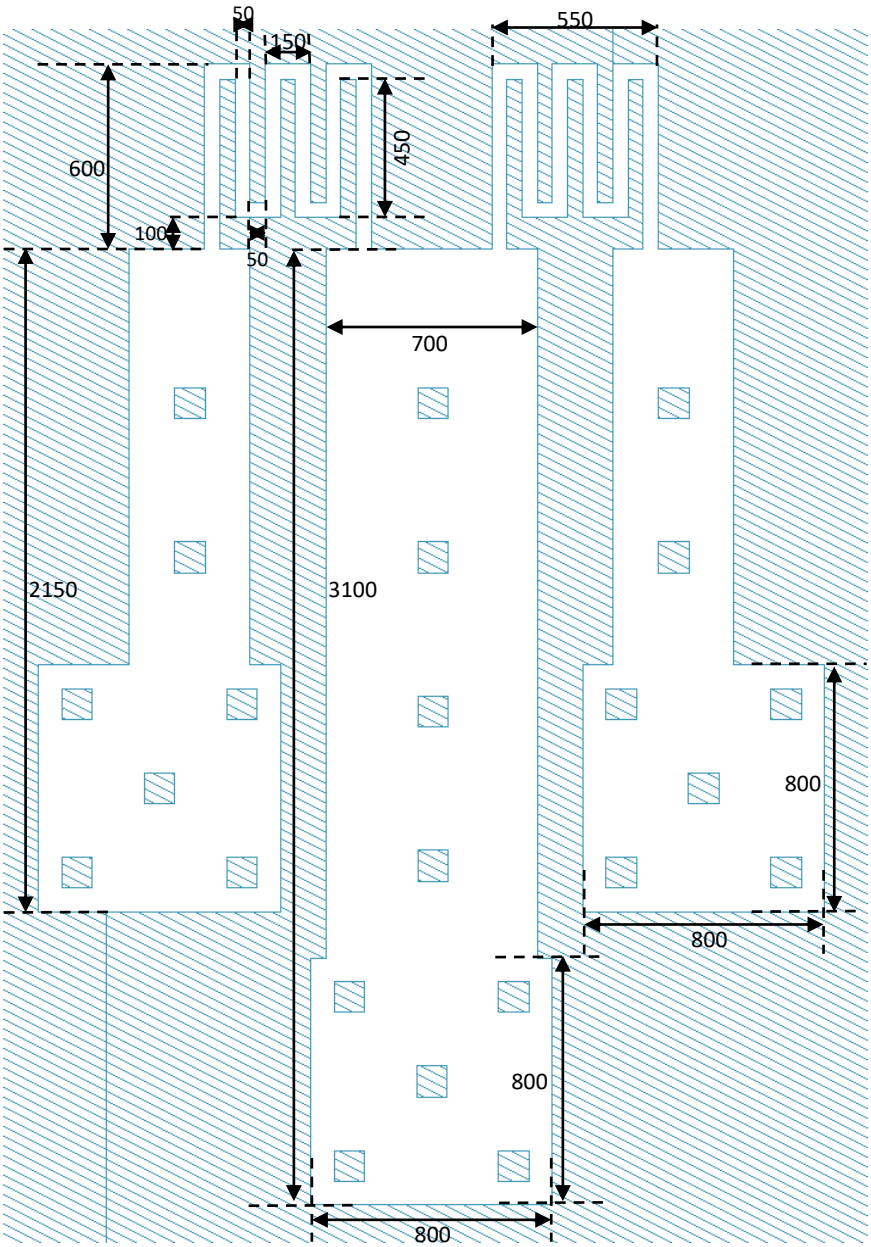

Figure 25. Design of the microcantilever sensor defining the dimensions of the strain gauge shown in the schematic

Fig. 26 shows the optical image of the piezoresistive strain gauges composed of thin and narrow SU-8 beams with gold pads, where gold/graphene and graphene zig-zag shaped piezoresistors are placed in the arms of the microcantilevers.

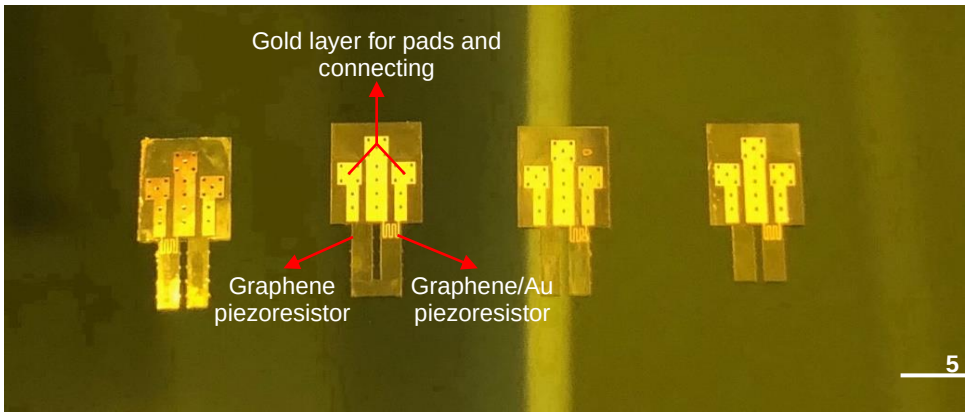

Figure 26. Optical image of an array of SU-8 piezoresistive strain gauges.

The choice of metal as a strain sensor is gold due to its good resistivity and large Poisson's ratio, which also defines a large piezometallic coefficient. On the other hand, the choice of semiconductor as a strain sensor is graphene not only because of its excellent mechanical and electrical properties but also due to having linear change of resistance versus strain, making it a good candidate for piezoresistive sensor applications.

The structural layer of the microcantilever type strain sensor is comprised of SU-8 since it enables to be patterned via optical lithography. Besides, SU-8 promises an ideal value of Young's modulus for the designed applications. It also shows insulating capability and high dielectric strength even for very thin layers.

Following the drawing of the computer layout, a photomask is created in order to design the microcantilever, which consists of sequential photographic processes utilizing optical generators. Therefore, a plate made of glass with the designed pattern is obtained as a thin chromium layer (around 100 nm). The lithography process subsequent to the generation of the photomask proceeds with next step as defined in Fig. 22.

4.2. Fabrication

The overall fabrication process is composed of nine steps, which are detailed in Fig. 27.

Based on the proposed method, three masks were used to fabricate the SU-8-based microcantilever with integrated piezoresistive readout. Fig. 28 shows the cross-sectional device fabrication flow, which defines our approach for patterning graphene and gold piezoresistors by combining the soft-lithography, wet etching, and oxygen plasma etching.

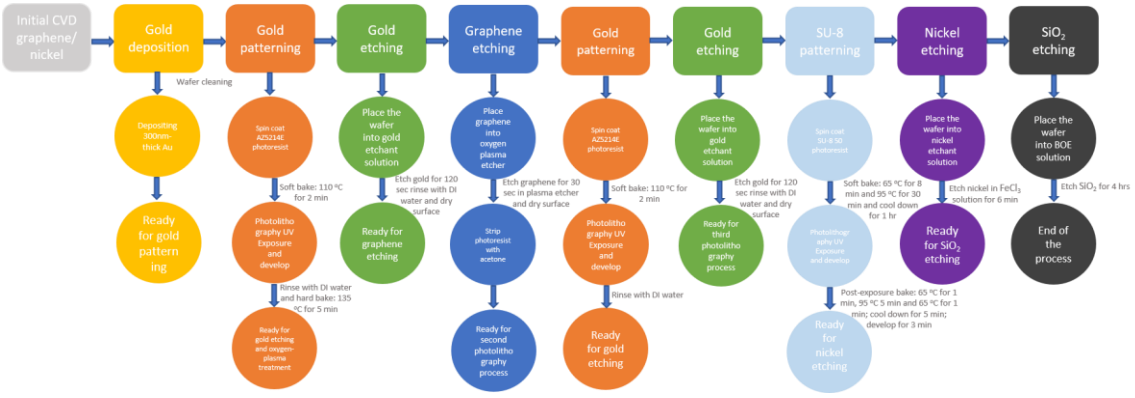

Figure 27. Overall fabrication process flow.

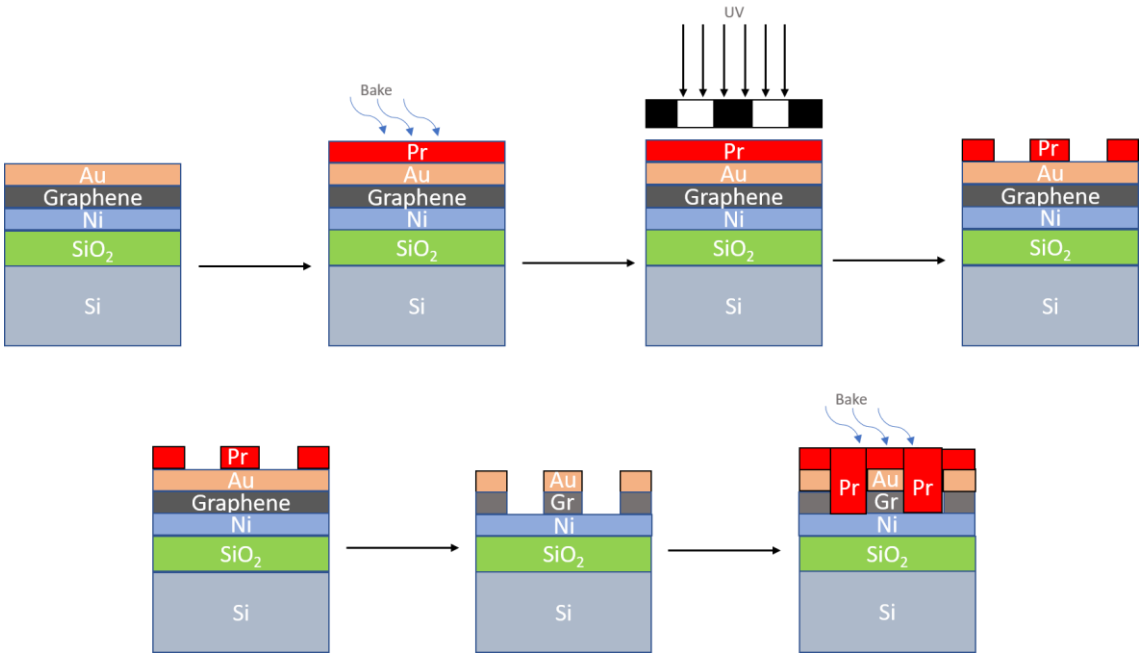

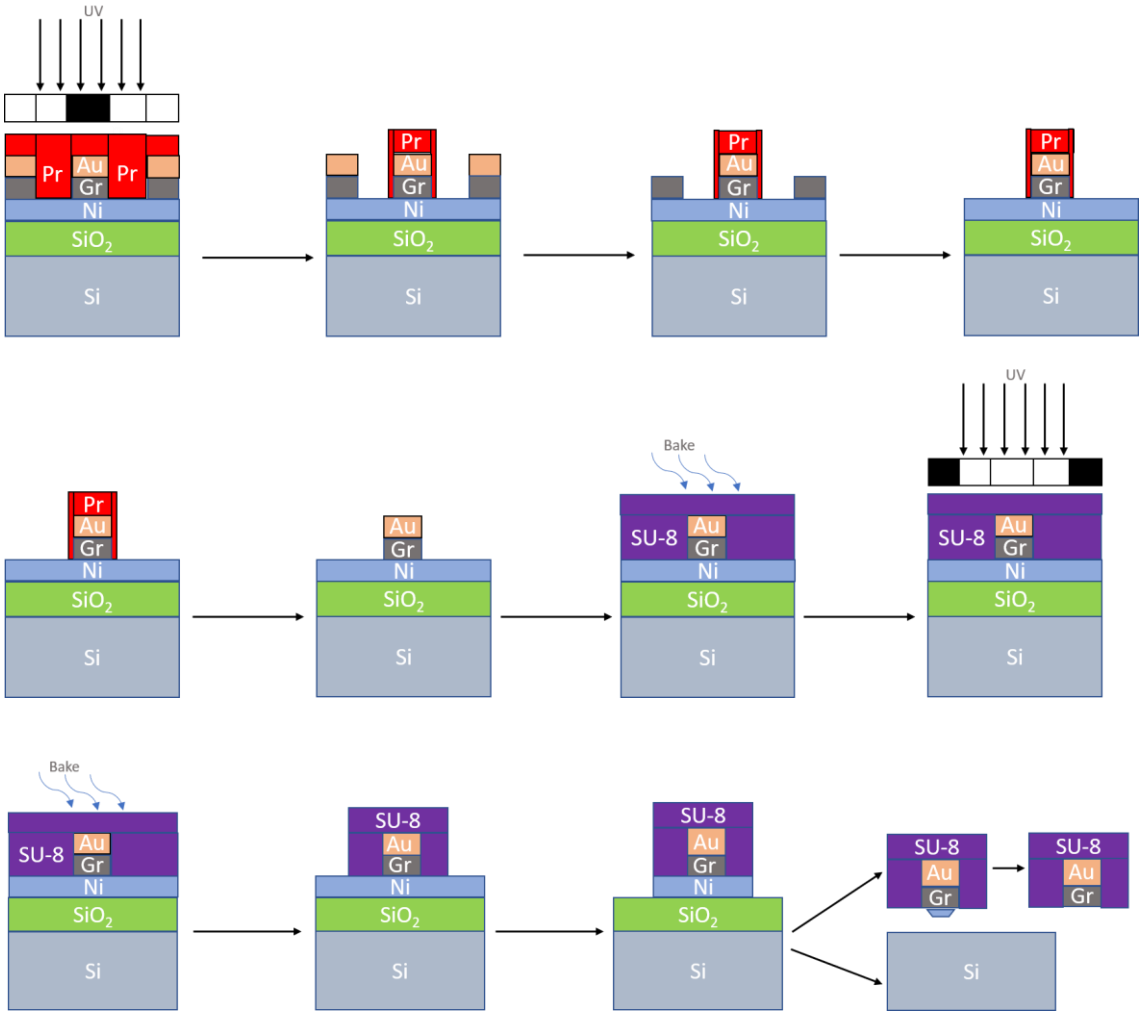

Figure 28. Process flow diagram outlining the device fabrication.

First, a layer of 300 nm thick-gold is deposited on the Si / SiO_2 / Ni / Gr (Graphene Supermarket, Inc.). The gold film was deposited by using electron-beam evaporator. The gold layer has been used not only as a metal pad and a piezoresistive layer but it has been also utilized for connecting the graphene as a piezoresistive layer to the metal pad. A thin layer of AZ 5214 positive photoresist was spun on the substrate at a spin rate of 4000 rpm for 30 s, which resulted in a final thickness of around 1.4 μm-thick photoresist layer. The layer was soft baked (110 ^{o}C for 2 min) and patterned with the first mask under UV light (130 mW/cm^2). After the exposure, a development was conducted to dissolve the photoresist layer at the region where UV light was exposed. This coating was used to isolate the layers of beam shape consisting of Au / Gr / Ni / SiO_2 / Si prior to proceeding to the metal etching step. Next, the photoresist layer was hard baked in a conventional oven to increase its stickiness by evaporating the solvent inside PR, thereby becoming

more resistant against to Gold Etchant solution (Sigma-Aldrich), and later the solution was used to etch the Au layer for 120 sec. Thereafter, the surface has been treated with O_2 plasma to etch graphene layers for 30 sec at a power of 50 W, a pressure of 40 mTorr, an oxygen flow of 40 sccm, and 26 ^oC, then the substrate has been cleaned immersing in acetone, isopropyl alcohol (IPA), de-ionized (DI) water sequentially and blown dry with N_2 gas. In the next step, the second mask has been used to pattern the second (intermediate) layer of microcantilever beam where Au and Au / Gr piezoresistors have presented in the arms. The same procedures have been conducted as the first mask; however, one step was distinguished from the whole where the Au layer was etched only in one arm, which resulted in having the Au and the Au / Gr layers in two arms of the beam, separately. Afterwards, SU-8 negative photoresist was spun on the substrate. The spin coating parameters were determined according to the desired thickness of SU-8; therefore, the first spin rate was initiated from 0 to 500 rpm for 3 sec, then the spin rate was kept at 500 rpm for 10 sec. Next, the spin rate was accelerated to 2000 rpm in 10 sec, later it was continued to spin at 2000 rpm for 30 sec. Lastly, the spin rate was decelerated to 0 rpm in 10 sec, and the substrate was placed on a flat surface for reflowing the resist on the surface for 1 hour, thereby smooth and conformal coating on the substrate. Eventually, a final thickness of around 50 μm-thick SU-8 negative resist was expected. The layer was soft baked (65 and 95 ^oC for 8 and 30 min, respectively), and cooled down for 1 hour, and patterned with the third mask under UV light (120 mW/cm^2) in soft contact mode to finalize shaping the upper cantilever layer. After the exposure, the layer was post exposure baked (65, 95 and 65^oC for 1, 5, and 1 min, respectively) and cooled down for 5 min before moving onto a developing bath. Then, a development (3 min) was conducted to dissolve the photoresist layer at the region where UV light wasn't exposed. This resulted in obtaining a cantilever beam made up of SU-8 negative resist on Si / SiO_2 / Ni substrate (figure 29). Fig. 30 shows all the formed SU-8 strain gauges, which were inspected under an SEM (scanning electron microscope). The optical images of the patterned SU-8 strain gauges are shown in Fig. 31. Lastly, the SU-8 microcantilevers were released from the substrate immersing in $FeCl_3$ solution (Sigma-Aldrich) for 6 min to etch Ni layer, then placed into BOE solution in order to etch SiO_2 for 4 hours.

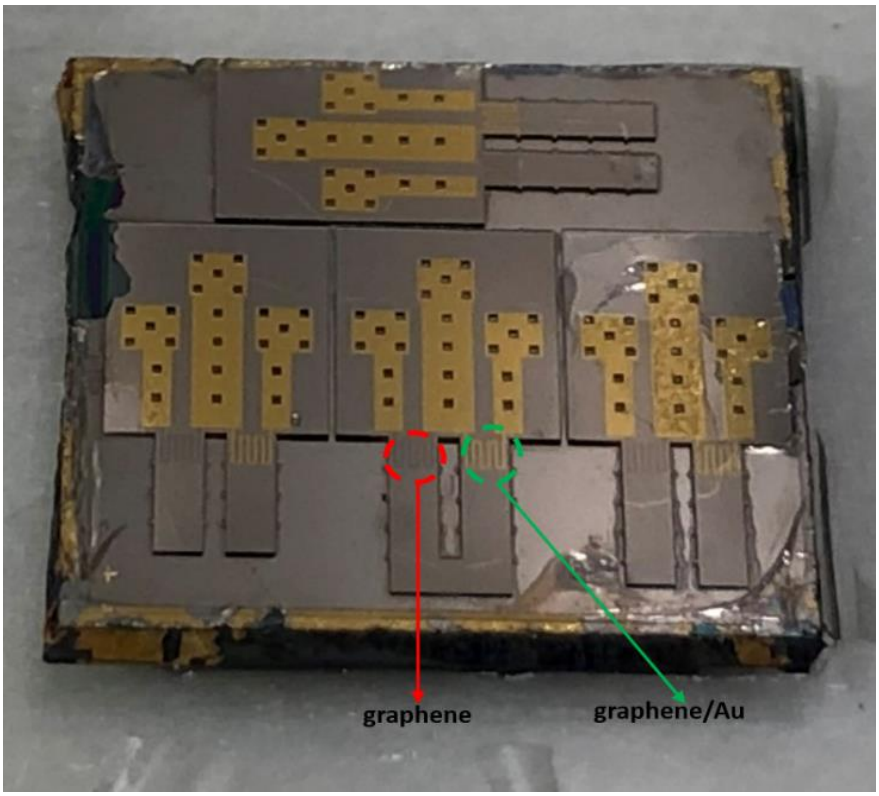

Figure 30. Optical image of fabricated SU-8 strain gauges on an SOI substrate.

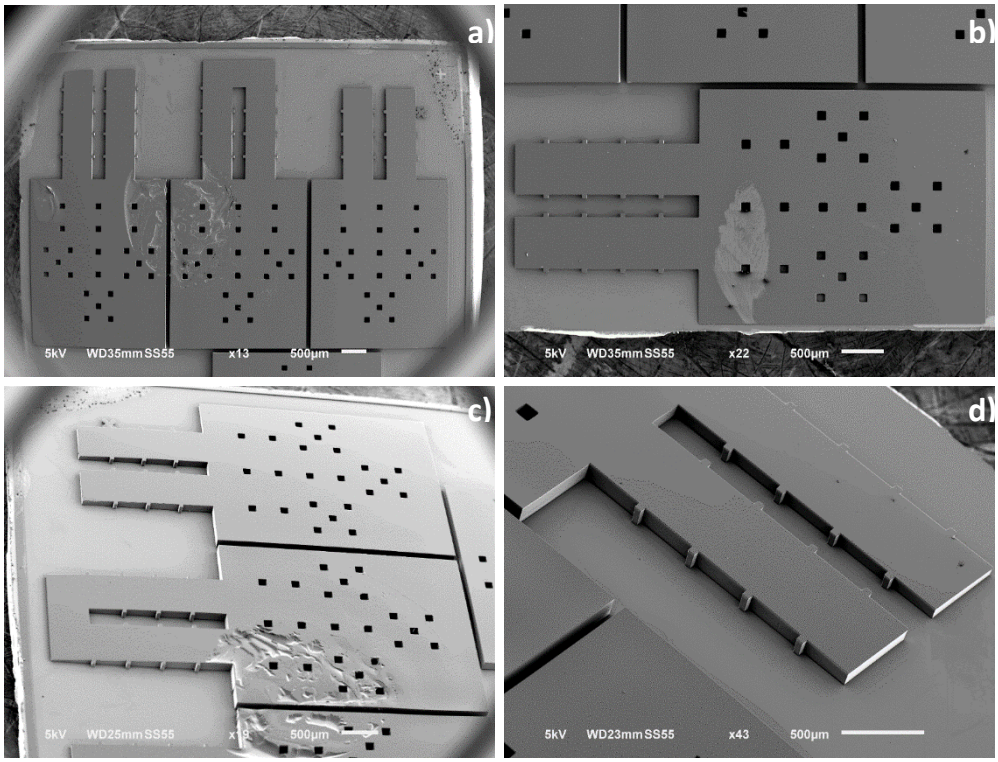

Figure 29. Scanning electron micrograph of fabricated SU-8 strain gauges on an SOI substrate. Inset (a)-(d) show the SU-8 body of strain gauges from different point of view.

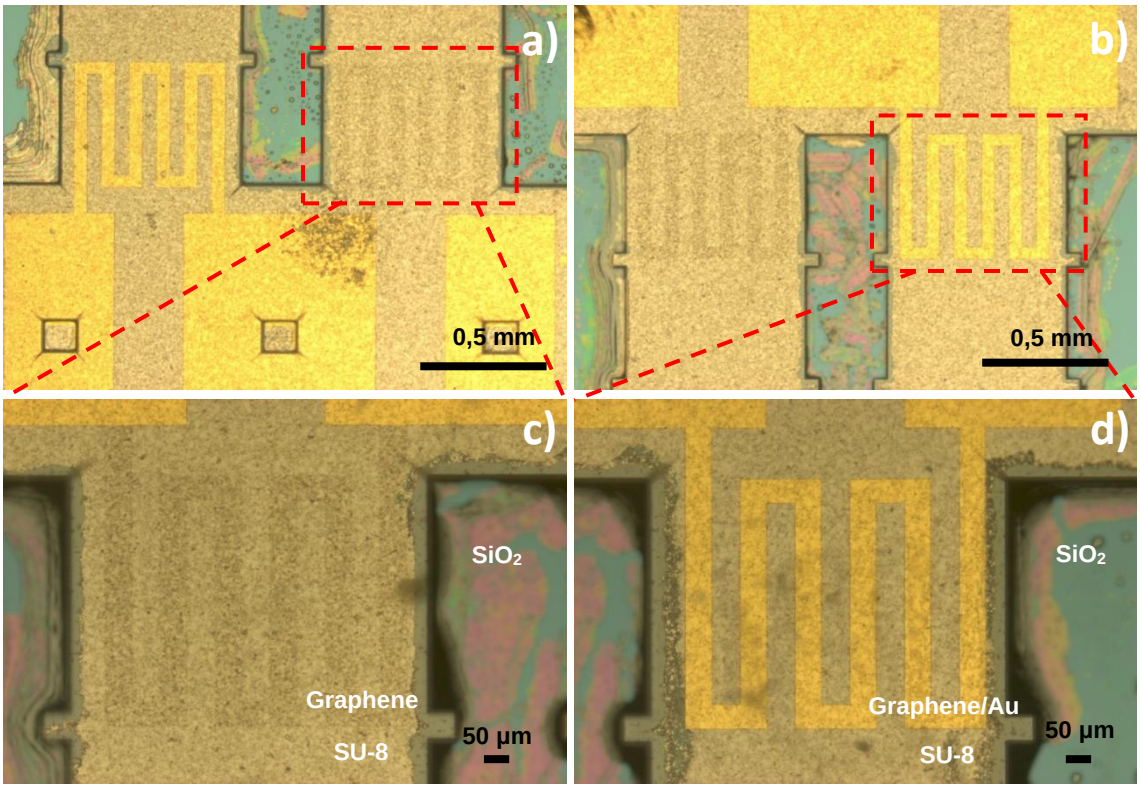

Figure 31. Optical images of SU-8 strain gauges on an SOI substrate at the end of patterning processes. Inset (a), (b) show the patterned SU-8 strain gauges with graphene/Au and graphene serpentine-shaped piezoresistors on the arms. Inset (c), (d) provides zoom-in images of both graphene and graphene/Au serpentine-shaped peizoresistors on the arms, respectively.

The structural characteristics of the graphene were examined via Raman spectrum in Fig. 32, where three most prominent peaks are displayed: The G band at 1581 cm^{-1}, the 2D band at 2720 cm^{-1}, and the disorder-induced D band at 1238 cm^{-1}. The G band, which is considered as the most prominent characteristic of most graphitic materials, is caused by in-plane vibrations of sp^2 carbon atoms. Whereas the 2D band becomes the foremost feature for graphene as compared to that of bulk graphite. The graphene lattice has some defects represented by the D band; however, it is not usually observed in highly ordered graphene layers. The intensity ratio of the G band to D band allows characterizing the defects in a graphene sample. On the other hand, the intensity ratio of 2D peak to G peak gives the number of graphene layers.

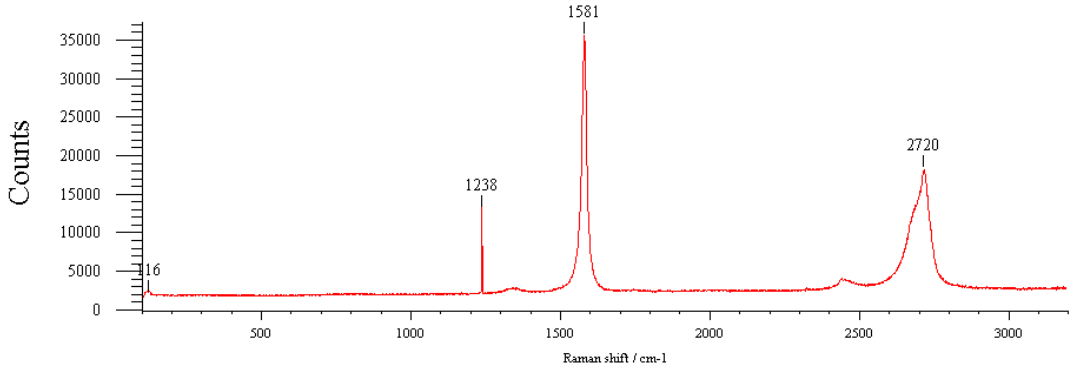

Figure 32. Raman spectra for the graphene serpentine-shaped piezoresistor.

5. EXPERIMENTAL CHARACTERIZATION

5.1. Microcantilever Testing

The experimental setup was used to measure the resistance change of the strain gauge as a function of the microcantilever deflection. There have been two test rigs constructed for the measurements. The first setup consisted of some components of which are an adjustable needle/probe to move the free tip of the strain gauge down, three degrees-of-freedom positioners (*x*, *y*, and *z* directions) for the needle/probe operated by brushed dc servo motor controller, 3-D structure used as a substrate/holder for microcantilever, digital power supply to apply bias to the Wheatstone bridge circuitry, operational amplifier in order to generate a larger output potential, Arduino card, and electronic oscilloscope (Agilent Technologies) for observing changes in voltage output. In the second setup, the basic components of the measurement system are an adjustable needle/probe to move the free tip of the strain gauge down, three degrees-of-freedom positioners (*x*, *y*, and *z* directions) for the needle/probe, 3-D structure used as a sample holder for microcantilever, and digital multimeter (Rohde&Schwarz HMC8012) in order to monitor immediate response of the strain gauge while under tension in terms of resistance measurement. Fig. 33, 34 shows the components of both experimental setups. In Fig. 35c, the Graphene-based SU-8 piezoresistive polymeric strain gauge is shown in a way of connecting to the electrical circuitry by bonding through electrical contact points as well.

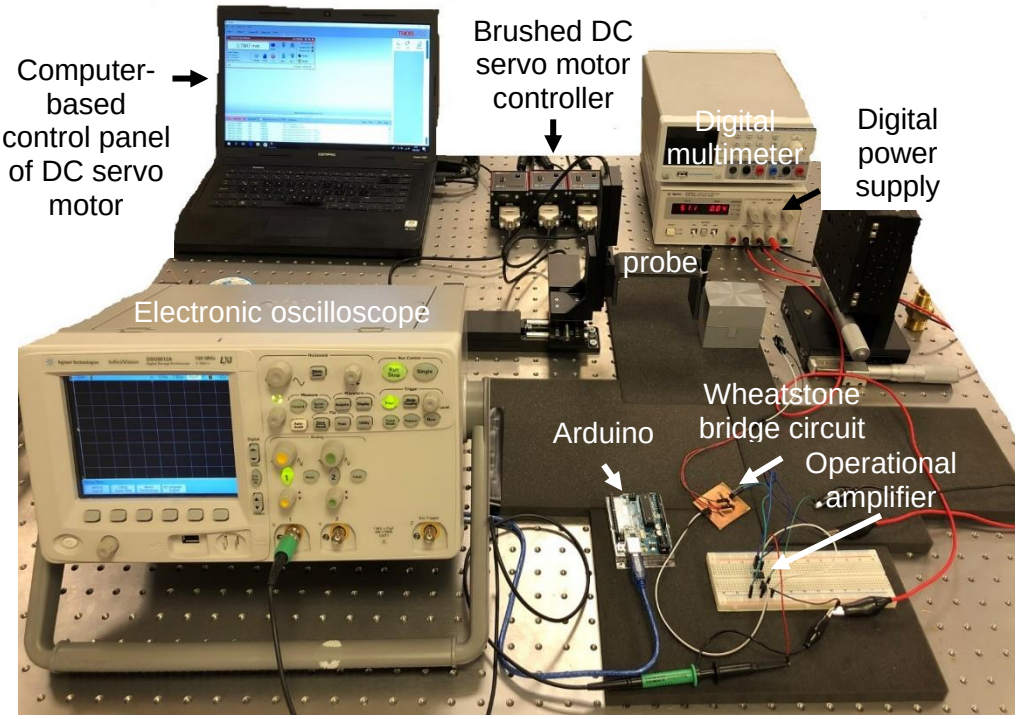

Figure 34. The first experimental setup components for microcantilever gauge factor measurement.

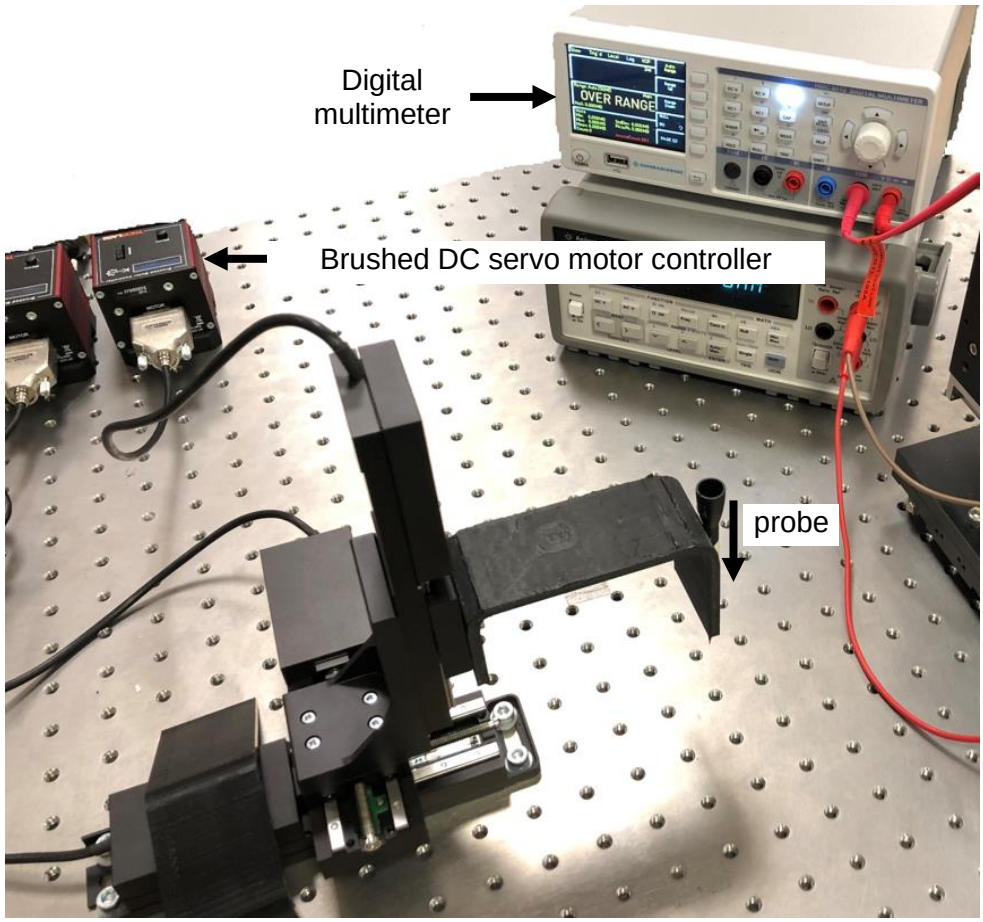

Figure 33. The second experimental setup components for microcantilever gauge factor measurement.

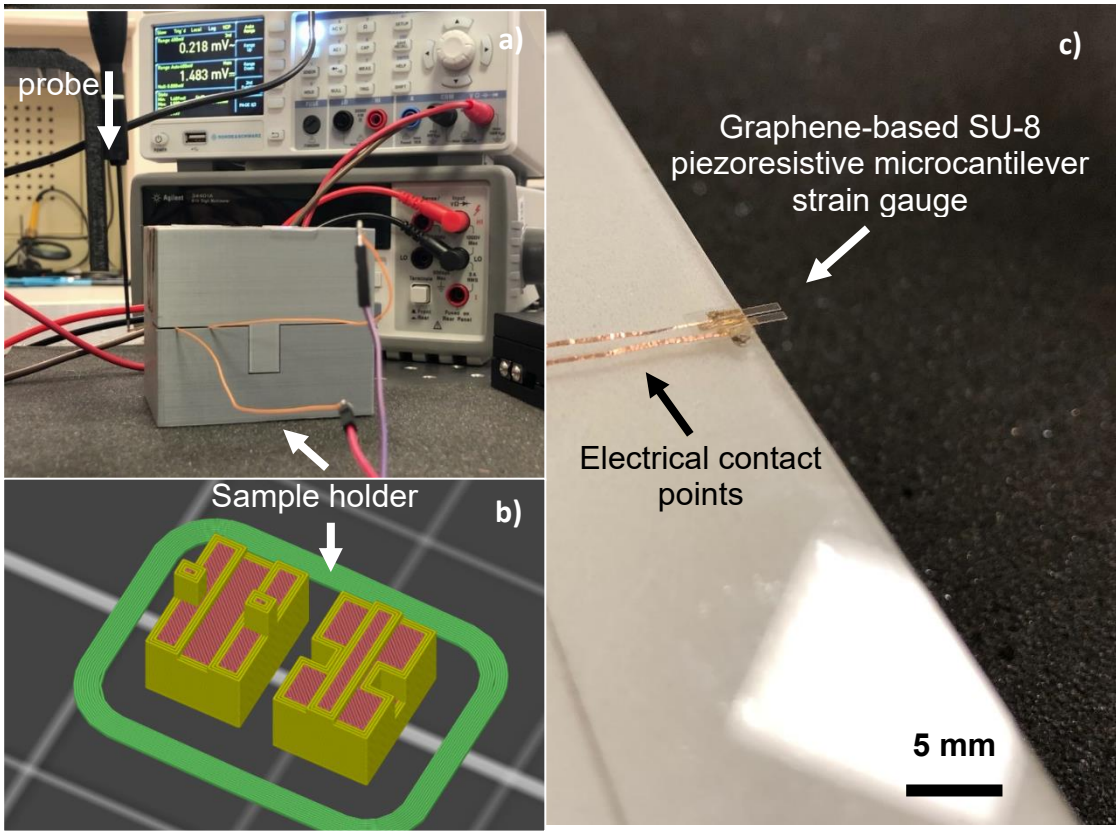

Figure 35. Image of the experimental setup with components. Inset (a) illustrates the moment when deforming the strain gauge; inset (b) details the 3-D structure of the substrate; inset (c) depicts the position of the strain gauge over electrical contact points.

5.2. Gauge Factor Measurement

The graphene-based SU-8 strain gauge was bonded by taping and soldering, and wired out for electrical measurements as shown in Fig 33. The applied stress was along the same direction of arrow as marked in Fig. 35a during measurements.

A typical factor to define the sensitivity of the strain sensor with respect to deformation is the Gauge Factor (GF), which was measured for the fabricated Graphene-based strain gauge formed on the SU-8 substrate by using a test rig (figure 35a). A full Wheatstone bridge was used to obtain an output signal in volts, which has shown proportionality to the resistance variation of the sensors (figure 33). R_1, R_2, and R_3 are resistors of known

resistance, and R_s represents the resistance of strain gauge as the unknown resistance. It may be noted that if R_1, R_2, R_3, R_s = R then the bridge is balanced, which means that the output voltage is zero, $V_{DC\ (out)}=0$. Therefore, an infinitesimal change in R_s that disrupts the balance is detected at high precision.

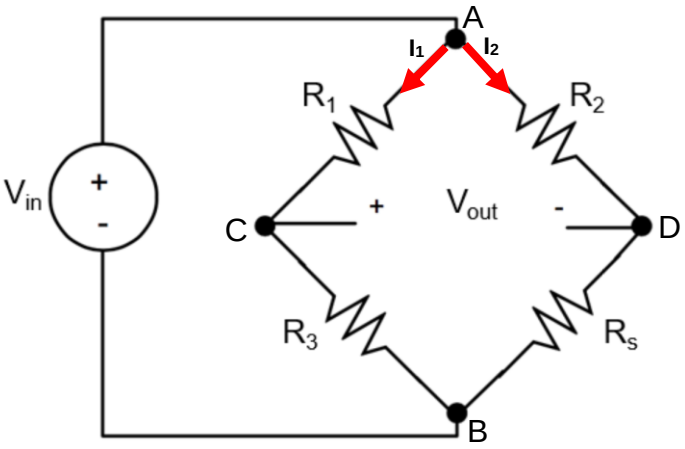

Figure 36. Wheatstone bridge circuit diagram.

In the bridge configuration, the strain gauge was connected to a side of the bridge, and three fixed resistors were inserted into each of the other three sides. Fig. 36 demonstrates the arrangement of the resistors and strain gauge in the Wheatstone bridge circuit diagram. For the electrical characterization of the Wheatstone bridge, a power supply (Agilent Technologies) was used to apply a bias voltage of 5 V to V_{in}, and then changes in the output voltage (V_{out}) were measured using oscilloscope (Agilent Technologies) while a bending moment was being exerted on the free end of the cantilever beam using the probe operated by brushed dc servo motor (figure 33). The gold pads of Graphene/SU-8 strain gauge was turned upside down in order to create some contact points with the conductive pathways formed on the surface of sample holder resulting in completing the electrical circuitry along the measurement setup. Thereafter, the Graphene-based SU-8 strain gauge was subjected to a uniaxial compressive (tensile) stress due to the downward deflection of the cantilever beam, thus causing changes in the electrical resistance of the strain gauge. All output sensitivity measurements related to deformations are identified by GF, and are calculated according to the Wheatstone bridge formula as derivated in the following equations:

$$
\begin{aligned}
V_{CD} &= V_{AC} - V_{AD} \\
V_C - V_D &= (V_A - V_C) - (V_A - V_D) \\
V_{DC} &= V_D - V_C \\
V_{DC\,(out)} &= V_{AC} - V_{AD}
\end{aligned} \tag{4}
$$

$$
V_{DC\,(out)} = I_1 \times R_1 - I_2 \times R_2 \tag{5}
$$

$$
\begin{aligned}
I_1 &= \frac{V_{in}}{R_1 + R_3} \text{ or } V_C = \left(\frac{R_3}{R_3 + R_1}\right) \times V_{in} \\
I_2 &= \frac{V_{in}}{R_2 + R_S} \text{ or } V_D = \left(\frac{R_S}{R_S + R_2}\right) \times V_{in}
\end{aligned} \tag{6}
$$

Eq. 6 is substituted in Eq. 5, thus resulting in the following form:

$$
V_{DC\,(out)} = V_{in} \times \left(\frac{R_1}{R_1 + R_3} - \frac{R_2}{R_2 + R_S}\right) \text{ or } V_{in} \times \left(\frac{R_S}{R_S + R_2} - \frac{R_3}{R_3 + R_1}\right) \tag{7}
$$

where V_{in} is the applied voltage of 5 V; R_1, R_2, and R_3 are fixed resistors of 88-Ω; R_s represents the unknown resistance value of the strain gauge, the output voltage was then obtained with the following equation:

$$
V_{DC\,(out)} = V_{in} \times \left(\frac{1}{2} - \frac{R}{R + R_S}\right) \tag{8}
$$

6. RESULTS AND DISCUSSION

Under a strain-free condition, the initial resistance (R_0) for the sensor was chosen as the resistance just before the resistance change begins, therefore the resistance values of graphene, and graphene/Au piezoresistor arms were around 35 kΩ and 13.5 Ω, respectively. Fig. 37, 38 shows a relative resistance change of the graphene-based SU-8 piezoresistive strain gauge sensor with respect to deflection as it was under bending state in which the deflection of 0.4 mm was applied individually to the graphene piezoresistor arm and graphene/Au piezoresistor arm in both of the experimental setup.

In the first experimental setup, GF of the fabricated Graphene/SU-8 strain gauge was measured by utilizing a 120-Ω Polyimide-based commercial strain gauge with GF of 2.14 as a reference strain gauge, which was used to represent one of the resistances in a complete Wheatstone bridge circuit, and the others were fixed resistances of 88-Ω. This commercial strain gauge was utilized to measure the axial strain at 1 mm deflection. The dc servo motor that was used to operate the probe as shown in Fig. 35a in order to deflect the free end of the strain gauge into down by 1 mm, which induced to change in its electrical resistance. As mentioned above, changes in the electrical resistance was derived from Eq. 8 defining the changes in V_{out}. Then, in the first experimental setup, it was observed that there have been many unidentified changes in the output voltage due to high noise and fluctuations when the arms of the graphene-based strain gauge were in bending state. Graphene/Au piezoresistor arm was giving unstable changes in output voltage, which could be attributed to the power consumed by the metal piezoresistive material owing to either its low electrical resistance, which results in increasing the temperature of the device, so that increases the noise level [355], or lack of contact points between conducting pads of the strain gauge and the wires. In contrast, the graphene piezoresistor arm of the strain gauge has shown some changes in output voltage under deflection. However, the noise level in the graph of resistance change as the function of

deflection was high, therefore there was no correlation obtained to interpret the data.

On the other hand, the second experimental setup gave an interpretable result showing the changes in resistance of both graphene and graphene/Au piezoresistor arm measured by a digital multimeter (Rohde&Schwarz HMC8012), where the immediate responses of the strain gauge in regard to the incremental deflections have been able to monitor. The sensitivity of the microcantilever is defined based on its gauge factor, which is the ratio of the relative change in resistance to the strain. The resistance change is caused by the change in total geometrical variation of the serpentine-shape graphene and graphene/Au layers.

The relation between the changes in strain and electrical resistance is deduced using Eq. 9:

$$GF = \frac{\Delta R/R}{\varepsilon} \tag{9}$$

where R is the strain-free graphene; ΔR refers to the change in the electrical resistance of the graphene due to the strain, $\mathcal{E}$.

Hooke's law describes one-dimensional stress in the following equation:

$$\sigma = \varepsilon \times E \tag{10}$$

where the stress, σ, occurs at the clamped end of the microcantilever; E is the Young's modulus of the substrate material; ε is the strain referring the change in dimension longitudinally.

Polyimide (PI)-based commercial strain gauge was bonded to the circuitry by wires as illustrated in Fig. 35a in order to calculate the bending stress experienced at its fixed end. It was deflected down by the probe with a step size of 0.02 mm until the free end of the strain gauge has been deflected to the point of 0.4 mm, which resulted in changes in resistance of the constantan alloy (copper-nickel) in that strain gauge as shown in Fig. 37.

Therefore, the change in relative resistance, $\Delta R/R$, was found 0.000165908 from the graph, and the GF of PI-based commercial strain gauge was given 2.14, then by using Eq. 9 the strain was found 77.5269 με, which was subsequently inserted into Eq. 10 with Young's modulus of PI of 2.5 GPa in order to calculate the stress of 0.000193817 GPa. The fact that the stress has been exerted on the surface of the cantilever by the same probe, the calculated stress was considered as the same for those cases where graphene-based SU-8 strain gauges were deflected at 0.4 mm.

The deflection tests of graphene-based strain gauges were performed for both graphene and graphene/Au arm, respectively. Subsequent the deflection, by inserting the stress value calculated in the previous part, and Young's modulus of SU-8 known as 3.6 GPa into Eq. 10, the strain was found as 53.84 με, which has been taken into account as the same for both graphene arm and graphene/Au arm. After that, the graphene and graphene/Au arm was deflected at several times, which resulted in obtaining the relative resistance change and the corresponding gauge factors as given in Table 7.

Table 7. Microcantilever displacement and the corresponding resistances, gauge factors, strains, and stresses for both graphene/Au and graphene arm of the SU-8 strain gauges.

Parameter	Commercial strain gauge	Graphene/Au arm	Graphene/Au arm	Graphene/Au arm	Graphene/Au arm
Deflection (mm)	0,4028	0,4028	0,4028	0,4028	0,4028
R_f (ohm)	120,569	13,965	14,048	14,034	13,029
R_i (ohm)	120,549	14,145	14,240	14,224	12,89
ΔR	0,020	-0,180	-0,192	-0,190	0,139
ΔR/R	0,000165908	-0,012725345	-0,013483146	-0,013357705	0,010783553
|GF|	2,1400000	-236,3629682	-250,4385158	-248,1085549	200,2957641
Strain (ε)	7,75269E-05	5,38381E-05	5,38381E-05	5,38381E-05	5,38381E-05
Young's modulus (GPa)	2,5	3,6	3,6	3,6	3,6
Stress (GPa)	0,000193817	0,000193817	0,000193817	0,000193817	0,000193817

Parameter	Commercial strain gauge	Graphene arm	Graphene arm	Graphene arm	Graphene arm
Deflection (mm)	0,4028	0,4028	0,4028	0,4028	0,4028
R_f (ohm)	120,569	40,352	40,750	37,711	37,740
R_i (ohm)	120,549	39,916	40,585	37,108	37,898
ΔR	0,020	0,436	0,165	0,604	-0,158
ΔR/R	0,000165908	0,010922938	0,004065541	0,016263559	-0,004186539
|GF|	2,14	202,8847281	75,51413914	302,0824258	-77,4373847
Strain (Ɛ)	7,75269E-05	5,38381E-05	5,38381E-05	5,38381E-05	5,38381E-05
Young's modulus (GPa)	2,5	3,6	3,6	3,6	3,6
Stress (GPa)	0,000193817	0,000193817	0,000193817	0,000193817	0,000193817

In Table 7, some GFs show negative values due to the sign of relative resistance change for those cases where the resistance of piezoresistor decreases. The fact that the strain gauge was flipped over as it was inserted in the printed circuit board (PCB), the graphene and graphene/Au patterns left at the bottom side of the cantilever. Therefore, compressive stress occurred at the bottom side of the cantilever due to the bending moment, which resulted in decreasing the resistance of the piezoresistive materials.

The relationships between the resistance variation of the sensor with respect to deflection are revealed in Fig. 37 (a, b) and Fig. 38 (a, b).

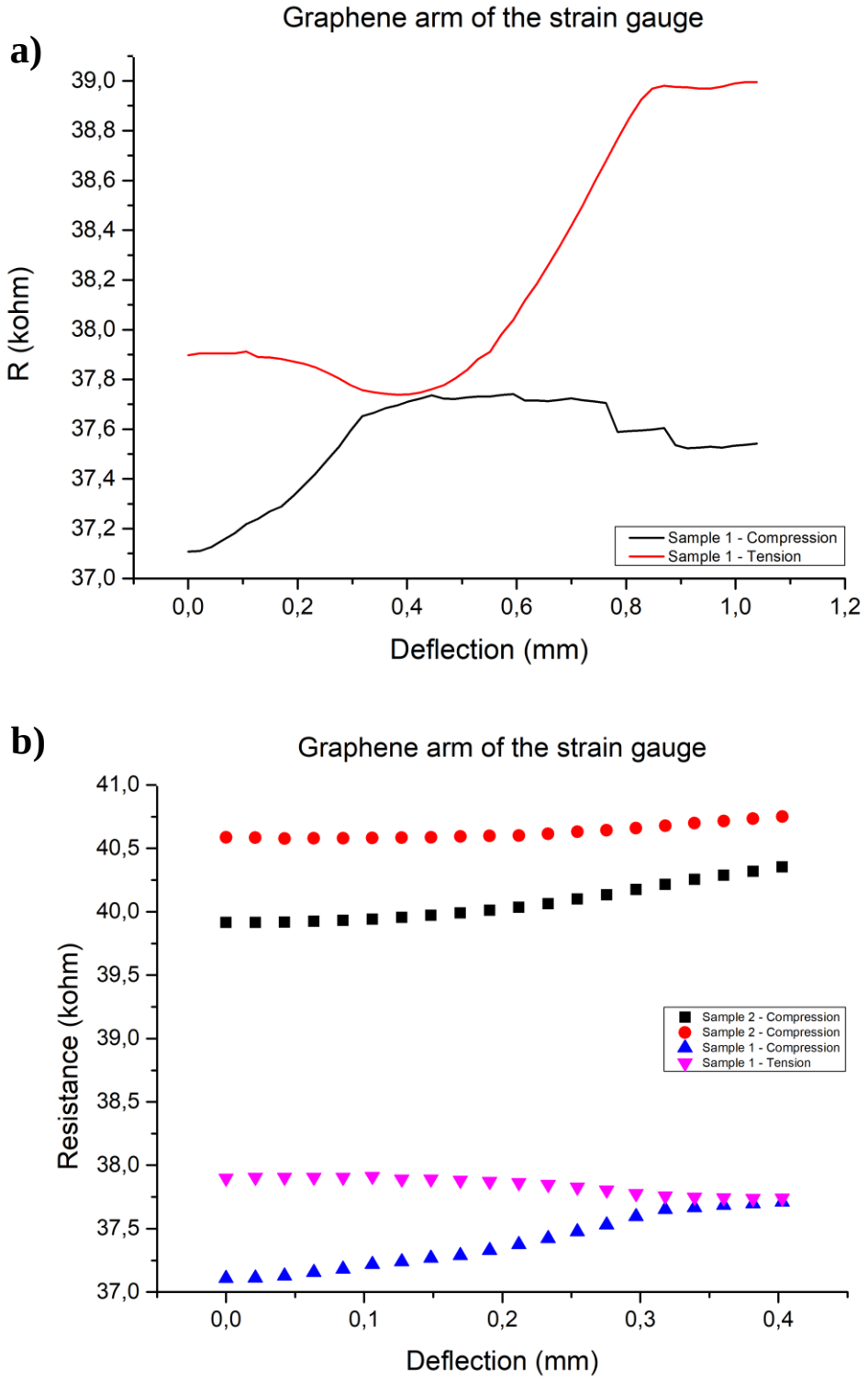

Figure 37. (a) The resistance changes of the graphene piezoresistor arm deflected by 1 mm. (b) Comparison of the changes in resistance of sample 1 and sample 2 under tension and compression deflected by 0.4 mm.

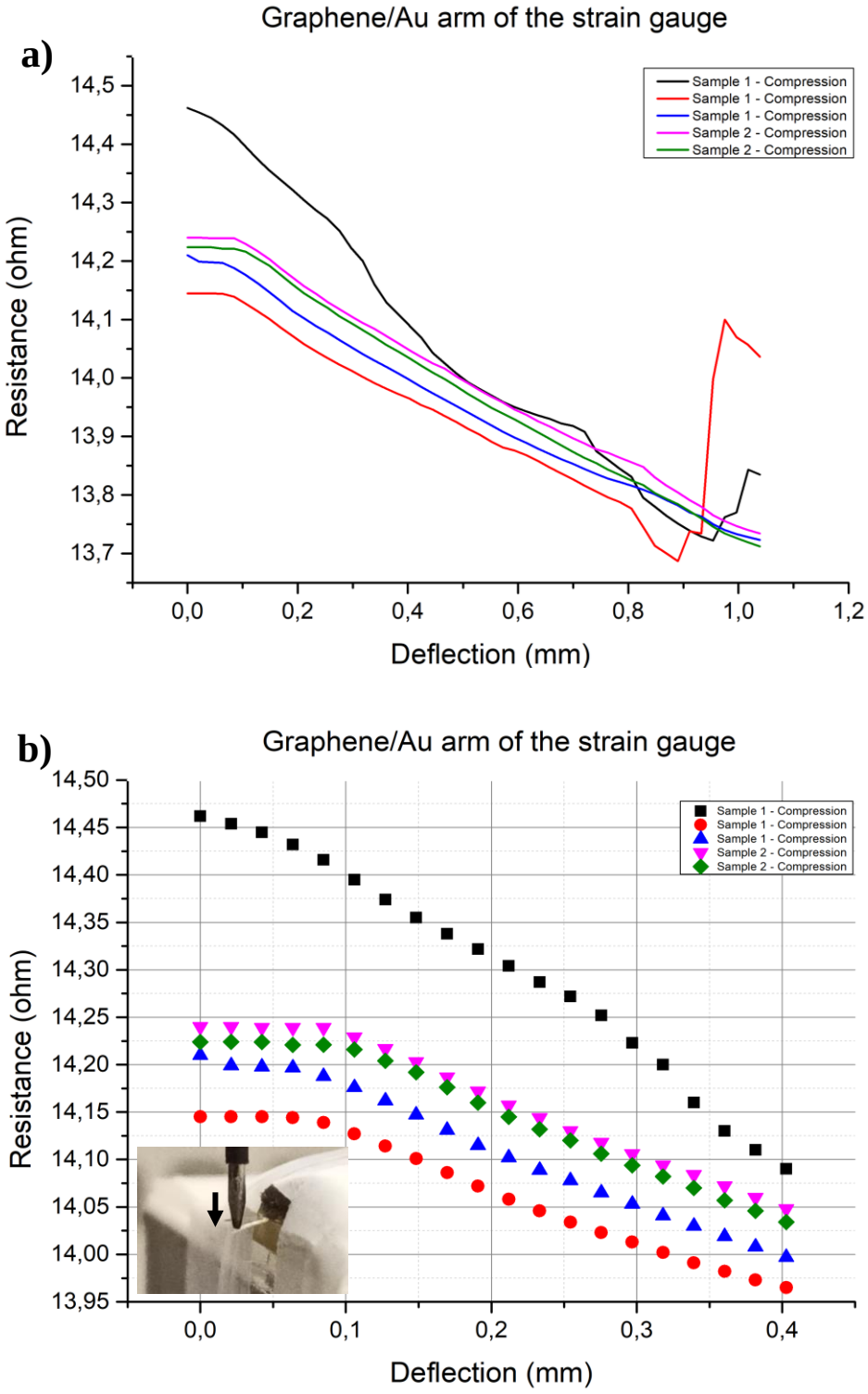

Figure 38. (a) The resistance changes with respect to deflection for sample 1 and sample 2 deflected by 1 mm. (b) Each plot illustrates the changes in resistance of graphene/Au arms under compression obtained at different times with deflection of 0.4 mm.

Variations in the resistance change at some points are caused by cleavage revealing in the graphene and irregular elongation in the SU-8 structure. There is a drop observed in resistance, which we anticipate to be due to possible ripples ocur in 2D graphene layers when strain is applied. It can also be noted that SU-8 poymer matrix can be deformed plastically. Furthermore, metal piezoresistive materials are considered as high power consuming materials since they show high conductivity, which cause increasing in the device temperature, and so increasing the level of noise, and even resulting in creating the crash in the entire of sensor [355].

The straight line slope crossing the points defines the deflection sensitivity, which is shown in the graph of change in relative resistance as a function of strain in response to tension and compression. Eventually, it yields a gauge factor for each strain gauge measured at several times as depicted in Fig. 39 (a-h).

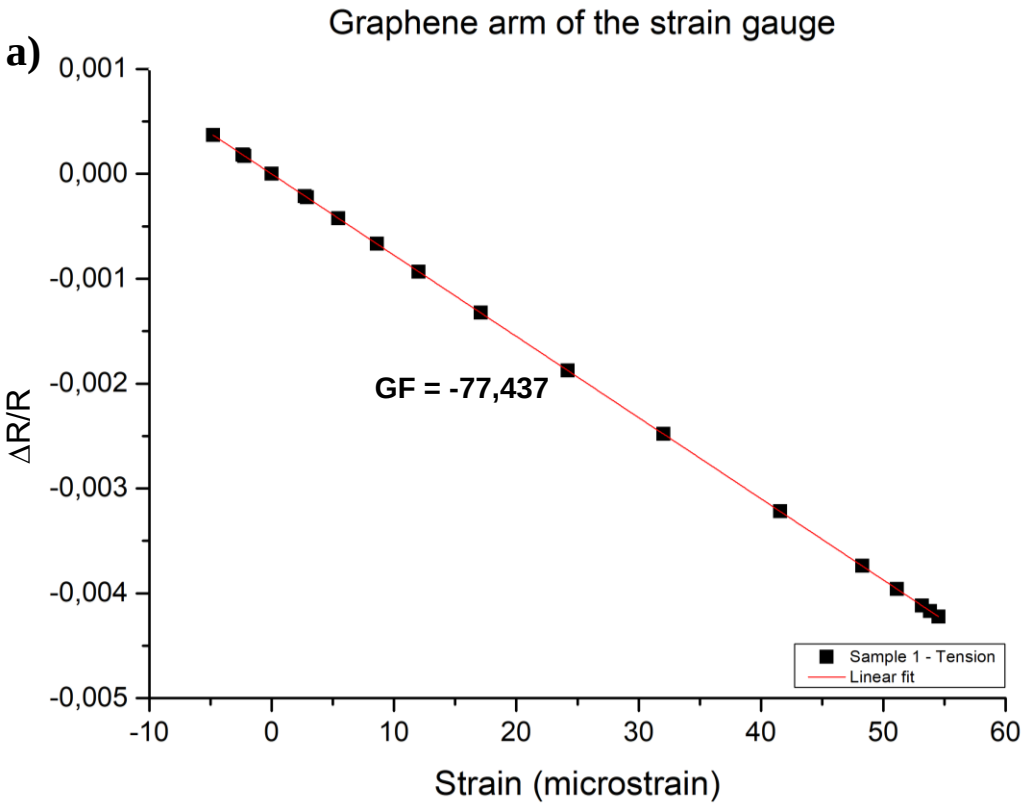
a)
Graphene arm of the strain gauge
ΔR/R
0,001
0,000
-0,001
-0,002
-0,003
-0,004
-0,005
GF = -77,437
Sample 1 - Tension
Linear fit
-10
0
10
20
30
40
50
60
Strain (microstrain)

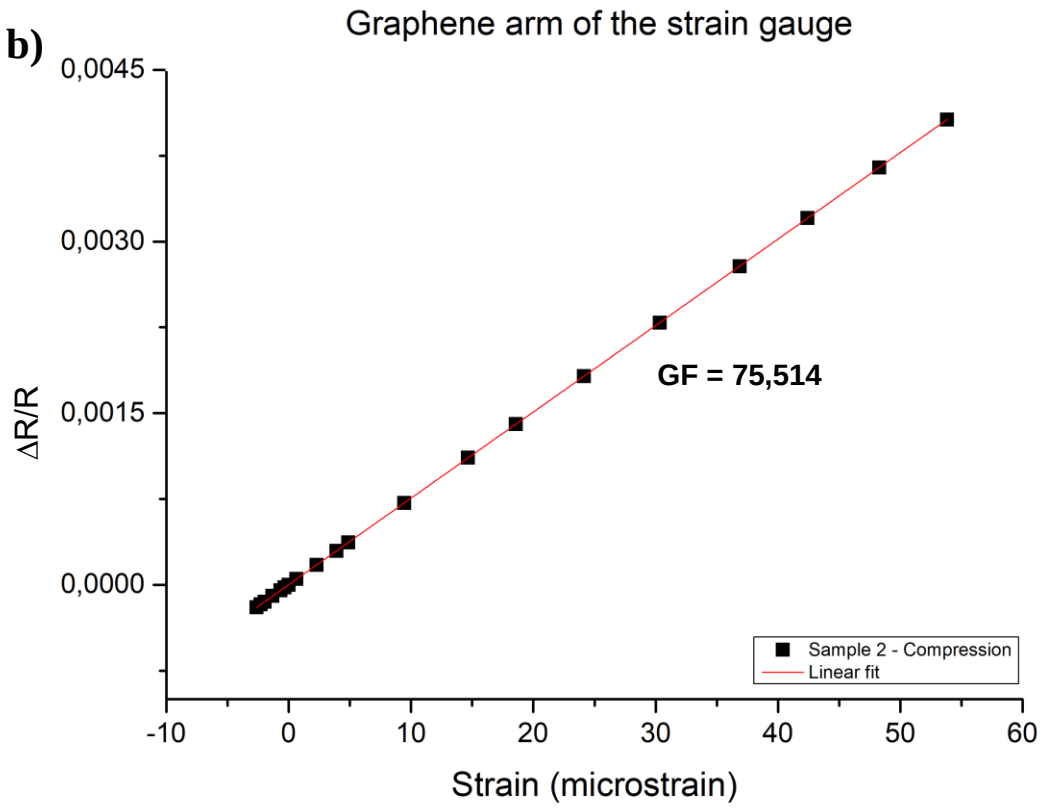
b)
Graphene arm of the strain gauge
ΔR/R
0,0045
0,0030
0,0015
0,0000
GF = 75,514
Sample 2 - Compression
Linear fit
-10
0
10
20
30
40
50
60
Strain (microstrain)

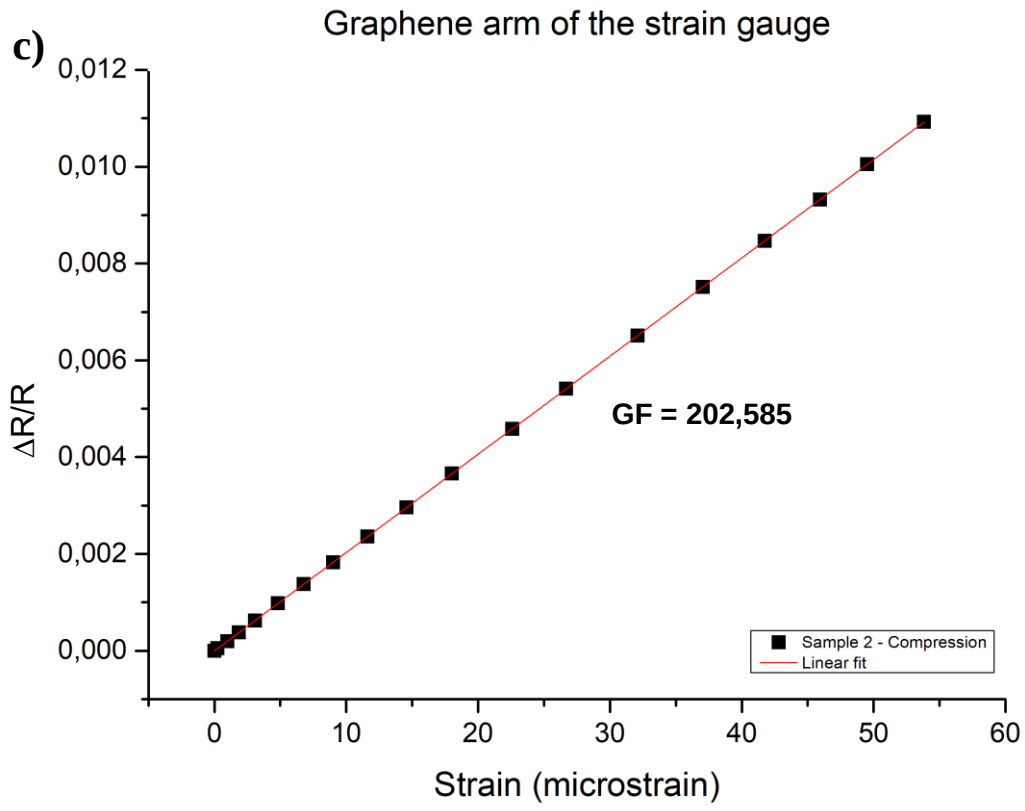
c)
Graphene arm of the strain gauge
ΔR/R
0,012
0,010
0,008
0,006
0,004
0,002
0,000
GF = 202,585
Sample 2 - Compression
Linear fit
0
10
20
30
40
50
60
Strain (microstrain)

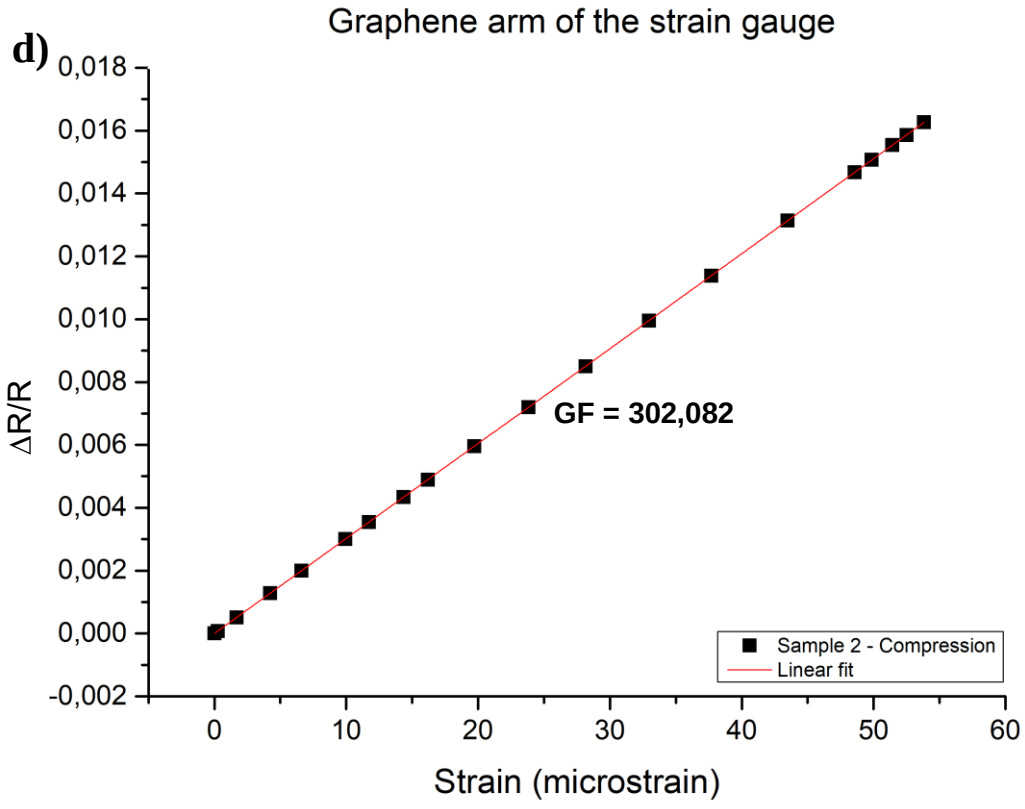
d)
Graphene arm of the strain gauge
ΔR/R
0,018
0,016
0,014
0,012
0,010
0,008
0,006
0,004
0,002
0,000
-0,002
GF = 302,082
Sample 2 - Compression
Linear fit
0
10
20
30
40
50
60
Strain (microstrain)

e)

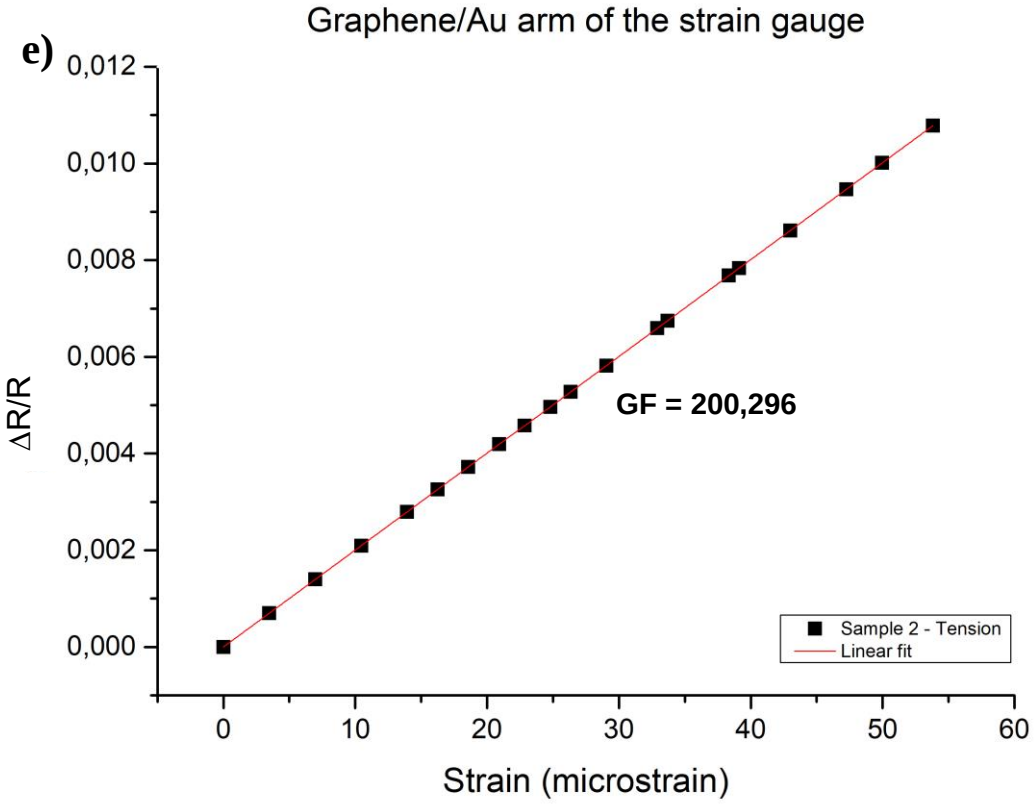
Graphene/Au arm of the strain gauge
ΔR/R
0,012
0,010
0,008
0,006
0,004
0,002
0,000
GF = 200,296
Sample 2 - Tension
Linear fit
0
10
20
30
40
50
60
Strain (microstrain)

f)

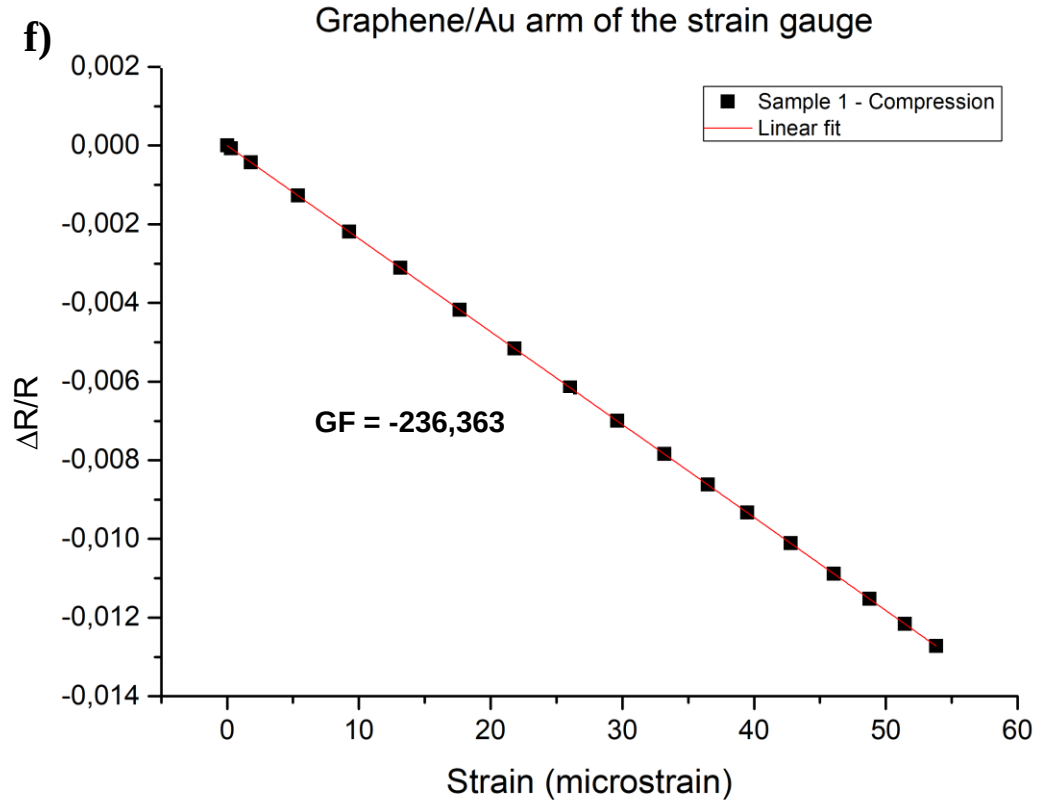
Graphene/Au arm of the strain gauge
ΔR/R
0,002
0,000
-0,002
-0,004
-0,006
-0,008
-0,010
-0,012
-0,014
GF = -236,363
Sample 1 - Compression
Linear fit
0
10
20
30
40
50
60
Strain (microstrain)

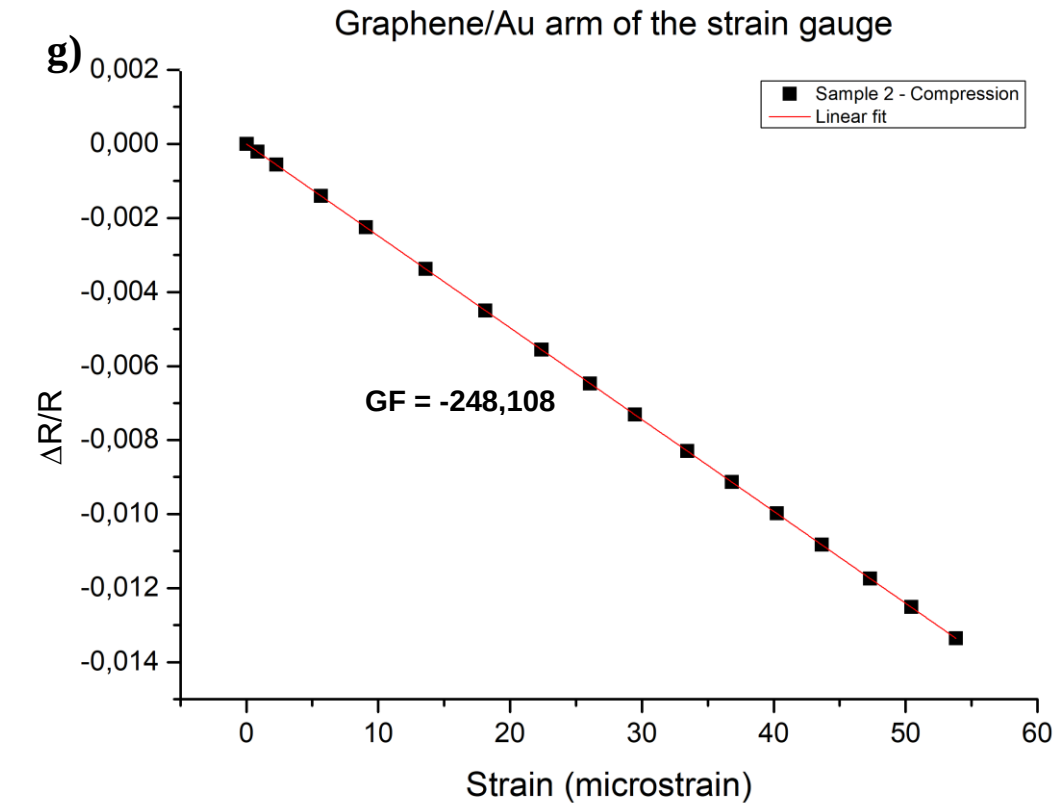

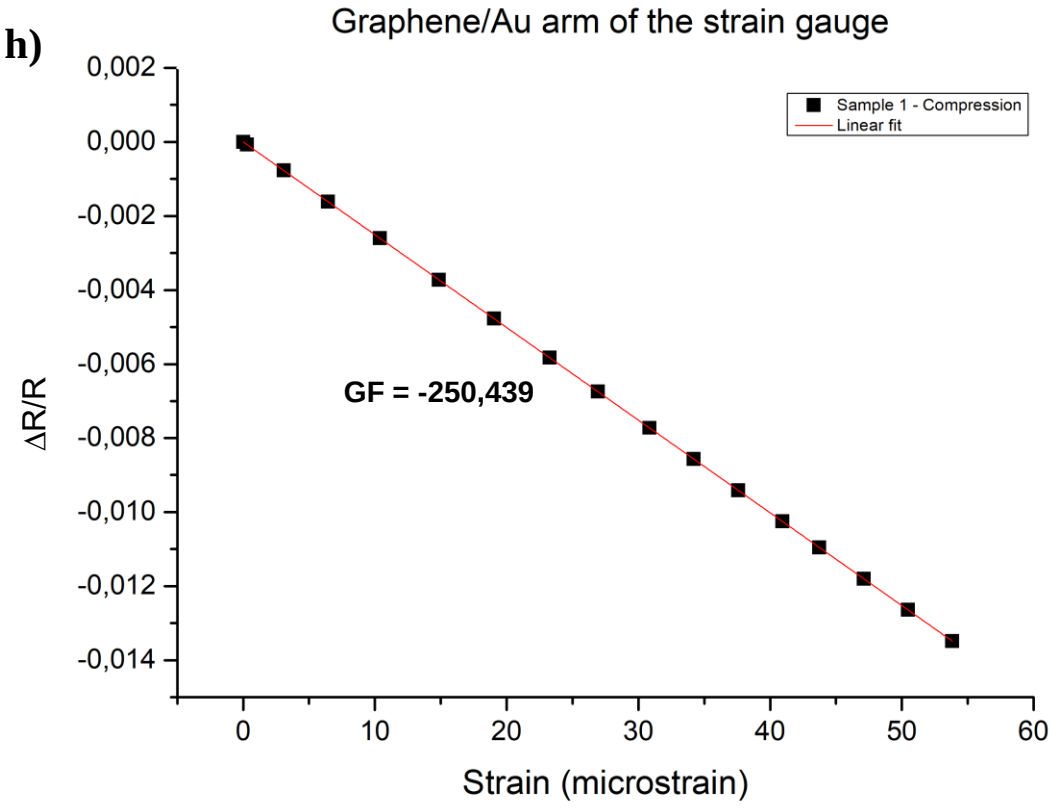

Figure 39. (a-h) Deflection sensitivity of graphene and graphene/Au arm of the strain gauge with respect to changes in strain.

As the linear relationships between the relative change in resistance in regard to the strain are revealed both for the graphene arm and graphene/Au arm of the strain gauge samples in Fig. 39 (a-h), the graphene arm of the strain gauge shows negative in relative resistance change as a function of strain when it is in tensile mode, which is unexpected for this case, so it is attributed to the fact that the width of the piezoresistive sensing grid lines increases and the length decreases due to Poisson's effect. On the other hand, the change in relative resistance is positive with regard to the strain when the arm is in compressive mode, which is the reverse in the case of tensile mode. However, the graphene/Au arm has positive of the relative resistance change in tensile mode, which is expected due to the fact that the concept of piezoresistive effect is proven by the concept of geometrical variation dependant resistance change of the graphene/Au piezoresistive materials. Nevertheless, compressive mode causes decreasing the relative change in resistance of the graphene/Au arm in regard to strain, which is the same case as the graphene arm under tension.

7. CONCLUSION

This work focuses on the design, fabrication, and performance of an SU-8 based strain gauge with graphene and gold as piezoresistive materials. The sensitivity of polymer-based microcantilevers can be enhanced using metal or carbon-based piezoresistive materials, which paves the way for competing with conventional piezoresistive microcantilever type sensors fabricated on silicon substrates, which results in obtaining higher sensitivity. Even though the piezoresistance effect of silicon provides higher gauge factor as compared to the other piezoresistive materials, the use of a metal or carbon-based material integrated in a polymeric structure can increase the sensitivity of device. Among the carbon-based materials, graphene has been considered as a distinctive and a promising material substituting the conventionally used metals and silicon. In the literature, several practices have been studied for which a flexible and compatible material has been suggested as the structure of sensor. Polymeric cantilevers like SU-8 promises low Young's modulus, therefore metal integrated microcantilever sensor based on SU-8 is almost as sensitive as microcantilevers based on Si. The gauge factor (GF) is defined as sensitivity of a strain gauge, which is the proportion of a relative resistance change to a strain. In strain sensing applications, graphene is used as electrode because of its high surface conductivity and Young's Modulus values, bringing robustness and high elastic stiffness. The load transfer capabilities and structural strength are two main characteristics of graphene, making it a perfect candidate to combine with polymers.

In this thesis, the proposed methods of patterning of graphene and gold, and the design and fabrication procedures with dedicated parameters to obtain SU-8 polymeric cantilever strain gauge have been demonstrated. Graphene has been preffered as a piezoresistive material that is considered as a valid material for flexible sensor applications due to its distinguished electrical and mechanical characteristics. Furthermore, gold has been utilized as another piezoresistive material, which shows good electrical properties, and

provides better compatibility with SU-8 substrate, therefore no adhesional layer is required. A graphene-based SU-8 polymeric cantilever strain gauge was fabricated by following the patterning procedures including the techniques utilized in microfabrication methods that are known as etching, thin film deposition, lithography, and substrate removal. Graphene and gold were masked into a desired pattern, then a method for etching and substrate removing of the graphene and gold layers with SU-8 polymeric substrate was also developed. The fabricated graphene-based SU-8 strain gauge was performed under bending test in order to determine the graphene piezoresistivity thus its respond to strain called sensitivity.

In conclusion, the graphene arm of sample 1 was under tension yielded gauge factor of -77.437. Furthermore, the graphene/Au arm of sample 2 was subjected to tension at once, which gave the gauge factor of 200.295. On the other hand, the graphene/Au arms of sample 1 and 2 were experienced compressive stress at 4 times, and those resulted in obtaining the gauge factor of -236.363, -248.108, -250.439, and -278.417, respectively. According to the calculations, we achieved that the gauge factors of graphene-based SU-8 strain gauges is higher than those of commercial metal-alloy-based strain gauges. In addition, the consistency of the proposed method is highlighted, which enables to fabricate the graphene-based strain gauges that are sensitive than commercial metallic strain gauges and more adaptable than silicon single-crystal strain gauges. The linear relationships between the resistance variation of the sensor in bending state as the result of deflection that was experienced by the tip of the graphene piezoresistor arm and the graphene/Au piezoresistor arm of the cantilever were demonstrated.

BIBLIOGRAPHY

1. Wang, Y., et al., *Wearable and highly sensitive graphene strain sensors for human motion monitoring.* Advanced Functional Materials, 2014. **24**(29): p. 4666-4670.
2. Choi, H., et al., *Flexible and transparent gas molecule sensor integrated with sensing and heating graphene layers.* Small, 2014. **10**(18): p. 3685-3691.
3. Lee, T., et al., *Flexible textile strain wireless sensor functionalized with hybrid carbon nanomaterials supported ZnO nanowires with controlled aspect ratio.* Advanced Functional Materials, 2016. **26**(34): p. 6206-6214.
4. Ashruf, C., *Thin flexible pressure sensors.* Sensor Review, 2002.
5. Paradiso, R., G. Loriga, and N. Taccini, *A wearable health care system based on knitted integrated sensors.* IEEE transactions on Information Technology in biomedicine, 2005. **9**(3): p. 337-344.
6. Luo, S., W. Obitayo, and T. Liu, *SWCNT-thin-film-enabled fiber sensors for lifelong structural health monitoring of polymeric composites-From manufacturing to utilization to failure.* Carbon, 2014. **76**: p. 321-329.
7. Lynch, J.P., et al., *Design of piezoresistive MEMS-based accelerometer for integration with wireless sensing unit for structural monitoring.* Journal of Aerospace Engineering, 2003. **16**(3): p. 108-114.
8. Sun, S., et al., *Nano graphite platelets-enabled piezoresistive cementitious composites for structural health monitoring.* Construction and Building Materials, 2017. **136**: p. 314-328.
9. Papadimitratos, P., et al., *Vehicular communication systems: Enabling technologies, applications, and future outlook on intelligent transportation.* IEEE communications magazine, 2009. **47**(11): p. 84-95.
10. Fehlmann, S., et al. *Application of detection and recognition algorithms to persistent wide area surveillance*. in *2013 International Conference on Digital Image Computing: Techniques and Applications (DICTA)*. 2013. IEEE.
11. Sorba, F. and C. Martin-Olmos, *High resolution polymer coated strain sensors for in-liquid operation.* Microelectronic Engineering, 2018. **191**: p. 38-41.
12. Filippidou, M., et al., *A flexible strain sensor made of graphene nanoplatelets/polydimethylsiloxane nanocomposite.* Microelectronic Engineering, 2015. **142**: p. 7-11.
13. Kanda, Y., *Piezoresistance effect of silicon.* Sensors and Actuators A: Physical, 1991. **28**(2): p. 83-91.
14. Middelhoek, S. and S.A. Audet, *Silicon sensors*. 1989: Academic Press.
15. Smith, C.S., *Piezoresistance effect in germanium and silicon.* Physical review, 1954. **94**(1): p. 42.
16. Niu, D., et al., *Graphene-elastomer nanocomposites based flexible piezoresistive sensors for strain and pressure detection.* Materials Research Bulletin, 2018. **102**: p. 92-99.
17. Jing, Z., Z. Guang-Yu, and S. Dong-Xia, *Review of graphene-based strain sensors.* Chinese Physics B, 2013. **22**(5): p. 057701.
18. Johansson, A., et al., *SU-8 cantilever chip interconnection.* Journal of Micromechanics and Microengineering, 2006. **16**(2): p. 314.

19. Martin-Olmos, C., et al., *Conductivity of SU-8 Thin Films through Atomic Force Microscopy Nano-Patterning.* Advanced Functional Materials, 2012. **22**(7): p. 1482-1488.
20. Genolet, G., et al., *Soft, entirely photoplastic probes for scanning force microscopy.* Review of scientific instruments, 1999. **70**(5): p. 2398-2401.
21. Lorenz, H., et al., *SU-8: a low-cost negative resist for MEMS.* Journal of Micromechanics and Microengineering, 1997. **7**(3): p. 121.
22. Thaysen, J., et al. *SU-8 based piezoresistive mechanical sensor*. in *Technical Digest. MEMS 2002 IEEE International Conference. Fifteenth IEEE International Conference on Micro Electro Mechanical Systems (Cat. No. 02CH37266)*. 2002. IEEE.
23. Han, B. and J. Ou, *Embedded piezoresistive cement-based stress/strain sensor.* Sensors and Actuators A: Physical, 2007. **138**(2): p. 294-298.
24. Ren, J., et al., *Environmentally-friendly conductive cotton fabric as flexible strain sensor based on hot press reduced graphene oxide.* Carbon, 2017. **111**: p. 622-630.
25. Sayar Irani, F. and B. Tunaboylu, *SAW humidity sensor sensitivity enhancement via electrospraying of silver nanowires.* Sensors, 2016. **16**(12): p. 2024.
26. Chen, X., L. Zhang, and S. Chen, *Large area CVD growth of graphene.* Synthetic Metals, 2015. **210**: p. 95-108.
27. Jo, G., et al., *The application of graphene as electrodes in electrical and optical devices.* Nanotechnology, 2012. **23**(11): p. 112001.
28. O'Grady, G., et al., *A comparison of gold versus silver electrode contacts for high-resolution gastric electrical mapping using flexible printed circuit board arrays.* Physiological measurement, 2011. **32**(3): p. N13.
29. Novoselov, K.S., et al., *Two-dimensional atomic crystals.* Proceedings of the National Academy of Sciences, 2005. **102**(30): p. 10451-10453.
30. Zhang, Y., et al., *Experimental observation of the quantum Hall effect and Berry's phase in graphene.* nature, 2005. **438**(7065): p. 201.
31. Lee, C., et al., *Measurement of the elastic properties and intrinsic strength of monolayer graphene.* science, 2008. **321**(5887): p. 385-388.
32. Nair, R.R., et al., *Fine structure constant defines visual transparency of graphene.* Science, 2008. **320**(5881): p. 1308-1308.
33. Schedin, F., et al., *Detection of individual gas molecules adsorbed on graphene.* Nature materials, 2007. **6**(9): p. 652.
34. Tien, H.-W., et al., *Preparation of transparent, conductive films by graphene nanosheet deposition on hydrophilic or hydrophobic surfaces through control of the pH value.* Journal of Materials Chemistry, 2012. **22**(6): p. 2545-2552.
35. Allen, M.J., V.C. Tung, and R.B. Kaner, *Honeycomb carbon: a review of graphene.* Chemical reviews, 2010. **110**(1): p. 132-145.
36. Ando, T., *The electronic properties of graphene and carbon nanotubes.* NPG asia materials, 2009. **1**(1): p. 17.
37. Nilsson, J., et al., *Electronic properties of graphene multilayers.* Physical review letters, 2006. **97**(26): p. 266801.
38. Kozubek, R., et al., *Fabrication of Defective Single Layers of Hexagonal Boron Nitride on Various Supports for Potential Applications in Catalysis and DNA Sequencing.* ACS Applied Nano Materials, 2018. **1**(8): p. 3765-3773.
39. Li, J., et al., *Electron–hole symmetry breaking in charge transport in nitrogen-doped graphene.* ACS nano, 2017. **11**(5): p. 4641-4650.
40. Mackin, C., et al., *Chemiresistive graphene sensors for ammonia detection.* ACS

applied materials & interfaces, 2018. **10**(18): p. 16169-16176.
41. Su, Q. and S.J. Koester, *Understanding Sources of Electrical Disorder in Graphene Grown by Chemical Vapor Deposition for Wafer-Scale Device Applications.* ACS Applied Nano Materials, 2019.
42. Yang, S.-J., et al., *All-Dry Transfer of Graphene Film by Van der Waals Interactions.* Nano letters, 2019.
43. De Fazio, D., et al., *High-mobility, wet-transferred graphene grown by chemical vapor deposition.* ACS nano, 2019. **13**(8): p. 8926-8935.
44. Gnisci, A., et al., *Ethanol-CVD Growth of Sub-mm Single-Crystal Graphene on Flat Cu Surfaces.* The Journal of Physical Chemistry C, 2018. **122**(50): p. 28830-28838.
45. Mojtabavi, M., et al., *Single-Molecule Sensing Using Nanopores in Two-Dimensional Transition Metal Carbide (MXene) Membranes.* ACS nano, 2019. **13**(3): p. 3042-3053.
46. Nathawat, J., et al., *Transient Response of h-BN-Encapsulated Graphene Transistors: Signatures of Self-Heating and Hot-Carrier Trapping.* ACS Omega, 2019. **4**(2): p. 4082-4090.
47. Srinivasan, B.M., et al., *Oxygen-promoted chemical vapor deposition of graphene on copper: a combined modeling and experimental study.* ACS nano, 2018. **12**(9): p. 9372-9380.
48. Petrone, N., et al., *Chemical vapor deposition-derived graphene with electrical performance of exfoliated graphene.* Nano letters, 2012. **12**(6): p. 2751-2756.
49. Geim, A.K., *Graphene: status and prospects.* science, 2009. **324**(5934): p. 1530-1534.
50. Neto, A.C., et al., *The electronic properties of graphene.* Reviews of modern physics, 2009. **81**(1): p. 109.
51. Ovid'Ko, I., *Mechanical properties of graphene.* Rev. Adv. Mater. Sci, 2013. **34**(1): p. 1-11.
52. Zhao, X., et al., *Enhanced mechanical properties of graphene-based poly (vinyl alcohol) composites.* Macromolecules, 2010. **43**(5): p. 2357-2363.
53. Frank, I., et al., *Mechanical properties of suspended graphene sheets.* Journal of Vacuum Science & Technology B: Microelectronics and Nanometer Structures Processing, Measurement, and Phenomena, 2007. **25**(6): p. 2558-2561.
54. Shaby, S.M., M. Premi, and B. Martin, *Enhancing the performance of mems piezoresistive pressure sensor using germanium nanowire.* Procedia Materials Science, 2015. **10**: p. 254-262.
55. Qin, Y., et al., *A high performance torque sensor for milling based on a piezoresistive MEMS strain gauge.* Sensors, 2016. **16**(4): p. 513.
56. Seto, J.Y., *Piezoresistive properties of polycrystalline silicon.* Journal of Applied Physics, 1976. **47**(11): p. 4780-4783.
57. KHATIBI, E., *Piezoresistivity of graphene.* 2011.
58. Bonavolontà, C., et al., *Characterization of piezoresistive properties of graphene-supported polymer coating for strain sensor applications.* Sensors and Actuators A: Physical, 2016. **252**: p. 26-34.
59. Smith, A.D., et al., *Piezoresistive properties of suspended graphene membranes under uniaxial and biaxial strain in nanoelectromechanical pressure sensors.* ACS nano, 2016. **10**(11): p. 9879-9886.
60. Gui, G., J. Li, and J. Zhong, *Band structure engineering of graphene by strain: first-principles calculations.* Physical Review B, 2008. **78**(7): p. 075435.
61. Kim, Y.-J., et al., *Preparation of piezoresistive nano smart hybrid material*

based on graphene. Current Applied Physics, 2011. **11**(1): p. S350-S352.
62. Zhang, X.W., et al., *Time dependence of piezoresistance for the conductor-filled polymer composites.* Journal of Polymer Science part B: polymer physics, 2000. **38**(21): p. 2739-2749.
63. Choi, S.-M., S.-H. Jhi, and Y.-W. Son, *Controlling energy gap of bilayer graphene by strain.* Nano letters, 2010. **10**(9): p. 3486-3489.
64. Cocco, G., E. Cadelano, and L. Colombo, *Gap opening in graphene by shear strain.* Physical Review B, 2010. **81**(24): p. 241412.
65. Farjam, M. and H. Rafii-Tabar, *Comment on "Band structure engineering of graphene by strain: First-principles calculations".* Physical Review B, 2009. **80**(16): p. 167401.
66. Jiang, J.-W. and J.-S. Wang, *Bright and dark modes induced by graphene bubbles.* EPL (Europhysics Letters), 2012. **97**(3): p. 36004.
67. Lu, Y. and J. Guo, *Band gap of strained graphene nanoribbons.* Nano Research, 2010. **3**(3): p. 189-199.
68. Pellegrino, F., G. Angilella, and R. Pucci, *Ballistic transport properties across nonuniform strain barriers in graphene.* High Pressure Research, 2012. **32**(1): p. 18-22.
69. Hwang, C., et al., *Fermi velocity engineering in graphene by substrate modification.* Scientific reports, 2012. **2**: p. 590.
70. Bhuyan, M.S.A., et al., *Synthesis of graphene.* International Nano Letters, 2016. **6**(2): p. 65-83.
71. Tomori, H., et al., *Introducing nonuniform strain to graphene using dielectric nanopillars.* Applied physics express, 2011. **4**(7): p. 075102.
72. Lee, H.C., et al., *Review of the synthesis, transfer, characterization and growth mechanisms of single and multilayer graphene.* RSC advances, 2017. **7**(26): p. 15644-15693.
73. Li, X., et al., *Large-area synthesis of high-quality and uniform graphene films on copper foils.* science, 2009. **324**(5932): p. 1312-1314.
74. Hernandez, Y., et al., *High-yield production of graphene by liquid-phase exfoliation of graphite.* Nature nanotechnology, 2008. **3**(9): p. 563.
75. Novoselov, K.S., et al., *Electric field effect in atomically thin carbon films.* science, 2004. **306**(5696): p. 666-669.
76. Dreyer, D.R., et al., *The chemistry of graphene oxide.* Chemical society reviews, 2010. **39**(1): p. 228-240.
77. Berger, C., et al., *Electronic confinement and coherence in patterned epitaxial graphene.* Science, 2006. **312**(5777): p. 1191-1196.
78. Wang, X., et al., *Large-scale synthesis of few-layered graphene using CVD.* Chemical Vapor Deposition, 2009. **15**(1-3): p. 53-56.
79. Wang, Y., et al., *Large area, continuous, few-layered graphene as anodes in organic photovoltaic devices.* Applied Physics Letters, 2009. **95**(6): p. 209.
80. Dervishi, E., et al., *Large-scale graphene production by RF-cCVD method.* Chemical communications, 2009(27): p. 4061-4063.
81. Di, C.a., et al., *Patterned graphene as source/drain electrodes for bottom-contact organic field-effect transistors.* Advanced Materials, 2008. **20**(17): p. 3289-3293.
82. Chae, S.J., et al., *Synthesis of large-area graphene layers on poly-nickel substrate by chemical vapor deposition: wrinkle formation.* Advanced materials, 2009. **21**(22): p. 2328-2333.
83. Rollings, E., et al., *Synthesis and characterization of atomically thin graphite*

films on a silicon carbide substrate. Journal of Physics and Chemistry of Solids, 2006. **67**(9-10): p. 2172-2177.
84. De Heer, W.A., et al., *Epitaxial graphene.* Solid State Communications, 2007. **143**(1-2): p. 92-100.
85. Mattausch, A. and O. Pankratov, *Density functional study of graphene overlayers on SiC.* physica status solidi (b), 2008. **245**(7): p. 1425-1435.
86. Ni, Z., et al., *Raman spectroscopy of epitaxial graphene on a SiC substrate.* Physical Review B, 2008. **77**(11): p. 115416.
87. Sutter, P.W., J.-I. Flege, and E.A. Sutter, *Epitaxial graphene on ruthenium.* Nature materials, 2008. **7**(5): p. 406-411.
88. Seyller, T., et al., *Epitaxial graphene: a new material.* physica status solidi (b), 2008. **245**(7): p. 1436-1446.
89. Sprinkle, M., et al., *Epitaxial graphene: the material for graphene electronics.* physica status solidi (RRL)–Rapid Research Letters, 2009. **3**(6): p. A91-A94.
90. Kosynkin, D.V., et al., *Longitudinal unzipping of carbon nanotubes to form graphene nanoribbons.* Nature, 2009. **458**(7240): p. 872-876.
91. Jiao, L., et al., *Narrow graphene nanoribbons from carbon nanotubes.* Nature, 2009. **458**(7240): p. 877-880.
92. Hirsch, A., *Unzipping carbon nanotubes: a peeling method for the formation of graphene nanoribbons.* Angewandte Chemie International Edition, 2009. **48**(36): p. 6594-6596.
93. Kim, C.-D., B.-K. Min, and W.-S. Jung, *Preparation of graphene sheets by the reduction of carbon monoxide.* Carbon, 2009. **47**(6): p. 1610-1612.
94. Borovikov, V. and A. Zangwill, *Step-edge instability during epitaxial growth of graphene from SiC (0001).* Physical Review B, 2009. **80**(12): p. 121406.
95. Hass, J., W. De Heer, and E. Conrad, *The growth and morphology of epitaxial multilayer graphene.* Journal of Physics: Condensed Matter, 2008. **20**(32): p. 323202.
96. Hass, J., et al., *Highly ordered graphene for two dimensional electronics.* Applied Physics Letters, 2006. **89**(14): p. 143106.
97. Virojanadara, C., et al., *Homogeneous large-area graphene layer growth on 6 H-SiC (0001).* Physical Review B, 2008. **78**(24): p. 245403.
98. Emtsev, K.V., et al., *Towards wafer-size graphene layers by atmospheric pressure graphitization of silicon carbide.* Nature materials, 2009. **8**(3): p. 203-207.
99. Orlita, M., et al., *Approaching the Dirac point in high-mobility multilayer epitaxial graphene.* Physical review letters, 2008. **101**(26): p. 267601.
100. Miller, D.L., et al., *Observing the quantization of zero mass carriers in graphene.* Science, 2009. **324**(5929): p. 924-927.
101. Fuhrer, M.S., *Journal club.* Nature, 2009. **459**(7250): p. 1037-1037.
102. Pan, Y., et al., *Highly ordered, millimeter-scale, continuous, single-crystalline graphene monolayer formed on Ru (0001).* Advanced Materials, 2009. **21**(27): p. 2777-2780.
103. Coraux, J., et al., *Structure of epitaxial graphene on Ir (111).* New Journal of Physics, 2008. **10**(4): p. 043033.
104. Gao, L., J.R. Guest, and N.P. Guisinger, *Epitaxial graphene on Cu (111).* Nano letters, 2010. **10**(9): p. 3512-3516.
105. Gao, M., et al., *Epitaxial growth and structural property of graphene on Pt (111).* Applied Physics Letters, 2011. **98**(3): p. 033101.
106. Iwasaki, T., et al., *Long-range ordered single-crystal graphene on high-quality*

heteroepitaxial Ni thin films grown on MgO (111). Nano letters, 2011. **11**(1): p. 79-84.
107. Lee, J.-H., et al., *Wafer-scale growth of single-crystal monolayer graphene on reusable hydrogen-terminated germanium.* Science, 2014. **344**(6181): p. 286-289.
108. Nguyen, V.L., et al., *Seamless stitching of graphene domains on polished copper (111) foil.* Advanced Materials, 2015. **27**(8): p. 1376-1382.
109. Yang, W., et al., *Growth, characterization, and properties of nanographene.* Small, 2012. **8**(9): p. 1429-1435.
110. Hempel, M., et al., *A novel class of strain gauges based on layered percolative films of 2D materials.* Nano letters, 2012. **12**(11): p. 5714-5718.
111. Sutter, P., *How silicon leaves the scene.* Nature materials, 2009. **8**(3): p. 171-172.
112. Zhou, Y., et al., *Design, fabrication and characterization of a two-step released silicon dioxide piezoresistive microcantilever immunosensor.* Journal of Micromechanics and Microengineering, 2009. **19**(6): p. 065026.
113. Bae, S., et al., *Roll-to-roll production of 30-inch graphene films for transparent electrodes.* Nature nanotechnology, 2010. **5**(8): p. 574.
114. Kobayashi, T., et al., *Production of a 100-m-long high-quality graphene transparent conductive film by roll-to-roll chemical vapor deposition and transfer process.* Applied Physics Letters, 2013. **102**(2): p. 023112.
115. Somani, P.R., S.P. Somani, and M. Umeno, *Planer nano-graphenes from camphor by CVD.* Chemical Physics Letters, 2006. **430**(1-3): p. 56-59.
116. Muñoz, R. and C. Gómez-Aleixandre, *Review of CVD synthesis of graphene.* Chemical Vapor Deposition, 2013. **19**(10-11-12): p. 297-322.
117. Yu, Q., et al., *Graphene segregated on Ni surfaces and transferred to insulators.* Applied Physics Letters, 2008. **93**(11): p. 113103.
118. Cahn, R.W., *Binary Alloy Phase Diagrams–Second edition. TB Massalski, Editor-in-Chief; H. Okamoto, PR Subramanian, L. Kacprzak, Editors. ASM International, Materials Park, Ohio, USA. December 1990. xxii, 3589 pp., 3 vol., hard-back. $995.00 the set.* Advanced Materials, 1991. **3**(12): p. 628-629.
119. Yu, Q., et al., *Control and characterization of individual grains and grain boundaries in graphene grown by chemical vapour deposition.* Nature materials, 2011. **10**(6): p. 443.
120. Reina, A., et al., *Large area, few-layer graphene films on arbitrary substrates by chemical vapor deposition.* Nano letters, 2008. **9**(1): p. 30-35.
121. Song, H., et al., *Origin of the relatively low transport mobility of graphene grown through chemical vapor deposition.* Scientific reports, 2012. **2**: p. 337.
122. Yamaguchi, H., et al., *Highly uniform 300 mm wafer-scale deposition of single and multilayered chemically derived graphene thin films.* ACS nano, 2010. **4**(1): p. 524-528.
123. Kang, J., et al., *Graphene transfer: key for applications.* Nanoscale, 2012. **4**(18): p. 5527-5537.
124. Kim, K.S., et al., *Large-scale pattern growth of graphene films for stretchable transparent electrodes.* nature, 2009. **457**(7230): p. 706.
125. Clarson, S.J. and J.A. Semlyen, *Siloxane polymers*. 1993: Prentice Hall.
126. Lee, J.N., C. Park, and G.M. Whitesides, *Solvent compatibility of poly (dimethylsiloxane)-based microfluidic devices.* Analytical chemistry, 2003. **75**(23): p. 6544-6554.
127. Ambrosi, A. and M. Pumera, *The CVD graphene transfer procedure introduces*

metallic impurities which alter the graphene electrochemical properties. Nanoscale, 2014. **6**(1): p. 472-476.
128. Bai, L., et al., *Transfer method of crumpled graphene and its application for human strain monitoring.* Sensors and Actuators A: Physical, 2017. **260**: p. 153-160.
129. AZoNano. *CVD Graphene Films on Silicon and Silicon Dioxide*. 2015 [cited 2020 9 Jun]; Available from: https://www.azonano.com/article.aspx?ArticleID=4037.
130. Kang, S.J., et al., *Inking Elastomeric Stamps with Micro-Patterned, Single Layer Graphene to Create High-Performance OFETs.* Advanced Materials, 2011. **23**(31): p. 3531-3535.
131. Li, X., et al., *Transfer of large-area graphene films for high-performance transparent conductive electrodes.* Nano letters, 2009. **9**(12): p. 4359-4363.
132. Martinez, A., et al., *Optical deposition of graphene and carbon nanotubes in a fiber ferrule for passive mode-locked lasing.* Optics express, 2010. **18**(22): p. 23054-23061.
133. Huang, Y., et al., *Reliable exfoliation of large-area high-quality flakes of graphene and other two-dimensional materials.* ACS nano, 2015. **9**(11): p. 10612-10620.
134. Yi, M. and Z. Shen, *A review on mechanical exfoliation for the scalable production of graphene.* Journal of Materials Chemistry A, 2015. **3**(22): p. 11700-11715.
135. Bracamonte, M.V., et al., *On the nature of defects in liquid-phase exfoliated graphene.* The Journal of Physical Chemistry C, 2014. **118**(28): p. 15455-15459.
136. Flint, E.B. and K.S. Suslick, *The temperature of cavitation.* Science, 1991. **253**(5026): p. 1397-1399.
137. McNamara III, W.B., Y.T. Didenko, and K.S. Suslick, *Sonoluminescence temperatures during multi-bubble cavitation.* nature, 1999. **401**(6755): p. 772.
138. Polyakova, E.Y., et al., *Scanning tunneling microscopy and X-ray photoelectron spectroscopy studies of graphene films prepared by sonication-assisted dispersion.* ACS nano, 2011. **5**(8): p. 6102-6108.
139. Skaltsas, T., et al., *Ultrasonication induces oxygenated species and defects onto exfoliated graphene.* The Journal of Physical Chemistry C, 2013. **117**(44): p. 23272-23278.
140. Suslick, K.S. and D.J. Flannigan, *Inside a collapsing bubble: sonoluminescence and the conditions during cavitation.* Annu. Rev. Phys. Chem., 2008. **59**: p. 659-683.
141. Yi, M., et al., *Water can stably disperse liquid-exfoliated graphene.* Chemical Communications, 2013. **49**(94): p. 11059-11061.
142. Zhao, W., et al., *Preparation of graphene by exfoliation of graphite using wet ball milling.* Journal of materials chemistry, 2010. **20**(28): p. 5817-5819.
143. Aparna, R., et al., *An effective route to produce few-layer graphene using combinatorial ball milling and strong aqueous exfoliants.* Journal of Renewable and Sustainable Energy, 2013. **5**(3): p. 033123.
144. Borah, M., et al., *Few Layer Graphene Derived from Wet Ball Milling of Expanded Graphite and Few Layer Graphene Based Polymer Composite.* Materials Focus, 2014. **3**(4): p. 300-309.
145. Leon, V., et al., *Exfoliation of graphite with triazine derivatives under ball-milling conditions: preparation of few-layer graphene via selective noncovalent interactions.* ACS nano, 2014. **8**(1): p. 563-571.

146. Lv, Y., et al., *Synthesis of graphene nanosheet powder with layer number control via a soluble salt-assisted route.* RSC Advances, 2014. **4**(26): p. 13350-13354.
147. Posudievsky, O.Y., et al., *High yield of graphene by dispersant-free liquid exfoliation of mechanochemically delaminated graphite.* Journal of nanoparticle research, 2013. **15**(11): p. 2046.
148. Hummers Jr, W.S. and R.E. Offeman, *Preparation of graphitic oxide.* Journal of the american chemical society, 1958. **80**(6): p. 1339-1339.
149. Rosli, N.N., et al., *A review of graphene based transparent conducting films for use in solar photovoltaic applications.* Renewable and Sustainable Energy Reviews, 2019. **99**: p. 83-99.
150. Becerril, H.A., et al., *Evaluation of solution-processed reduced graphene oxide films as transparent conductors.* ACS nano, 2008. **2**(3): p. 463-470.
151. Wu, J., et al., *Organic solar cells with solution-processed graphene transparent electrodes.* Applied physics letters, 2008. **92**(26): p. 237.
152. Pham, V.H., et al., *One-step synthesis of superior dispersion of chemically converted graphene in organic solvents.* Chemical Communications, 2010. **46**(24): p. 4375-4377.
153. Zhou, X., et al., *Reducing graphene oxide via hydroxylamine: a simple and efficient route to graphene.* The Journal of Physical Chemistry C, 2011. **115**(24): p. 11957-11961.
154. Zhu, C., et al., *Reducing sugar: new functional molecules for the green synthesis of graphene nanosheets.* ACS nano, 2010. **4**(4): p. 2429-2437.
155. Zhang, J., et al., *Reduction of graphene oxide via L-ascorbic acid.* Chemical Communications, 2010. **46**(7): p. 1112-1114.
156. Wang, G., et al., *Facile synthesis and characterization of graphene nanosheets.* The Journal of Physical Chemistry C, 2008. **112**(22): p. 8192-8195.
157. Fan, X., et al., *Deoxygenation of exfoliated graphite oxide under alkaline conditions: a green route to graphene preparation.* Advanced Materials, 2008. **20**(23): p. 4490-4493.
158. Amarnath, C.A., et al., *Efficient synthesis of graphene sheets using pyrrole as a reducing agent.* Carbon, 2011. **49**(11): p. 3497-3502.
159. Dubin, S., et al., *A one-step, solvothermal reduction method for producing reduced graphene oxide dispersions in organic solvents.* ACS nano, 2010. **4**(7): p. 3845-3852.
160. Compton, O.C., et al., *Chemically active reduced graphene oxide with tunable C/O ratios.* ACS nano, 2011. **5**(6): p. 4380-4391.
161. Guo, H.-L., et al., *A green approach to the synthesis of graphene nanosheets.* ACS nano, 2009. **3**(9): p. 2653-2659.
162. Sundaram, R.S., et al., *Electrochemical modification of graphene.* Advanced Materials, 2008. **20**(16): p. 3050-3053.
163. Manjunath, M., et al., *Design, fabrication and testing of reduced graphene oxide strain gauge based pressure sensor with increased sensitivity.* Microsystem Technologies, 2018. **24**(7): p. 2969-2981.
164. Grodecki, K., et al., *SEM and Raman analysis of graphene on SiC (0001).* Micron, 2016. **80**: p. 20-23.
165. Ferrari, A.C., *Raman spectroscopy of graphene and graphite: disorder, electron–phonon coupling, doping and nonadiabatic effects.* Solid state communications, 2007. **143**(1-2): p. 47-57.
166. Ferrari, A.C., et al., *Raman spectrum of graphene and graphene layers.* Physical

review letters, 2006. **97**(18): p. 187401.
167. Malard, L., et al., *Raman spectroscopy in graphene.* Physics reports, 2009. **473**(5-6): p. 51-87.
168. Wall, M., *The Raman spectroscopy of graphene and the determination of layer thickness.* Thermo Sci, 2011. **5**.
169. Peng, H., Q. Li, and T. Chen, *Industrial applications of carbon nanotubes*. 2016: William Andrew.
170. Scientific, H. *Raman Spectroscopy of Graphene*. 24 September 2019; Available from: https://www.azom.com/article.aspx?ArticleID=10130.
171. Ni, Z.H., et al., *Tunable stress and controlled thickness modification in graphene by annealing.* ACS nano, 2008. **2**(5): p. 1033-1039.
172. AZoM. *Characterization of Graphene Using Raman Spectroscopy*. 2012 [cited 2020 9 Jun]; Available from: https://www.azom.com/article.aspx?ArticleID=6271.
173. Hosseinzadeh, A., et al., *Graphene based strain sensors: A comparative study on graphene and its derivatives.* Applied Surface Science, 2018. **448**: p. 71-77.
174. Elias, D.C., et al., *Control of graphene's properties by reversible hydrogenation: evidence for graphane.* Science, 2009. **323**(5914): p. 610-613.
175. Kim, Y.-R., et al., *Electrochemical detection of dopamine in the presence of ascorbic acid using graphene modified electrodes.* Biosensors and Bioelectronics, 2010. **25**(10): p. 2366-2369.
176. Zhao, J., et al., *Ultra-sensitive strain sensors based on piezoresistive nanographene films.* Applied Physics Letters, 2012. **101**(6): p. 063112.
177. Bae, S.-H., et al., *Graphene-based transparent strain sensor.* Carbon, 2013. **51**: p. 236-242.
178. Boland, C.S., et al., *Sensitive, high-strain, high-rate bodily motion sensors based on graphene–rubber composites.* ACS nano, 2014. **8**(9): p. 8819-8830.
179. Lin, Y., et al., *Graphene–elastomer composites with segregated nanostructured network for liquid and strain sensing application.* ACS applied materials & interfaces, 2016. **8**(36): p. 24143-24151.
180. Coskun, M.B., et al., *Ultrasensitive strain sensor produced by direct patterning of liquid crystals of graphene oxide on a flexible substrate.* ACS applied materials & interfaces, 2016. **8**(34): p. 22501-22505.
181. Fu, X.-W., et al., *Strain dependent resistance in chemical vapor deposition grown graphene.* Applied Physics Letters, 2011. **99**(21): p. 213107.
182. Gamil, M., et al., *Graphene-based strain gauge on a flexible substrate.* Sensors and Materials, 2014. **26**(9): p. 699-709.
183. Tian, H., et al., *A graphene-based resistive pressure sensor with record-high sensitivity in a wide pressure range.* Scientific reports, 2015. **5**: p. 8603.
184. Neella, N., et al. *Negative temperature coefficient behavior of graphene-silver nanocomposite films for temperature sensor applications*. in *2016 IEEE 11th Annual International Conference on Nano/Micro Engineered and Molecular Systems (NEMS)*. 2016. IEEE.
185. Neella, N., et al. *Highly flexible and sensitive graphene-silver nanocomposite strain sensor*. in *2015 IEEE SENSORS*. 2015. IEEE.
186. Qin, Y., et al., *Lightweight, superelastic, and mechanically flexible graphene/polyimide nanocomposite foam for strain sensor application.* ACS nano, 2015. **9**(9): p. 8933-8941.
187. Saha, B., S. Baek, and J. Lee, *Highly sensitive bendable and foldable paper sensors based on reduced graphene oxide.* ACS applied materials & interfaces,

2017. **9**(5): p. 4658-4666.
188. Yan, C., et al., *Highly stretchable piezoresistive graphene–nanocellulose nanopaper for strain sensors.* Advanced materials, 2014. **26**(13): p. 2022-2027.
189. Wang, Y., et al., *Super-elastic graphene ripples for flexible strain sensors.* ACS nano, 2011. **5**(5): p. 3645-3650.
190. Huang, M., et al., *Electronic− mechanical coupling in graphene from in situ nanoindentation experiments and multiscale atomistic simulations.* Nano letters, 2011. **11**(3): p. 1241-1246.
191. Park, J.J., et al., *Highly stretchable and wearable graphene strain sensors with controllable sensitivity for human motion monitoring.* ACS applied materials & interfaces, 2015. **7**(11): p. 6317-6324.
192. Jeong, Y.R., et al., *Highly stretchable and sensitive strain sensors using fragmentized graphene foam.* Advanced Functional Materials, 2015. **25**(27): p. 4228-4236.
193. Lee, C., L. Jug, and E. Meng, *High strain biocompatible polydimethylsiloxane-based conductive graphene and multiwalled carbon nanotube nanocomposite strain sensors.* Applied Physics Letters, 2013. **102**(18): p. 183511.
194. Eswaraiah, V., K. Balasubramaniam, and S. Ramaprabhu, *One-pot synthesis of conducting graphene–polymer composites and their strain sensing application.* Nanoscale, 2012. **4**(4): p. 1258-1262.
195. Park, Y.J., et al., *Graphene-based conformal devices.* ACS nano, 2014. **8**(8): p. 7655-7662.
196. Zhu, B., et al., *Microstructured graphene arrays for highly sensitive flexible tactile sensors.* Small, 2014. **10**(18): p. 3625-3631.
197. Chun, S., et al., *A highly sensitive pressure sensor using a double-layered graphene structure for tactile sensing.* Nanoscale, 2015. **7**(27): p. 11652-11659.
198. Chun, S., et al., *A tactile sensor using a graphene film formed by the reduced graphene oxide flakes and its detection of surface morphology.* Carbon, 2015. **94**: p. 982-987.
199. Sun, Q., et al., *Active matrix electronic skin strain sensor based on piezopotential-powered graphene transistors.* Advanced Materials, 2015. **27**(22): p. 3411-3417.
200. Wu, S., S. Peng, and C.H. Wang, *Stretchable strain sensors based on PDMS composites with cellulose sponges containing one-and two-dimensional nanocarbons.* Sensors and Actuators A: Physical, 2018. **279**: p. 90-100.
201. Chen, S., et al., *Ultrasensitive cracking-assisted strain sensors based on silver nanowires/graphene hybrid particles.* ACS applied materials & interfaces, 2016. **8**(38): p. 25563-25570.
202. Luo, S. and T. Liu, *SWCNT/Graphite nanoplatelet hybrid thin films for self-temperature-compensated, highly sensitive, and extensible piezoresistive sensors.* Advanced materials, 2013. **25**(39): p. 5650-5657.
203. Eswaraiah, V., et al., *Graphene-Functionalized Carbon Nanotubes for Conducting Polymer Nanocomposites and Their Improved Strain Sensing Properties.* Macromolecular Chemistry and Physics, 2013. **214**(21): p. 2439-2444.
204. Zhao, H. and J. Bai, *Highly sensitive piezo-resistive graphite nanoplatelet–carbon nanotube hybrids/polydimethylsilicone composites with improved conductive network construction.* ACS applied materials & interfaces, 2015. **7**(18): p. 9652-9659.
205. Chen, M., et al., *Highly stretchable conductors integrated with a conductive*

carbon nanotube/graphene network and 3D porous poly (dimethylsiloxane). Advanced Functional Materials, 2014. **24**(47): p. 7548-7556.
206. Shi, J., et al., *Graphene reinforced carbon nanotube networks for wearable strain sensors.* Advanced Functional Materials, 2016. **26**(13): p. 2078-2084.
207. Liu, H., et al., *Electrically conductive strain sensing polyurethane nanocomposites with synergistic carbon nanotubes and graphene bifillers.* Nanoscale, 2016. **8**(26): p. 12977-12989.
208. Hwang, S.-H., H.W. Park, and Y.-B. Park, *Piezoresistive behavior and multi-directional strain sensing ability of carbon nanotube–graphene nanoplatelet hybrid sheets.* Smart materials and structures, 2012. **22**(1): p. 015013.
209. Liu, Q., et al., *High-performance strain sensors with fish-scale-like graphene-sensing layers for full-range detection of human motions.* ACS nano, 2016. **10**(8): p. 7901-7906.
210. Trung, T.Q., et al., *A flexible reduced graphene oxide field-effect transistor for ultrasensitive strain sensing.* Advanced Functional Materials, 2014. **24**(1): p. 117-124.
211. Liu, X., et al., *A highly sensitive graphene woven fabric strain sensor for wearable wireless musical instruments.* Materials Horizons, 2017. **4**(3): p. 477-486.
212. Tang, Y., et al., *Highly stretchable and ultrasensitive strain sensor based on reduced graphene oxide microtubes–elastomer composite.* ACS applied materials & interfaces, 2015. **7**(49): p. 27432-27439.
213. Casiraghi, C., et al., *Inkjet printed 2D-crystal based strain gauges on paper.* Carbon, 2018. **129**: p. 462-467.
214. Zhao, J., et al., *Tunable piezoresistivity of nanographene films for strain sensing.* ACS nano, 2015. **9**(2): p. 1622-1629.
215. Chun, S., Y. Choi, and W. Park, *All-graphene strain sensor on soft substrate.* Carbon, 2017. **116**: p. 753-759.
216. Gong, T., et al., *Highly responsive flexible strain sensor using polystyrene nanoparticle doped reduced graphene oxide for human health monitoring.* Carbon, 2018. **140**: p. 286-295.
217. Mayorov, A.S., et al., *Micrometer-scale ballistic transport in encapsulated graphene at room temperature.* Nano letters, 2011. **11**(6): p. 2396-2399.
218. Elias, D., et al., *Dirac cones reshaped by interaction effects in suspended graphene.* Nature Physics, 2011. **7**(9): p. 701-704.
219. Gan, T. and S. Hu, *Electrochemical sensors based on graphene materials.* Microchimica Acta, 2011. **175**(1-2): p. 1.
220. Sheng, Z.-H., et al., *Electrochemical sensor based on nitrogen doped graphene: simultaneous determination of ascorbic acid, dopamine and uric acid.* Biosensors and Bioelectronics, 2012. **34**(1): p. 125-131.
221. Wang, C., et al., *A novel hydrazine electrochemical sensor based on the high specific surface area graphene.* Microchimica Acta, 2010. **169**(1-2): p. 1-6.
222. Wang, Z., et al., *An ionic liquid-modified graphene based molecular imprinting electrochemical sensor for sensitive detection of bovine hemoglobin.* Biosensors and Bioelectronics, 2014. **61**: p. 391-396.
223. Wang, K., et al., *Ultrasensitive photoelectrochemical sensing of nicotinamide adenine dinucleotide based on graphene-TiO2 nanohybrids under visible irradiation.* Analytica chimica acta, 2012. **745**: p. 131-136.
224. Sun, C.-L., et al., *The simultaneous electrochemical detection of ascorbic acid, dopamine, and uric acid using graphene/size-selected Pt nanocomposites.*

Biosensors and Bioelectronics, 2011. **26**(8): p. 3450-3455.
225. Zhan, B., et al., *Graphene field-effect transistor and its application for electronic sensing.* Small, 2014. **10**(20): p. 4042-4065.
226. Nag, A., A. Mitra, and S.C. Mukhopadhyay, *Graphene and its sensor-based applications: A review.* Sensors and Actuators A: Physical, 2018. **270**: p. 177-194.
227. Tian, H., et al., *Scalable fabrication of high-performance and flexible graphene strain sensors.* Nanoscale, 2014. **6**(2): p. 699-705.
228. Li, X., et al., *Stretchable and highly sensitive graphene-on-polymer strain sensors.* Scientific reports, 2012. **2**: p. 870.
229. Li, X., et al., *Multifunctional graphene woven fabrics.* Scientific reports, 2012. **2**: p. 395.
230. Jang, H., et al., *Graphene-based flexible and stretchable electronics.* Advanced Materials, 2016. **28**(22): p. 4184-4202.
231. Lee, Y., et al., *Wafer-scale synthesis and transfer of graphene films.* Nano letters, 2010. **10**(2): p. 490-493.
232. Gong, S., et al., *Highly Stretchy Black Gold E-Skin Nanopatches as Highly Sensitive Wearable Biomedical Sensors.* Advanced Electronic Materials, 2015. **1**(4): p. 1400063.
233. Hwang, B.-U., et al., *Transparent stretchable self-powered patchable sensor platform with ultrasensitive recognition of human activities.* ACS nano, 2015. **9**(9): p. 8801-8810.
234. Xiao, X., et al., *High-strain sensors based on ZnO nanowire/polystyrene hybridized flexible films.* Advanced materials, 2011. **23**(45): p. 5440-5444.
235. Majumder, S., T. Mondal, and M.J. Deen, *Wearable sensors for remote health monitoring.* Sensors, 2017. **17**(1): p. 130.
236. Dementyev, A., et al. *Power consumption analysis of Bluetooth Low Energy, ZigBee and ANT sensor nodes in a cyclic sleep scenario*. in *2013 IEEE International Wireless Symposium (IWS)*. 2013. IEEE.
237. Laine, T.H., C. Lee, and H. Suk. *Mobile gateway for ubiquitous health care system using zigbee and bluetooth*. in *2014 Eighth International Conference on Innovative Mobile and Internet Services in Ubiquitous Computing*. 2014. IEEE.
238. Tröster, G., *The agenda of wearable healthcare.* Yearbook of medical informatics, 2005. **14**(01): p. 125-138.
239. Liu, C., *Foundations of MEMS*. 2012: Pearson Education India.
240. Singh, P., et al., *Biomedical perspective of electrochemical nanobiosensor.* Nano-micro letters, 2016. **8**(3): p. 193-203.
241. He, W., et al., *Polypyrrole/silver coaxial nanowire aero-sponges for temperature-independent stress sensing and stress-triggered joule heating.* Acs Nano, 2015. **9**(4): p. 4244-4251.
242. Sirelkhatim, A., et al., *Review on zinc oxide nanoparticles: antibacterial activity and toxicity mechanism.* Nano-micro letters, 2015. **7**(3): p. 219-242.
243. Yin, J., V.J. Santos, and J.D. Posner, *Bioinspired flexible microfluidic shear force sensor skin.* Sensors and Actuators A: Physical, 2017. **264**: p. 289-297.
244. Kumar, R., et al., *Zinc oxide nanostructures for NO 2 gas–sensor applications: A review.* Nano-Micro Letters, 2015. **7**(2): p. 97-120.
245. Wang, A., et al., *Recent advances of graphitic carbon nitride-based structures and applications in catalyst, sensing, imaging, and LEDs.* Nano-micro letters, 2017. **9**(4): p. 1-21.
246. Stassi, S., et al., *Polymeric 3D printed functional microcantilevers for*

biosensing applications. ACS applied materials & interfaces, 2017. **9**(22): p. 19193-19201.
247. Wen, Z., Q. Shen, and X. Sun, *Nanogenerators for self-powered gas sensing.* Nano-micro letters, 2017. **9**(4): p. 45.
248. Zhang, J., et al., *Low-dimensional halide perovskites and their advanced optoelectronic applications.* Nano-micro letters, 2017. **9**(3): p. 1-26.
249. Thuau, D., et al., *Advanced thermo-mechanical characterization of organic materials by piezoresistive organic resonators.* Materials Horizons, 2015. **2**(1): p. 106-112.
250. Zhu, Z., *An overview of carbon nanotubes and graphene for biosensing applications.* Nano-micro letters, 2017. **9**(3): p. 1-24.
251. Arlett, J., E. Myers, and M. Roukes, *Comparative advantages of mechanical biosensors.* Nature nanotechnology, 2011. **6**(4): p. 203-215.
252. Lang, H.P., et al., *An artificial nose based on a micromechanical cantilever array.* Analytica Chimica Acta, 1999. **393**(1-3): p. 59-65.
253. Xu, S. and R. Mutharasan, *Rapid and sensitive detection of Giardia lamblia using a piezoelectric cantilever biosensor in finished and source waters.* Environmental science & technology, 2010. **44**(5): p. 1736-1741.
254. Huang, L.-S., et al., *Detection of the antiepileptic drug phenytoin using a single free-standing piezoresistive microcantilever for therapeutic drug monitoring.* Biosensors and Bioelectronics, 2014. **59**: p. 233-238.
255. Arcamone, J., et al., *Micro/nanomechanical resonators for distributed mass sensing with capacitive detection.* Microelectronic Engineering, 2006. **83**(4-9): p. 1216-1220.
256. Loui, A., et al., *The effect of piezoresistive microcantilever geometry on cantilever sensitivity during surface stress chemical sensing.* Sensors and Actuators A: Physical, 2008. **147**(2): p. 516-521.
257. Fernandez, R.E., et al., *MEMS composite porous silicon/polysilicon cantilever sensor for enhanced triglycerides biosensing.* IEEE Sensors Journal, 2009. **9**(12): p. 1660-1666.
258. Yang, R., et al., *A chemisorption-based microcantilever chemical sensor for the detection of trimethylamine.* Sensors and actuators B: chemical, 2010. **145**(1): p. 474-479.
259. Pandya, H., et al., *MEMS based low cost piezoresistive microcantilever force sensor and sensor module.* Materials science in semiconductor processing, 2014. **19**: p. 163-173.
260. Yang, Y., et al., *Quad-cantilever microsensors with a low-cost single-sided micro-machining technique for trace chemical vapor detection.* Microelectronic engineering, 2010. **87**(11): p. 2317-2322.
261. Yang, S.-M., T. Yin, and C. Chang, *A biosensor chip by CMOS process for surface stress measurement in bioanalyte.* Sensors and Actuators B: Chemical, 2007. **123**(2): p. 707-714.
262. Harkey, J. and T.W. Kenny, *1/f noise considerations for the design and process optimization of piezoresistive cantilevers.* Journal of microelectromechanical systems, 2000. **9**(2): p. 226-235.
263. Lakhmi, R., et al., *Force sensors based on screen-printed cantilevers.* IEEE Sensors Journal, 2010. **10**(6): p. 1133-1137.
264. Katragadda, R., et al., *Parylene cantilevers integrated with polycrystalline silicon piezoresistors for surface stress sensing.* Applied Physics Letters, 2007. **91**(8): p. 083505.

265. Alpuim, P., V. Chu, and J.P. Conde, *Piezoresistive sensors on plastic substrates using doped microcrystalline silicon.* IEEE sensors journal, 2002. **2**(4): p. 336-341.
266. Li, X. and D.-W. Lee, *Integrated microcantilevers for high-resolution sensing and probing.* Measurement Science and Technology, 2011. **23**(2): p. 022001.
267. Calleja, M., et al., *Challenges for nanomechanical sensors in biological detection.* Nanoscale, 2012. **4**(16): p. 4925-4938.
268. Moulin, A., S. O'shea, and M.E. Welland, *Microcantilever-based biosensors.* Ultramicroscopy, 2000. **82**(1-4): p. 23-31.
269. Boisen, A., et al., *Cantilever-like micromechanical sensors.* Reports on Progress in Physics, 2011. **74**(3): p. 036101.
270. Goeders, K.M., J.S. Colton, and L.A. Bottomley, *Microcantilevers: sensing chemical interactions via mechanical motion.* Chemical reviews, 2008. **108**(2): p. 522-542.
271. Buchapudi, K.R., et al., *Microcantilever biosensors for chemicals and bioorganisms.* Analyst, 2011. **136**(8): p. 1539-1556.
272. Kim, B.J. and E. Meng, *Review of polymer MEMS micromachining.* Journal of Micromechanics and Microengineering, 2015. **26**(1): p. 013001.
273. Liu, C., *Recent developments in polymer MEMS.* Advanced Materials, 2007. **19**(22): p. 3783-3790.
274. Seena, V., et al., *Polymer MEMS sensors.* Advanced Biomaterials and Biodevices, 2014: p. 305-342.
275. Nordström, M., et al., *SU-8 cantilevers for bio/chemical sensing; fabrication, characterisation and development of novel read-out methods.* Sensors, 2008. **8**(3): p. 1595-1612.
276. Mathew, R. and A.R. Sankar, *A review on surface stress-based miniaturized piezoresistive SU-8 polymeric cantilever sensors.* Nano-micro letters, 2018. **10**(2): p. 35.
277. Wasisto, H., et al., *Silicon Nanowire Resonators: Aerosol Nanoparticle Mass Sensing in the Workplace.* IEEE Nanotechnology Magazine, 2013. **7**(2): p. 18-23.
278. Wasisto, H.S., et al., *Silicon resonant nanopillar sensors for airborne titanium dioxide engineered nanoparticle mass detection.* Sensors and Actuators, B: Chemical, 2013. **189**.
279. Merzsch, S., et al., *Production of vertical nanowire resonators by cryogenic-ICP–DRIE.* Micro- and Nanosystems Information Storage and Processing Systems, 2014. **20**(4): p. 759-767.
280. Wasisto, H., et al., *Finite element modeling and experimental proof of NEMS-based silicon pillar resonators for nanoparticle mass sensing applications.* Micro- and Nanosystems Information Storage and Processing Systems, 2014. **20**(4): p. 571-584.
281. Wasisto, H.S., et al., *Evaluation of photoresist-based nanoparticle removal method for recycling silicon cantilever mass sensors.* Sensors and Actuators, A: Physical, 2013. **202**.
282. Wasisto, H.S., et al., *Airborne engineered nanoparticle mass sensor based on a silicon resonant cantilever.* Sensors & Actuators: B. Chemical, 2013. **180**: p. 77-89.
283. Wasisto, H., et al., *A phase-locked loop frequency tracking system for portable microelectromechanical piezoresistive cantilever mass sensors.* Micro- and Nanosystems Information Storage and Processing Systems, 2014. **20**(4): p. 559-

569.
284. Wasisto, H.S., et al., *Partially integrated cantilever-based airborne nanoparticle detector for continuous carbon aerosol mass concentration monitoring.* Journal of sensors and sensor systems, 2015. **4**(1): p. 111-123.
285. Wasisto, H.S., et al., *Handheld personal airborne nanoparticle detector based on microelectromechanical silicon resonant cantilever.(Report).* Microelectronic Engineering, 2015. **145**: p. 96.
286. Keller, S., D. Haefliger, and A. Boisen, *Fabrication of thin su-8 cantilevers: initial bending, release and time stability.* Journal of Micromechanics and Microengineering, 2010. **20**(4): p. 045024.
287. Seena, V., et al., *Polymer nanocomposite nanomechanical cantilever sensors: material characterization, device development and application in explosive vapour detection.* Nanotechnology, 2011. **22**(29): p. 295501.
288. Johansson, A., et al., *SU-8 cantilever sensor system with integrated readout.* Sensors & Actuators: A. Physical, 2005. **123**: p. 111-115.
289. Binnig, G., C.F. Quate, and C. Gerber, *Atomic force microscope.* Physical Review Letters, 1986. **56**(9): p. 930-933.
290. Binnig, G., *Atomic resolution with atomic force microscope.* EPL (Europhysics Letters), 1987. **3**(12): p. 1281-1286.
291. Tortonese, M., et al., *Atomic force microscopy using a piezoresistive cantilever*. 1991. p. 448-451.
292. Kim, S.-J., T. Ono, and M. Esashi, *Capacitive resonant mass sensor with frequency demodulation detection based on resonant circuit.* Applied Physics Letters, 2006. **88**(5).
293. Lee, J.H., et al., *Immunoassay of prostate-specific antigen (PSA) using resonant frequency shift of piezoelectric nanomechanical microcantilever.* Biosensors and Bioelectronics, 2005. **20**(10): p. 2157-2162.
294. Scheible, D.V., A. Erbe, and R.H. Blick, *Tunable coupled nanomechanical resonators for single-electron transport.* New J. Phys., 2002. **4**.
295. Nordström, M., et al., *Integrated optical readout for miniaturization of cantilever-based sensor system.* Applied Physics Letters, 2007. **91**(10).
296. Komati, B., et al., *Prototyping of a highly performant and integrated piezoresistive force sensor for microscale applications.* Journal of Micromechanics and Microengineering, 2014. **24**(3): p. 035018.
297. Tosolini, G., et al., *Silicon microcantilevers with MOSFET detection.* Microelectronic Engineering, 2010. **87**(5-8): p. 1245-1247.
298. Sung-Jin, P., et al., *Piezoresistive Cantilever Performance-Part II: Optimization.* Journal of Microelectromechanical Systems, 2010. **19**(1): p. 149-161.
299. Sung-Jin, P., J.C. Doll, and B.L. Pruitt, *Piezoresistive Cantilever Performance-Part I: Analytical Model for Sensitivity.* Journal of Microelectromechanical Systems, 2010. **19**(1): p. 137-148.
300. Doll, J.C., S.-J. Park, and B.L. Pruitt, *Design optimization of piezoresistive cantilevers for force sensing in air and water.* Journal of Applied Physics, 2009. **106**(6).
301. Villanueva, G., et al., *Crystalline silicon cantilevers for piezoresistive detection of biomolecular forces.* Microelectronic Engineering, 2008. **85**(5-6): p. 1120-1123.
302. Cheney, C.P., et al., *In vivo wireless ethanol vapor detection in the Wistar rat.* Sensors & Actuators: B. Chemical, 2009. **138**(1): p. 264-269.
303. Venkatasubramanian, A., et al., *MOF @ MEMS: Design optimization for high*

sensitivity chemical detection. Sensors & Actuators: B. Chemical, 2012. **168**: p. 256-262.
304. Rasmussen, P.A., et al., *Optimised cantilever biosensor with piezoresistive read-out.* Ultramicroscopy, 2003. **97**(1-4): p. 371-376.
305. Hyun, S.-J., et al., *Mechanical detection of liposomes using piezoresistive cantilever.* Sensors & Actuators: B. Chemical, 2006. **117**(2): p. 415-419.
306. Ansari, M.Z. and C. Cho, *On self-heating in piezoresistive microcantilevers with short piezoresistor.* Journal of Physics D: Applied Physics, 2011. **44**(28): p. 285402.
307. Chen, Y., et al., *Bio/chemical detection in liquid with self-sensing Pr-Oxi-Lever (piezo-resistive SiO 2 cantilever) sensors.* Microelectronic Engineering, 2010. **87**(12): p. 2468-2474.
308. Huang, C.-W., et al., *A fully integrated wireless CMOS microcantilever lab chip for detection of DNA from Hepatitis B virus (HBV).* Sensors & Actuators: B. Chemical, 2013. **181**: p. 867-873.
309. Yang, S.M., et al., *DNA hybridization measurement by self-sensing piezoresistive microcantilevers in CMOS biosensor.* Sensors & Actuators: B. Chemical, 2008. **130**(2): p. 674-681.
310. Yang, S.M. and T.I. Yin, *Design and analysis of piezoresistive microcantilever for surface stress measurement in biochemical sensor.* Sensors & Actuators: B. Chemical, 2007. **120**(2): p. 736-744.
311. Zuo, G., et al., *Detection of trace organophosphorus vapor with a self-assembled bilayer functionalized SiO 2 microcantilever piezoresistive sensor.* Analytica chimica acta, 2006. **580**(2): p. 123-127.
312. Ansari, M.Z. and C. Cho, *A conduction–convection model for self-heating in piezoresistive microcantilever biosensors.* Sensors & Actuators: A. Physical, 2012. **175**: p. 19-27.
313. Yao, T., X. Yang, and Y. Tai, *BrF3 dry release technology for large freestanding parylene microstructures and electrostatic actuators.* Sens. Actuator A-Phys., 2002. **97-8**: p. 771-775.
314. McFarland, A.W. and J.S. Colton, *Chemical sensing with micromolded plastic microcantilevers.* Journal of Microelectromechanical Systems, 2005. **14**(6): p. 1375-1385.
315. Lee, L.P., et al., *High aspect ratio polymer microstructures and cantilevers for bioMEMS using low energy ion beam and photolithography.* Sensors & Actuators: A. Physical, 1998. **71**(1-2): p. 144-149.
316. Calleja, M., et al., *Low-noise polymeric nanomechanical biosensors.* Applied Physics Letters, 2006. **88**(11).
317. Zhang, X.R. and X. Xu, *Development of a biosensor based on laser-fabricatedpolymer microcantilevers.* Applied Physics Letters, 2004. **85**(12): p. 2423-2425.
318. Gaitas, A. and Y.B. Gianchandani, *An experimental study of the contact mode AFM scanning capability of polyimide cantilever probes.* Ultramicroscopy, 2006. **106**(8-9): p. 874-880.
319. Greve, A., et al., *Thermoplastic microcantilevers fabricated by nanoimprint lithography.* Journal of Micromechanics and Microengineering, 2010. **20**(1): p. 015009.
320. Andrew, W.M., *Injection moulding of high aspect ratio micron-scale thickness polymeric microcantilevers.* Nanotechnology, 2004. **15**(11): p. 1628-1632.
321. Firpo, G., et al., *Permeability thickness dependence of polydimethylsiloxane*

(PDMS) membranes. Journal of Membrane Science, 2015. **481**: p. 1-8.
322. Zhu, R., et al., *Microstructure and mechanical properties of polypropylene/poly(methyl methacrylate) nanocomposite prepared using supercritical carbon dioxide.* Macromolecules, 2011. **44**(15): p. 6103-6112.
323. Seena, V., et al., *Polymer microcantilever biochemical sensors with integrated polymer composites for electrical detection.* Solid State Sciences, 2009. **11**(9): p. 1606-1611.
324. Ray, P., S. Pandey, and V. Ramgopal Rao, *Development of graphene nanoplatelet embedded polymer microcantilever for vapour phase explosive detection applications.* Journal of Applied Physics, 2014. **116**(12).
325. Joshi, M., et al., *Modeling, Simulation, and Design Guidelines for Piezoresistive Affinity Cantilevers.* Journal of Microelectromechanical Systems, 2011. **20**(3): p. 774-784.
326. Mathew, R. and A. Ravi Sankar, *Design of a triangular platform piezoresistive affinity microcantilever sensor for biochemical sensing applications.* Journal of Physics D: Applied Physics, 2015. **48**(20).
327. Bashir, R., *On the design of piezoresistive silicon cantilevers with stress concentration regions for scanning probe microscopy applications.* Journal of Micromechanics and Microengineering, 2000. **10**(4): p. 483-491.
328. Mishra, N., et al., *Evaluation of Effective Elastic, Piezoelectric, and Dielectric Properties of SU8/ZnO Nanocomposite for Vertically Integrated Nanogenerators Using Finite Element Method.* Journal of Nanomaterials, 2017. **2017**.
329. Lim, Y., et al., *A protocol for improving fabrication yield of thin SU-8 microcantilevers for use in an aptasensor.* Micro- and Nanosystems Information Storage and Processing Systems, 2015. **21**(2): p. 371-380.
330. Mao, Z., K. Yoshida, and J.-w. Kim, *Study on the fabrication of a SU-8 cantilever vertically-allocated in a closed fluidic microchannel.* Micro- and Nanosystems Information Storage and Processing Systems, 2018. **24**(5): p. 2473-2483.
331. Gerardo, C.D., E. Cretu, and R. Rohling, *Fabrication of Circuits on Flexible Substrates Using Conductive SU-8 for Sensing Applications.* Sensors, 2017. **17**(6).
332. Ge, C. and E. Cretu, *Mems transducers low-cost fabrication using su-8 in a sacrificial layer-free process.* Journal of Micromechanics and Microengineering, 2017. **27**(4): p. 045002.
333. Nayak, S., et al., *Flexible polymer-multiwall carbon nanotubes composite developed by in situ polymerization technique.* Polymer Composites, 2016. **37**(9): p. 2860-2870.
334. Tiwary, N., et al., *Fabrication, Characterization and Application of ZnO Nanostructure-Based Micro-Preconcentrator for TNT Sensing.* Journal of Microelectromechanical Systems, 2016. **25**(5): p. 968-975.
335. Toor, A., H. So, and A.P. Pisano, *Dielectric properties of ligand-modified gold nanoparticle/SU-8 photopolymer based nanocomposites.* Applied Surface Science, 2017. **414**: p. 373-379.
336. Sapra, G. and P. Sharma, *Design and analysis of MEMS MWCNT/epoxy strain sensor using COMSOL.* Published by the Indian Academy of Sciences, 2017. **89**(1): p. 1-5.
337. Ru, F., *Influence of processing conditions on the thermal and mechanical properties of su8 negative photoresist coatings.* Journal of Micromechanics and

Microengineering, 2003. **13**(1): p. 80-88.
338. Kan, J., et al., *Proton beam writing: a tool for high-aspect ratio mask production.* Micro- and Nanosystems Information Storage and Processing Systems, 2007. **13**(5): p. 431-434.
339. Hopcroft, M., et al., *Micromechanical testing of SU-8 cantilevers.* Fatigue & Fracture of Engineering Materials & Structures, 2005. **28**(8): p. 735-742.
340. Wang, P.-C., et al., *Fabrication and Characterization of Polymer Hollow Microneedle Array Using UV Lithography Into Micromolds.* Journal of Microelectromechanical Systems, 2013. **22**(5): p. 1041-1053.
341. Sikanen, T., et al., *Temperature modeling and measurement of an electrokinetic separation chip.* Microfluidics and Nanofluidics, 2008. **5**(4): p. 479-491.
342. Thaysen, J., *Polymer-based stress sensor with integrated readout.* Journal of Physics D: Applied Physics, 2002. **35**(21): p. 2698-2703.
343. Adami, A., et al., *Design of a cantilever-based system for genomic applications.* Procedia Engineering, 2011. **25**(C): p. 399-402.
344. Schmid, P., et al., *Gauge Factor of Titanium/Platinum Thin Films up to 350°C.* Procedia Engineering, 2014. **87**(C): p. 172-175.
345. Shokuhfar, A., et al., *Low-cost polymeric microcantilever sensor with titanium as piezoresistive material.* Microelectronic Engineering, 2012. **98**: p. 338-342.
346. Chiriac, H., et al., *Ni–Ag thin films as strain-sensitive materials for piezoresistive sensors.* Sensors & Actuators: A. Physical, 1999. **76**(1-3): p. 376-380.
347. Shokuhfar, A., et al., *Low-cost polymeric microcantilever sensor with titanium as piezoresistive material.* Microelectronic engineering, 2012. **98**: p. 338-342.
348. Kale, N.S. and V.R. Rao, *Design and Fabrication Issues in Affinity Cantilevers for bioMEMS Applications.* Journal of Microelectromechanical Systems, 2006. **15**(6): p. 1789-1794.
349. Youzheng, Z., et al., *A Front-Side Released Single Crystalline Silicon Piezoresistive Microcantilever Sensor.* IEEE Sensors Journal, 2009. **9**(3): p. 246-254.
350. French, P.J., *Polysilicon: a versatile material for microsystems.* Sensors & Actuators: A. Physical, 2002. **99**(1-2): p. 3-12.
351. Kale, N.S., et al., *Fabrication and Characterization of a Polymeric Microcantilever With an Encapsulated Hotwire CVD Polysilicon Piezoresistor.* Journal of Microelectromechanical Systems, 2009. **18**(1): p. 79-87.
352. Doll, J.C., et al., *SU-8 force sensing pillar arrays for biological measurements.* Lab on a Chip, 2009. **9**(10): p. 1449-1454.
353. Patil, S.J., N. Duragkar, and V.R. Rao, *An ultra-sensitive piezoresistive polymer nano-composite microcantilever sensor electronic nose platform for explosive vapor detection.* Sensors & Actuators: B. Chemical, 2014. **192**: p. 444-451.
354. Zorman, C.A., R.C. Roberts, and L. Chen, *Additive processes for semiconductors and dielectric materials*, in *MEMS Materials and Processes Handbook*. 2011, Springer. p. 37-136.
355. Kadhim, R., M.A. Muhi, and A.A. Najim, *Structure and optical properties of pbI2 thin film by thermal evaporation.*
356. Johansson, A., et al., *Temperature effects in Au piezoresistors integrated in SU-8 cantilever chips.* Journal of Micromechanics and Microengineering, 2006. **16**(12): p. 2564.